The role of fissures in the hydrology and stability of the Hollin Hill landslide

Johannes van Woerden

The role of fissures in the hydrology and stability of the Hollin Hill landslide

Master of Science Thesis

Johannes van Woerden

Water Science & Management
Earth Sciences
30 ECTs

18 November, 2014

Cover Photo: Tom Dijkstra (British Geological Survey)

Supervision:

Dr. L.P.H. van Beek (Utrecht University)
Dr. T.A. Bogaard (Delft University of Technology)
Dr. T.A. Dijkstra (British Geological Survey)

TU Delft Delft University of Technology

British Geological Survey
NATURAL ENVIRONMENT RESEARCH COUNCIL

Universiteit Utrecht

Abstract

This research focuses on the influence of preferential flow paths through geo-mechanically induced cracks, also known as fissures, on the hydrology and stability of the Hollin Hill landslide. Understanding of the influence of fissures on hydrological processes and stability of landslides is not entirely clear yet, because hydrogeology in landslides is often very heterogeneous and difficult to measure, which is also related to lack of data. Moreover, fissure influences are determined by natural feedback dynamics, such as the relation between fissure connectivity and soil moisture content, known as a hydrological feedback. In addition there is a relation between the occurrence of fissures and the movement of the slope, known as a mechanical feedback. These complexities also apply for the field study of this research, the slow-moving precipitation-induced clayey Hollin Hill landslide in the United Kingdom, which is monitored by the British Geological Survey (BGS). The aim of this research is to gain a better understanding of the influence of fissures and their natural dynamics on the Hollin Hill landslide by means of fieldwork and a conceptual model.

In cooperation with the BGS five infiltration experiments were carried out on the Hollin Hill landslide, where water was applied with a garden sprinklers over plots of approximately 20 m^2 for time periods ranging from 2 to 6 hours. During the sprinkler experiments groundwater levels and soil moisture contents were monitored and Electrical Resistivity Tomography was conducted to study the influence of fissures on the hydrological behaviour at different zones of the landslide. In combination with one month groundwater level measurements from before the experiments, the infiltration experiments revealed the influence of fissures at Plot 3 and 5 where increased infiltration and drainage rates were visible, especially when groundwater levels were higher and thus closer to the bottom of the fissures. The measurement also outlined the presence of perched water tables and their likely influence of hydrological behaviour. The data gained from the fieldwork and literature of the Hollin Hill landslide was used to set up a conceptual model of Hollin Hill in STARWARS, a coupled a hydrology and stability model. The STARWARS model was used to investigate influence of fissures via the hydrology on the stability of the Hollin Hill landslide and to evaluate the dynamic feedback mechanisms of fissures. The Hollin Hill model was carried out with four scenarios; No fissures, with fissures and no feedbacks, with mechanical feedback (no hydrological feedback), and with both feedbacks. The saturated conductivity and porosity parameters of the most-natural both feedbacks scenario were calibrated by comparing the modelled groundwater levels to one year observed groundwater levels and subsequently the parameters of the other scenarios were also adjusted. The validation of all four scenarios was carried out against two years observed groundwater levels. The modelled spatial groundwater and stability outcomes coincide with the observations in literature and fieldwork. The model revealed that the incorporation of fissures causes higher groundwater levels, which lead to more instability of the landslide. It was also found that incorporation of the hydrological feedback might overestimates the drainage capacities of the landslide and thus also stability of the landslide.

Overall, from this research can be concluded that preferential flow through fissures, influences hydrological behaviour as infiltration and drainage processes in landslides. Moreover, this thesis outlined the spatial heterogeneity of soil hydraulic properties in the Hollin Landslide and the importance of dynamic natural feedbacks mechanisms of fissure influences. Lastly, the fieldwork and model revealed that disturbing layers and perched water tables in the soil also of importance to hydrological behaviour and should not be neglected during fissure researches.

List of symbols

A =	Area size [L^2]
a_{fis} =	Aperture of fissures [L]
C_{fis} =	Fissure connectivity [-]
c =	Cohesion [M L^{-1} T^{-2}]
D_i =	Layer depth [L]
ET_o =	Reference potential evapotranspiration (L T^{-1})
E =	Total evaporation during experiment [L^3]
F_{fis} =	Fraction of the surface area covered by fissures [L^2L^{-2}]
f_s =	Factor of safety [-]
h =	Groundwater height [L]
h_A =	Air entry value [L]
$\|h\|$ =	Absolute matrix suction [L]
I =	Current flowing through the conductor [A]
K_{sat} =	Saturated hydraulic conductivity of the soil [LT^{-1}]
k_r =	Unsaturated hydraulic conductivity [-]
k =	Depletion factor of the storage [T]
K_T =	Empirical coefficient is 0.170 [-]
L =	Length of the conductor [L]
L_{mat} =	Width of the matrix block [L]
N_{fis} =	Numbers of fissures is equal in x and y direction [-]
P =	Precipitation [L^3]
R =	Resistance of the conductor [M L^2 T^{-3} A^{-2}]
R_a =	Extra-terrestrial radiation [MJ m^{-2} T^{-1}]
T =	Daily temperature at 2 m height [°C]
u =	Pore water pressure [$ML^{-1}T^{-2}$]
Q_{sat} =	Saturated flow [L^3T^{-1}]
V =	Potential Difference across the conductor [M m^2]
W =	Total fraction weight [$ML^{-1}T^{-2}$]
α =	Shape factor for matrix and fissures [-]
β =	Slope angle [°]
γ_w =	Specific weight of water [$ML^{-2}T^{-2}$]
ΔS =	Change in storage over the duration of the experiment [L^3]
Δx =	Cell length of the model [L]
Δx^2 =	Surface area [L^2]
θ =	Soil moisture content [-]
θ_E =	Effective degree of saturation [-]
ρ =	Resistivity of the conductor material [M L^2 T^{-3} A^{-2}]
σ =	Total normal stress [$ML^{-1}T^{-2}$]
σ' =	Effective normal stress [$ML^{-1}T^{-2}$]
τ =	Shear strength [$ML^{-1}T^{-2}$]
τ =	Tortuosity parameter in Chapter 5 [-]
φ =	Angle of internal friction [°]

List of subscripts

fc =	field capacity
fis =	fissure
GWin =	groundwater inflow
GWout =	groundwater outflow
i =	initial
mat =	matrix
max =	maximum
min =	minimum
OF =	overland flow
p =	previous
sat =	saturation
SSF =	subsurface flow
t =	time
x =	x-direction
y =	y-direction

List of abbreviations

BGS =	British Geological Survey
DF =	Dogger Formation
ERT =	Electrical Resistivity Tomography
RMF =	Redcar Mudstone Formation
RMSE =	Root Mean Square Error
SSF =	Staithes Sandstone Formation
VMC =	Volumetric moisture content
WMF =	Whitby Mudstone Formation

Contents

1. Introduction

1.1 Background and problem description

A landslide is as 'a downward and outward movement of slope forming material under the influence of gravity' (Varnes, 1978). Landslides can be classified on their different kind of movements and materials that can vary from thick clayey landslides that move with velocities of only tens of centimetres a year to shallow mudslides that move with velocities of several hundred kilometres an hour (Varnes, 1978). The movement of a landslide can be triggered by different mechanisms such as for example deforestation, human constructions, earthquakes and the most common triggering-mechanism; precipitation (Van Asch et al., 2007). The latter one, precipitation-induced, slow-moving landslides are the focus of this research. In this type of landslides, precipitation causes groundwater levels to rise and thus water pore pressure to increase, which subsequently can lead to decreased slope stability and movement of the slope. When the landslide starts to move differential displacements can cause a continuous opening and closing of cracks, better known as fissures. These fissures form preferential flow paths with other hydraulic properties than the soil matrix and affect the infiltration and draining processes of the landslide. The effectiveness of fissures to transmit water is moreover related to the connectivity of the fissures, which is found to be dependent on the wetness of the soil (Van Schaik et al., 2008). This natural dynamic is known as a hydrological feedback mechanism (Krzeminska, 2012). There is also a mechanical feedback mechanism, which is the relation between the continuous displacements of the landslide and the development of fissures (Krzeminska, 2012; Wenker, 2013).

The impact of landslides is enormous since they are one of the most destructive natural hazards, which yearly kill thousands of people and cause tens of billions property damage (Brabb, 1991; Petley, 2008). It is expected that over the next 80 years climate change (due to e.g. heavier precipitation), and in even larger extent human activity and land-use change (e.g. human construction, deforestation), will affect landslide frequency (Collison et al., 2000). Therefore it is important to understand the triggering mechanisms and occurrence of landslides to enhance the prediction, and may reduce or even avoid damage caused by landslides. In order to attain a better understanding of the failure mechanisms of landslides they are mapped, assessed, monitored and modelled all over the world (Reichenbach et al., 2002; Reid et al., 2008; Shen & Fernandez-Steeger, 2011). However, despite these extensive and valuable researches, complete understanding of the earlier mentioned precipitation-induced landslides and the influences of fissures is still lacking (Krzeminska, 2012). One of the problems for understanding precipitation-induced landslides is often the lack of data, especially when hydrogeology is very heterogeneous and difficult to measure (Bogaard et al., 2007). Although monitoring techniques to collect data and understanding of landslide behaviour has improved over the last years, complete understanding of infiltration and percolation processes, subsurface flow paths and residence time of groundwater in landslides is still lacking and difficult to measure or capture during failure (Bogaard et al., 2004; Van Asch et al., 2007; Krzeminska, 2012). Moreover, Weiler & McDonnel (2007) outlined that for conceptualisation and parameterisation of the effect of lateral preferential flow on hillslope hydrology the incorporation of the spatially dynamic nature of preferential flow systems is one of the greatest challenges. The importance of the dynamic hydrological and mechanical feedback mechanisms is also investigated by Krzeminska (20120), who also stressed the need for future research on these topics.

The lack of understanding in the above mentioned landslide mechanisms also applies to the field site of this research, the Hollin Hill landslide near Mowthorpe (United Kingdom) that is surveyed by the British Geological Survey. At the Hollin Hill landslide still little is known about hydrogeological behaviour (Chamber et al., 2008) and regarding to fissure influences. The presence of fissures and their likely influence on slope movements are described in the literature (Gun et al., 2013), but detailed information of the relation between hydrology, dynamic fissure behaviour and slope displacements of the landslide is still lacking.

1.2 Research aim and questions

The aim of this research is to gain a better understanding of the relations between hydrological behaviour, influence of fissures and landslide stability. To attain this, these aspects were investigated at the Hollin Hill landslide in the United Kingdom, by means of fieldwork and a conceptual model in the hydrological and stability model STARWARS (Van Beek, 2002). The fieldwork included infiltration experiments to identify the heterogeneity of hydrological processes and preferential flows through fissures. Also, the fieldwork was intended to provide lithological and hydrological data to develop a conceptual model of the Hollin Hill landslide. The model was used to analyse the influence of fissures and their natural dynamic behaviour on landslide stability with different fissure configurations. Finally, the outcome of this study may also serve to improve forecasting and prediction of landslides on the regional scale in Great-Britain and may even for other locations and different scales.

Summarizing, the main research question and its sub question to be answered are:

What is the influence of fissures via the hydrology on the stability of the Hollin Hill landslide?

- Can the influence of fissures on the hydrology be traced during field scale infiltration experiments for landslide features that experience different displacements?
- How can the information gained from field experiments be incorporated in STARWARS as a static fissure configuration to simulate the relation between hydrology and stability of Hollin Hill?
- Does the observed landslide activity differ from the simulation under static fissure configurations and, if so, can feedback mechanisms between activity and fissure content lead to a better agreement?

1.3 Outline thesis

In Chapter 2 a literature study is presented in which the mechanisms and processes of landslides, and in particular precipitation-induced slow-moving landslides with fissures are described. The literature study gives an overview of studies that outline different available possibilities to conduct field experiments, measurements and trace fissure mechanisms. Moreover, Chapter 2 describes several models that have been used in the literature to model landslides. In Chapter 3 the different aspects as geomorphology, hydrology and most important findings in the literature are given of the Hollin Hill landslide to develop background information for the fieldwork. Chapter 4 describes the methodology of the conducted infiltration experiments and measurements, followed by the results of the fieldwork. The chapter ends with a hydrological conceptualisation of the Hollin Hill landslide, and a discussion and conclusion of the results. The conceptual model of the Hollin Hill landslide is

treated in Chapter 5. The chapter starts with an explanation of the used model STARWARS, followed by the incorporation of the Hollin Hill landslide, based on the data from the literature and fieldwork. Subsequently, the results are shown from the four different fissure configurations, with a discussion and conclusion in the last paragraph of the chapter. The report ends with a final synthesis of the research and further recommendations in Chapter 6.

2. Literature study

2.1 Movement and hydrology of landslides

Varnes (1978) classified landslides on their different types of movement and materials. Briefly described, the materials of a landslide can be rock, debris or earth. The different types of movement of a landslide, or also known as failure mechanism, consists of fall, topple, rotational sliding, translational sliding, lateral spreading and flow. Nevertheless, landslides can be more complex when the landslide encompasses one or more types of movements or materials (Highland & Bobrowsky, 2008). Beside the different mechanisms a landslide also has different zones, which are labelled in Fig. 2.1.

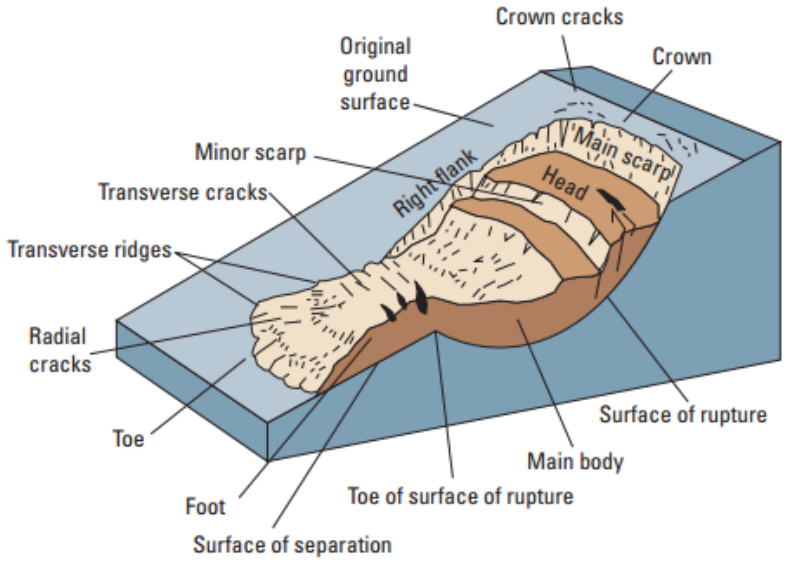

Fig. 2.1: A schematic overview of a rotational landslide that evolved into an earthflow including names of the different zone (Varnes, 1978).

The movement of a landslide is the result of different forces that work on a soil body such as gravity, mobilised friction, buoyancy and seepage. The resistance that a soil body contains to prevent the soil from moving depends on the mobilised shear strength (τ) along the slip surface. This mobilised shear strength is defined by the Mohr-Coulomb equation as (e.g., Krzeminska, 2012):

$$\tau = c + \sigma' \tan(\varphi) \qquad (2.1)$$

Where:

c =	Cohesion of the soil [kPa]
φ =	Angle of internal friction [°]
σ' =	Effective normal stress [kNm^{-2}]
	σ' = σ−u
σ =	Total normal stress [kNm^{-2}]
u =	Pore water pressure [kNm^{-2}]

When the shear stress (i.e. gravitational forces) of a soil overpasses the shear strength, which consist of friction and cohesion forces, than the slope can start to move. The movement precipitation-induced landslide is often caused by both preparatory factors, which work to make the slope increasingly susceptible to failure without actually initiating it, and triggering mechanisms, which

initiate the movement (Nettleton et al., 2005). In general the causes of movement can be distinguished into two groups; internal and external causes (Bogaard, 2001):

- *Internal causes* are a result of changes in water regimes (e.g. increased pore pressure) that cause a reduction of frictional forces or a result of decreased material properties (e.g. weathering, internal erosion);
- *External causes* are factors as changing slope geometry (e.g. slope erosion, undercutting of the slope), vibration (e.g. earthquakes, movement of tectonic plates) and changes in surcharges (e.g. vegetation, buildings), which increase gravitational shear stresses.

Precipitation-induced landslides and preferential flow

Precipitation-induced landslides are mainly the result of hydrological, internal causes. The relation between the hydrology and stability of a slope is caused by infiltration of precipitation, which result cause an increased pore water pressure in the soil matrix that will subsequently lead to a decreased effective stress and declining internal strength of the slope (Van Asch et al., 2007). In other words, the increased pore water pressure causes the stabilizing forces to become smaller than the driving forces, leading to downward and outward movements of slope forming materials (Varnes, 1978).

Beside the infiltration of water through the soil matrix there are preferential flow paths of water solutes, which bypass the porous matrix and affect slope stability (Hendrickx & Flury, 2001). Krzeminska (2012) distinguished three types of preferential flow, which are described below and shown in Fig. 2.2:

- Rapid macropore flow (Beven & Germann, 1982) caused by soil fauna, plants roots, cracks in clayey soils or natural soil pipes (Fig. 2.2a);
- Unstable finger flow (Ritsma & Dekker, 1994), caused by water repellency, soil layering or air entrapment in an instable wetting front (Fig. 2.2b);
- Funnel flow (Roth, 1995) caused by changing flow paths of the main flow due to sloping layers, lenses or stones (Fig 2.2c).

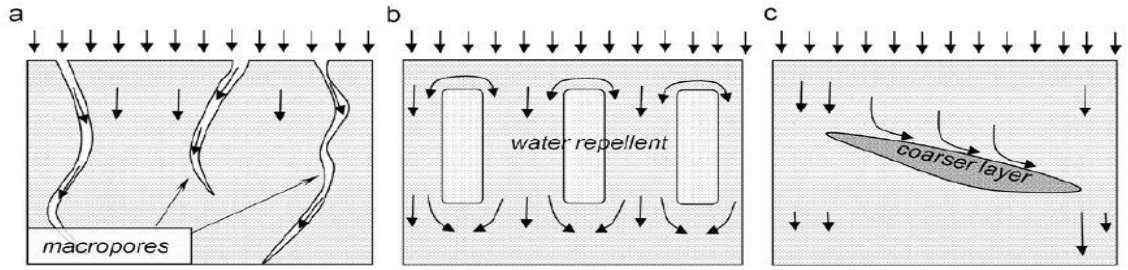

Fig. 2.2: Overview of the three different types of preferential flow, which are described above: (a) Macropore flow, (b) Water repellency, (c) Funnel flow (Krzeminska, 2012).

Preferential flow is of great importance for slope hydrology and is found to be more the rule than the exception (Pierson, 1983; Van Asch et al., 1999; Roulier & Schulin, 2008; Nieber & Sidle, 2010). In this research is focused on preferential macropore flow in precipitation-induced slow-moving landslides through geo-mechanically induced crack, known as fissures. These fissures consist of macropores, which refer to structural pores that are much larger than the average soil matrix pores (Greco, 2002) and drain mainly by gravitational forces (not influenced by capillarity (Krzeminska, 2012). During rainfall, fissures form vertical preferential flow paths for more rapid recharge to the groundwater and cause a faster increase of pore water pressure and thus declined slope stability.

Connected fissures also form a network of lateral drainage, which can limit the build-up of pore water pressure. However, when a lateral drainage is a dead end and the storage capacity is exceeded, it can contribute to a higher pore pressure in the surrounding soil again (McDonnel, 1990; Hencher, 2010).

The ability of fissures to drain water laterally downslope depends on the size, spatial distribution and connectivity of the macropores (Beven & Germann, 1982; McDonnel, 1990; Nobles et al., 2004) The amount of water that macropores potentially conduct or store, depends on the size of the macropores and the connectivity between macropores. It is most likely that the macropores are not continuous throughout the soil profile and that they are separated by matrix blocks located at the endpoint of the individual macropores (Noguchi et al., 1999; Sidle et al., 2001), see Fig. 2.3. Macropore connectivity and transmissivity therefore depends on the water content of the in between laying matrix blocks and macropore effectiveness increases with wetness (Tsuboyama et al., 1994; Sidle et al., 2000; Van Schaik et al., 2008). This relation between soil moisture and fissure connectivity is also known as a hydrological feedback mechanism (Krzeminska, 2012). However, this relation between soil moisture and fissure connectivity is qualitative only (Nieber & Sidle, 2010) and remains difficult to quantify (Krzeminska, 2012).

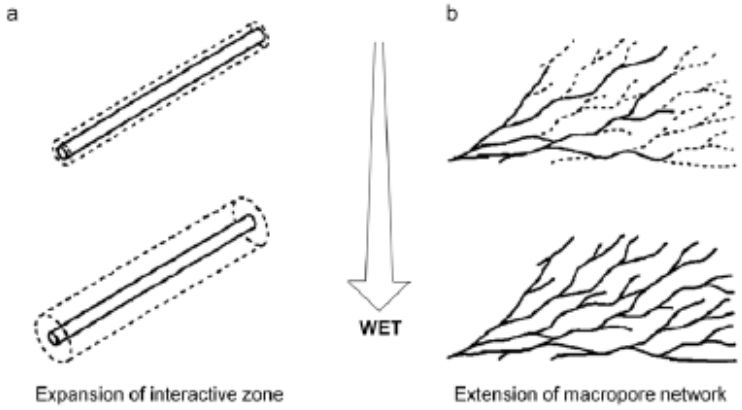

Fig. 2.3: Conceptual model of (a) an expansion of surrounding soil that interacts with water in macropores and (b) the extension of macropore network with increasing moisture content of the soil (Tsuboyama et al., 1994).

The development of fissures in slow-moving landslides takes place when differential displacements result in a continuous opening and closing of fissures (see Fig. 2.4). This movement can also cause open fissures to be refilled with higher porosity materials than the matrix and change the bottom in a dual-permeability network wherein hydraulic properties change dynamically (Krzeminska, 2012).
The dynamic relation between the movement of the slope and the influence on the amount and size of fissure is also described by Krzeminska (2012) as a mechanical feedback mechanism.

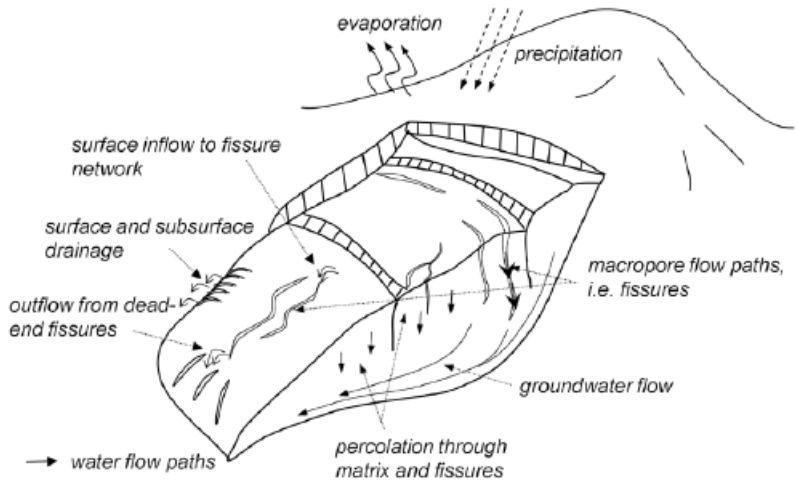

Fig. 2.4: Influences of preferential flow paths due to fissures in a schematic representation of a landslide (Krzeminska, 2012).

2.2 Measurements, monitoring and experiments in landslide research

Knowledge of processes and mechanisms in rainfall-induced landslides is over the last decades enhanced by numerous of worldwide case studies with field measurements, such as in Kyrgyzstan (Havenith et al., 2006), Hong Kong (Chen & Lee, 2003), Austria (Wienhöfer et al., 2010) and France (Bogaard et al. 2007; Krzeminska, 2012; Wenker, 2013). These field measurements lasted from short single day experiments to monitoring programs of multiple years, which all mainly focussed on geophysical movement, the behaviour of hydrology, or a combination of both. The most common devices that are used to study geophysical behaviour of landslides are: Extensometers to detect movement, inclinometers for slope indication, GPS (Global Positioning System) and LiDAR to monitor the movement and change in shape of the surface (Inada & Takagi, 2010). The most common devices to monitor hydrological behaviour of landslides are measurement devices as piezometers to measure groundwater levels, tensiometers for soil moisture content and artificial and dye tracers to determine flow paths and the origin of water (Schulz et al., 2009). Other studies concluded that Electrical Resistivity Tomography (ERT) is a useful tool for site characterization and monitoring (Newmark et al., 1999). Distributed Temperature Sensing is found to be useful to asses and monitor hydrological processes (Lane, et al., 2008).

The literature shows that especially infiltration experiments were found to be very useful to gain a better understanding of hydrological processes and fissure influences on landslides (Oberdoerster et al., 2009; Debieche et al., 2010; Krzeminska, 2012). Debieche et al (2010) conducted artificial rainfall experiments at a 100 m^2 infiltration plot on the Super-Sauze clay-shale mudslide in France and monitored with several hydrological, hydrochemical and geophysical equipment. The artificial rainfall was applied by a sprinkler over a period of 14 days with a mean rainfall intensity of 8 mm per hour. The rainfall was applied with a garden sprinkler and different measurements took place with rain gauges, piezometers, tensiometers and soil moisture devices. Based on the measurement results Debieche et al. (2010) setup a hydrological conceptual model and concluded that the outcome of the hydrodynamic and hydrochemical responses of the tracing experiments gave insight into: '(1) the horizontal and vertical variability of the rain infiltration in unstable black marl hillslopes; (2) the effect of shallow fissures on the groundwater recharge; (3) the role of piston flow on the rate of water level changes and the increase of pore water pressures and (4) the effect of material

heterogeneity in the development of preferential water flows and local perched water tables' (p. 2571). Krzeminska (2012) conducted smaller infiltration experiments on three plots of 1 m^2 with sprinkler intensities of 20 to 30 mm per 15 minutes during 7 to 8 hours of sprinkling in blocks of 15 minutes sprinkling and 15 minutes breaks. During the experiments measurements were carried out with rain gauges, moisture content devices, water pressure devices, chemical tracers and Distributed Temperature Sensing. A water and mass balance, together with a depletion curve method applied on the measured groundwater level drawdowns was used to research the hydrological behaviour. The study outlined the spatial heterogeneity of soil hydraulic properties and dominant hydrological processes in slow-moving clay-shale landslide. Moreover, preferential flow paths were identified and it was confirmed that they increase the vertical infiltration rate and control the direction of subsurface water flow.

ERT can measure by means of fluxes of electrical charges the electrical resistivity of a soil, which is related to the saturation of the soil and can therefore give insight in hydrological behaviour (Vecchia & Cosentini, 2011). Oberdoerster et al. (2009) conducted infiltration experiments on a 48 m^2 area in a forest with tracers and ERT measurement to determine the level of saturation of the soil. The ERT measurements revealed possibilities to image the distribution of preferential flow paths and the velocity of the paths, but unfortunately tracer movement of the individual preferential flow paths were not visible. In 1992 Daily & Ramirez already highlighted the possibilities of ERT by imaging the resistivity distribution before and during two infiltration experiments. After applying water into the vadose zone the differences between capillary and gravity-driven flow through the sediments were visible on the ERT images. They also concluded that the ERT can be useful to monitor the circuitous moisture movements in heterogeneous soils that would go undetected by borehole measurements.

2.3 Landslide modelling

Conceptual models are useful in landslide research to gain insight and understanding of hydrological and kinematical behaviour of the landslide. Modelling landslides can be done by adopting empirical, statistical, and process based approaches, or a combination of both (Raia et al., 2013). Moreover, models can vary from simple 1-D empirical models to complex physically based 3-D models with either lumped or distributed approaches (Van Asch et al., 2007). However, distributed process based (deterministic, numerical, physically based) models are most suited for shallow precipitation-induced landslides and most preferred to forecast the spatial and temporal occurrence of a landslide (Malet et al., 2005; Raia et al., 2013).

The inclusion of preferential flow into a hydrological model of a hillslope is difficult due to the complexity of the phenomena (Krzeminska, 2012). While modelling preferential macropore flow, the nature of the flow in both matrix and macropores, and the interaction between the two areas are the main component to be defined (Beven & Germann, 1982; Šimůnek et al., 2003; Van Genuchten, 2011). The flow and interaction between the two domains can be classified in different model concepts as: equivalent continuum approach, dual – porosity or multi – porosity approach, dual–permeability approach (Altman, et al., 1996; Van Genuchten et al., 1999). These approaches are mainly stochastic or deterministic, but in the field scale the majority of the macropore flow models use deterministic methods to study water and solute transport. The deterministic models are based on the Richards equation and the assumption of uniform flow within the particular flow domains.

Nevertheless, the majority above mentioned approaches of modelling macropore flow resulted in improved model performance (Krzeminska, 2012).

Several physically based models are used to model precipitation-induced landslides as for example the tRIBS-VEGGIE (Lepore et al., 2013), SHETRAN (Burton & Bathurst, 1998) and STARWARS (Van Beek & Van Asch, 2004; Van Beek, 2002) models. The gross of the physically based landslide models couples a hydrological model and slope stability model and use the safety factor (see also Chapter 5.1) to determine whether a slope is stable or not. The STARWARS (STorage And Redistribution of Water on Agricultural and Revegetated Slopes) model is a physically based model that also includes preferential flow in the model as a dual-permeability system. The STARWARS model is developed in the PCRaster environmental software package and is developed in 1999 by Van Beek. Later the model was adapted by including fissures as preferential flow paths and their hydrological connectivity in both, longitudinal direction as in transverse direction (Van Beek, 2002). A final adaption was conducted by Krzeminska (2012), who included a mechanical fissure feedback, which determines the volume of fissures based on the stability of the slope.

The STARWARS model was used by Kuriakose et al. (2009) to study landslide behaviour of a data poor region in Western Ghats Kerala, India and concluded that the model captured the general temporal and spatial pattern of instability in the area, despite the poor data input. They also concluded that the root cohesion, soil depth and angle of internal friction were the most dominant parameters that influence the slope stability. Moreover, the study stressed the importance of high resolution digital terrain models for accurate mechanistic predictions of a shallow landslide initiation. The STARWARS model is also used multiple times to investigate landslide movement, hydrology and the influence of fissures in the Super-Sauze landslide (Malet et al., 2005; Krzeminska, 2012; Wenker, 2013). Both, Malet et al. (2005) and Krzeminska (2012) concluded that the model reproduced the observed time-depend hydrological well and that outputs were mainly sensitive to the effective porosity and conductivity values. They stated that the STARWARS model is one of the only tools available to the expert to aid in forecasting future behaviour of landslides.

3. The Hollin Hill Landslide

3.1 Introduction

The Hollin Hill landslide was discovered in 2004 by the landowner and in October 2005 a visit was made by the British Geological Survey (BGS) from Keyworth. As a result the BGS installed different monitoring systems and started up researches at the landslide (BGS, 2014). For this Master Thesis research the BGS provided the opportunity and help to research the Hollin Hill landslide by field experiments and the setup of a conceptual model. Prior to the fieldwork and model a literature study in combination with field observations of the Hollin Hill landslide is conducted to develop an overview with geographical, geological and hydrological aspects of the Hollin Hill landslide. These aspects together with the currently existing monitoring and research by the BGS provides a strong background to conduct efficient and fruitful field experiments and modelling work of the Hollin Hill landslide.

3.2 Location and climate

The Hollin Hill landslide is located in the northeast of England near Malton, North Yorkshire at Mowthrope (see Fig. 3.1). The landslide occupies an elevation of between 55 and 100 m above sea level and is approximately 200 m long and 250 to 300 m wide. The slope of the Hollin Hill is facing south and has an average slope angle of approximately 12 degrees (Gunn et al., 2013). Hollin Hill is on the west side bordered by a wood. At the north side and east side Hollin Hill is bordered by other livestock lands and at the south side by a street and more southern cultivation land. In the wood and at the east side of Hollin Hill are also slope movements visible, but to a lesser extent than at Hollin Hill (see also Fig. 3.1).

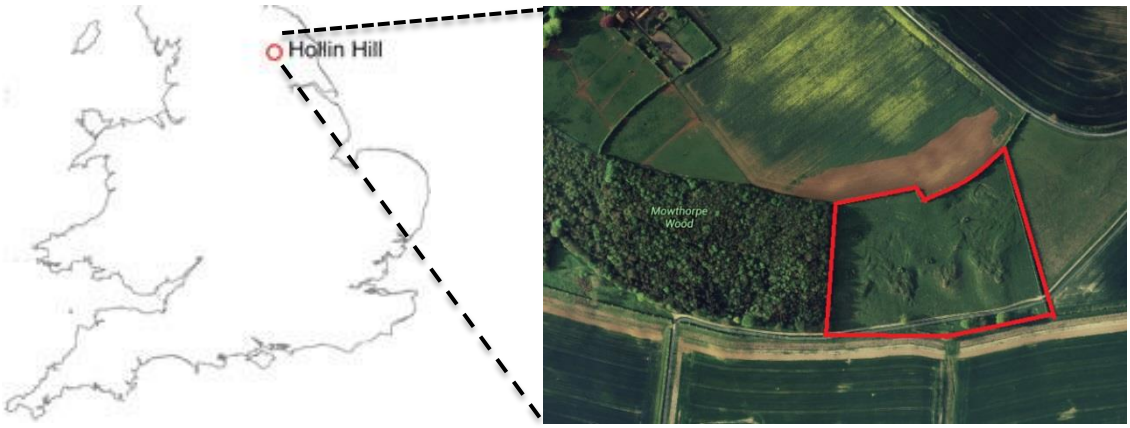

Fig. 3.1: Location of the Hollin Hill landslide (BGS, 2014) and aerial photograph (Google Maps, 2014).

The north of England has a temperature climate with mild summers and mild winters. The nearby weather station at Mowthorpe measured average minimum and maximum temperature of 5.1 and 11.6 degrees per year from 1989 until 2010. The total amount of precipitation at the same weather station was approximately 730 mm per year and number of wet days 128.5. (Met Office, 2014). At the recently installed, Hollin Hill weather station the highest precipitation intensity was measured at 16 mm per hour between November 2011 and January 2013.

3.3 Geology

The Hollin Hill slope is extensively described by the BGS (2014). The Hollin Hill landslide is formed by four different formations (see Fig. 3.2 and also Fig. 3.4 for a cross-section), from base to top: the Lower Lias, Middle Lias, Upper Lias and Dogger Formation. The Lower Lias consists of a Redcar Mudstone Formation (RMF) and forms the toe of the hill. This mudstone formation comprises a layer of up to 200 meter with grey silty, calcareous and sideritic mudstone and thin shelly limestones. Above the Lower Lias the Middle Lias is formed by the Staithes Sandstone Formation (SSF). This sandstone formation encompasses an up to 20 meters thick layer with an upward transition from sandstone or siltstone to shaley mudstone. In the middle part of the escarpment the sandstone formation is associated with well-drained loam soil. Also thin and discontinuous mudstone and sideritic nodules from the Cleveland Ironstone Formation are present in the upper boundary of the sandstone formation. Above the the Middle Lias the largest part of the hill is composed by the Upper Lias of Whitby Mudstone Formation (WMF), a 25-30 m thick formation characterized by grey to dark grey mudstone and siltstone with scattered bands of calcareous and sideritic concretions. Near the ground surface the mudstone formation is weathered and gives rise to a red-brown, poorly drained clay soil. Above the mudstone formation, on the top of the slope, the up to 2.7 meters thick Dogger Formation (DF) is located. This is a thinly developed aquifer consists of calcareous sandstone and ferruginous limestone including rounded clasts of micritic limestone. This head of deposits on the escarpments gives a free-draining sandy soil, which is rich in gravel to cobble-sized rock fragments (Chamber et al., 2008; Gunn et al., 2013; BGS, 2014).

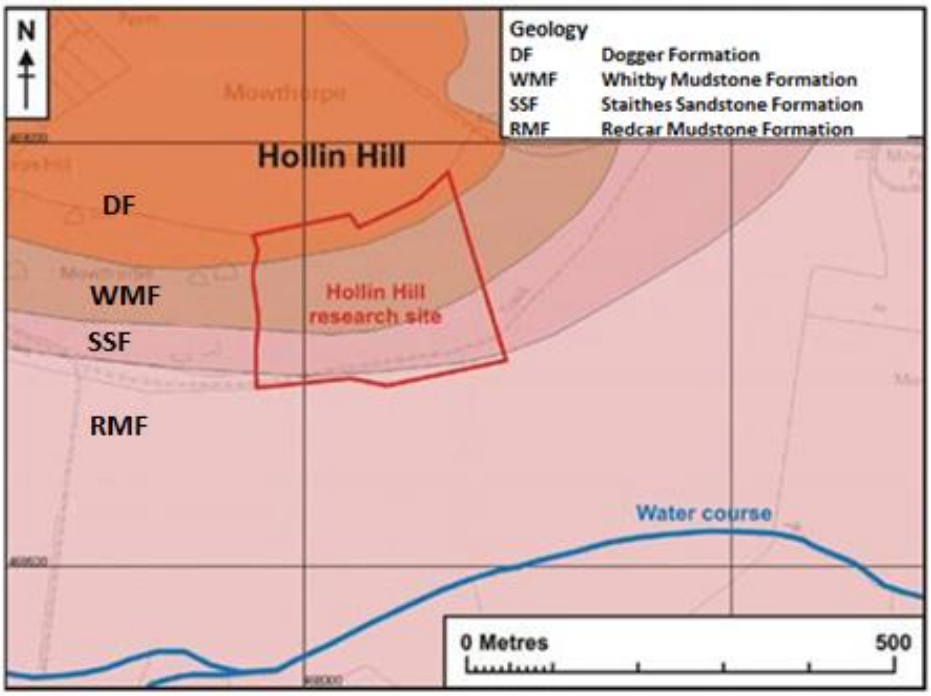

Fig. 3.2: Geology of the Hollin Hill landslide (BGS, 2014).

3.4 Hydrology

Chambers et al. (2008) concluded that knowledge of the hydrology of the Hollin landslide was still incomplete and not well constrained. However, newer research revealed some more insights on the hydrology. Between the sandstone SSF and the less permeable mudstone RMF at the toe of the slope a spring line is observed that is active for most of the year (see Fig. 3.3). At the top of the slope, within a backward tilted section, sag ponds develop during wet periods and it is assumed that water infiltrates here and seeps through the lobes to the base of the slope (see Fig. 3.3). Auger holes revealed that the slipped material within the lobes contain multiple perched water levels and horizons on which seepage occurs within the mudstone WMF and sandstone SSF bedrock (Chambers et al., 2011). The advancement of the lobes, where younger materials overflow older materials is according to Gunn et al. (2013) caused by cyclic changes in moisture content, pore pressure and associated material property changes. Moreover is explained that during dry periods cracks of 300 to 400 mm depth develop due to shrinkage and soil cracking in the advancing toe zone and upper zones of the lobe masses. Most likely these fissures allow water to infiltrate and migrate downslope through the lobe mass during wet periods and leave at the toe of the lobe as a mudflow of water and mud.

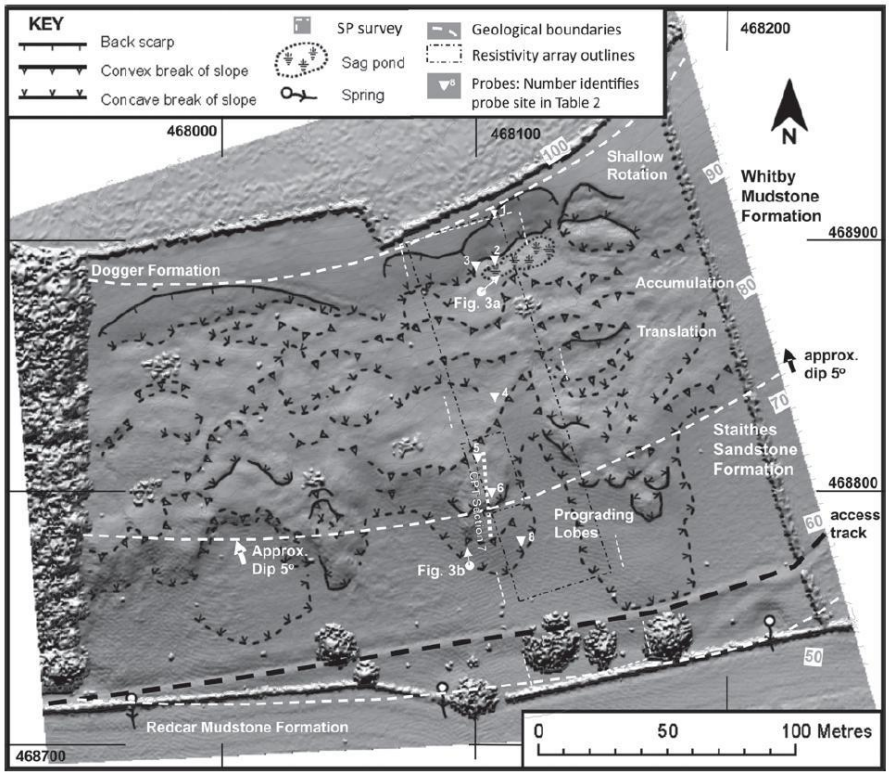

Fig. 3.3: Geomorphological map of Hollin Hill generated from aerial LiDAR data with vegetation included (Gunn, et al., 2013).

3.6 Movement of the slope and fissure formation

The Hollin Hill landslide is a grassed slope and is according to the classification scheme of Cruden and Varnes (1996) a very slow to slow moving composite multiple earth slides with moving rates of only a couple of centimetres a year. The instability of Hollin Hill starts at the top of the slope in the mudstone WMF where shallow rotational failures occur, see Fig. 3.4. This is obvious since the mudstone WMF has one of the highest landslide densities in the United-Kingdom, with 42 landslides per 100 km^2 (Gunn, et al., 2013). The rotational failures cause a series of multiple retrogressive failures, which move as translational landslides and cascades over the lower laying sandstone SSF. This results in the formation of 4 large lobes of slumped material, which move with circa tens of centimetres per year to the base of the slope (BGS, 2014).

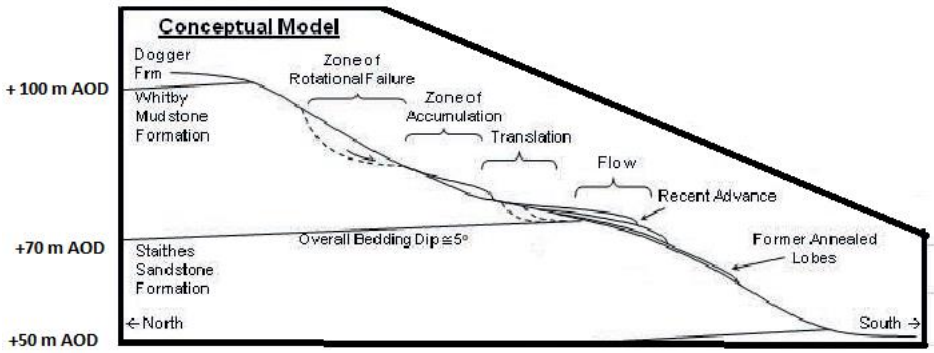

Fig. 3.4: Conceptual movement of Hollin Hill, its movements and the 5 degrees dipping slope of SSF underneath the WMF (Gunn et al., 2013).

The occurrence of different fissure formations in the Hollin Hill landslide is relatively normal to a typical mudslide, see Fig. 3.5. At the top of the rotational zone of the landslide, at the backscarp, mainly tensions cracks are visible in horizontal patterns and in the zone of accumulation compression fissures are presents. In the translation zone tension, shear and compression fissure are present and develop over the entire zone and mixed through each other. At the sides of the different landslide zones also tension or shear crack, or a combination of both develops.

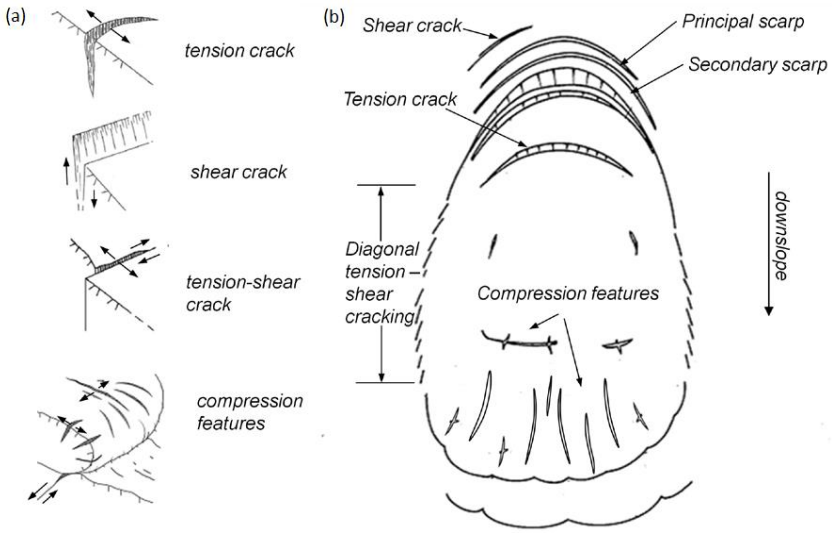

Fig. 3.5: Typical surface fissures formations and their spatial occurrence in a typical mudslide (Krzeminska, 2012 modified after Keaton & Graff, 1996)

3.7 Current monitoring and research

Since October 2005 the BGS monitors the movement of the landslide by combining geomorphological mapping, terrestrial LiDaR and real-time monitoring with geophysics. Scientific research has been set on the site to gain field surveying, geomorphological, geophysical, engineering and hydrological expertise at the BSG. The goal of the monitoring and research is to develop eventually possibilities to predict movement of the landslides (BGS, 2014).

The BGS conducts geoelectrical surveying by means of four 2D Electrical Resistivity Tomography (ERT) lines and Self-Potential profiling lines (SP profile). Besides, a SP mapping area and 3D ERT measurement area is located on the western lobe of the landslide (see Fig. 3.6). The measurements of both ERT and SP profiling are effective in researching landslide behaviour aspects as internal structure, distinguishing different lithology's and indications of water flows and moisture contents (Chambers, et al., 2011). Different augers hole observations have been conducted at 11 locations on the landslide. To measure groundwater levels two piezometers are installed on the eastern and western lobe and measure daily groundwater levels since September 2009.

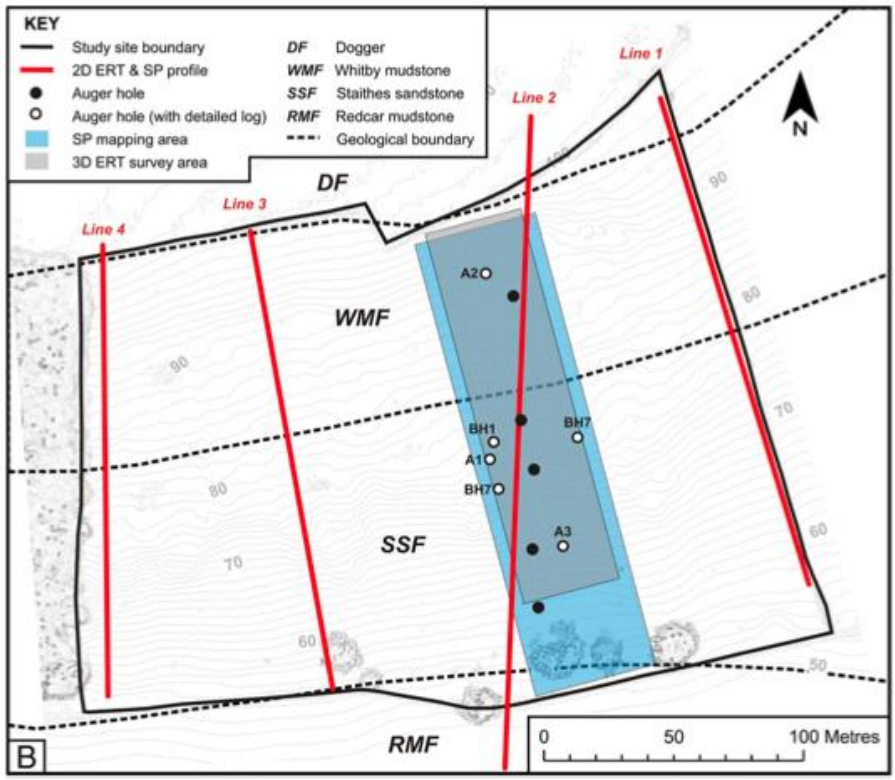

Fig. 3.5: The geophysical survey locations, intrusive sampling points and geological boundaries at Hollin Hill (Chambers, et al., 2011).

4. Infiltration experiments Hollin Hill

4.1 Introduction

In order to gain better understanding of the hydrological processes in the Hollin Hill landslide, five infiltration experiments were carried out on the landslide in collaboration with the BGS in May 2014. During the infiltration experiments, water was applied on plots of approximately 20 m^2 and behaviour of moisture contents and groundwater levels were monitored. The aim of the infiltration experiments was to develop a better insight in the spatial hydrological processes and the influence of preferential flow paths at the different morphological areas of the landslide, by analysing and interpreting the monitoring data. To investigate the reliability of the infiltration experiments and observations, a water balance was set up for each plot. This water balance provides insight in the storage mechanisms and capacities of the plots. Moreover, a groundwater level response analysis was conducted from one month groundwater level measurements to characterize the different plots and indicate preferential flow mechanisms. The outcomes of this chapter will contribute to improve understanding of the Hollin Hill landslide and the set up of the STARWARS model, which is discussed in Chapter 5.

4.2 Methodology

4.2.1 Locations of plots

The five rainfall experiments were located on the two most eastern lobes of the landslide, from here on called the western and eastern lobe (see also Fig. 4.1). In Appendix II photos are shown for each plot. Plot numbers range from 2 to 6 since initially 6 plots had been planned, but Plot 1 was skipped because at this plot was not enough water pressure from gravity flow to carry out the sprinkling experiment. Numbers of the remaining plots have not been changed to avoid confusion with numbering of the measurement equipment. Over the eastern lobe plot 2, 3 and 4 are located from the north to the south of the landslide and on the western lobe plot 5 and 6 are located in the middle of the landslide. The locations of the plots are chosen to attain a hydrogeological insight of all different phases of the landslide as for example the back scarps, rotational zone and translational zone (see Chapter 3.4). Moreover, the different plots and phases have distinct fissure density, what is of interest to this research.

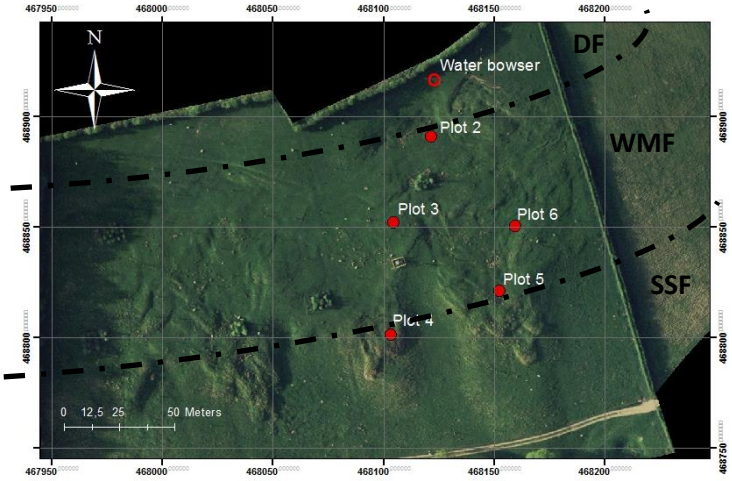

Fig. 4.1: Locations of the 20m^2 plots for the infiltration experiments across the different zones of the Hollin Hill landslide in OSGB36 coordinate system.

4.2.2 Experimental design

The infiltration experiments were carried out with water from a water bowser that was placed on top of the hill. The water bowser with a capacity of 1100 litres was connected with a water hose to a Gardena water sprinkler that was placed in the middle of each plot. The sprinkling area of the Gardena sprinkler is adjustable in width and length (see Fig. 4.2). The elevation difference between the water bowser and plot caused a water pressure from 0.7 Bar (Plot 2) to 2.0 Bar (Plot 4). By means of a flow meter, the pressure of the water flowing from the browser could be adjusted and constantly measured (see Fig. 4.2) to ensure constant rainfall intensities.

Fig. 4.2: (L) Photo of the connection between the flow meter, pressure adjuster and pressure meter, from left to right; (R) Photo the Gardena garden sprinkler.

During the five days of fieldwork one experiment per day was carried out with durations ranging from approximately 2 until 7 hours. The durations of the experiments were dependent on the plot size and sprinkling intensities. The plot size and sprinkling intensities were dependent on the accuracy of the Gardena sprinkler and the weather conditions. The experiments were performed in blocks of sprinkling with intermissions of 15 minutes to measure the soil moisture content and sprinkling intensities. Table 4.1 gives an overview of the dates and times at which the rainfall experiments on each plot took place. The area of the plot size is estimated from visual observations and the total sprinkled amount of water is measured with the flow meter. The total water sprinkled per area unit is a derivation of these two. To distinguish the applied water from natural groundwater and precipitation during for example exfiltration, salt was added to the applied water. The initial salt concentration in the water bowser was measured with an electrical conductivity meter (EC-meter, see paragraph 4.2.3) before the beginning of the experiment.

Table 4.1: Overview of basic information of the sprinkling tests at the different plots, a lower electrical conductivity means a lower salt concentration and vice versa.

Plot	Date	Time	Plot size (m^2)	Total water sprinkled (m^3)	Total water sprinkled per area (mm)	Electrical conductivity in tank (dS/m)
2	7-5-2014	12:25 - 18:50	20 (4x5)	0.973	48	2.6
3	8-5-2014	13:05 - 18:45	20 (4x5)	0.924	46	2.6
4	9-5-2014	10:15 - 13:45	9 (3x3)	0.910	100	2.6
5	12-5-2014	13:50 - 18:20	20 (4x5)	1.034	52	1.4
6	13-5-2014	13:15 - 15:30	20 (4x5)	0.508	25	2.4

4.2.3 Observations and measurements

Prior to every experiment the fissures at every plot were measured and mapped on a grid paper. Subsequently, the locations of the to-be-installed measurement devices were determined based on the geomorphological character of the plot and the positions of the fissures. Before, during and after the experiments the responses of groundwater levels and soil moisture content were locally monitored at the plots. Besides, Electrical Resistivity Tomography was used to attain a 3-dimensional spatial overview of the hydrological processes. The specifications of the used devices are described below.

Groundwater levels

At each plot one piezometer was installed with a Solinst Levelogger Gold (Model 3001) to record water pressure, barometric pressure and temperature every 15 minutes (at plot 5 every 30 minutes).The accuracy of the water level logger is approximately 0.05 kPa for water pressure and 0.055 °C for temperature (Solinst, 2013). The measured water pressure was compensated with the measured barometric pressure (1 kPa = 0.1022 m) to derive an absolute water pressure, measured at the bottom of the piezometer. Lastly, the measured groundwater level was subtracted from the installation depth of the piezometer to calculate the water level below surface. The piezometers were installed one month before the infiltration experiments by the BGS to measure groundwater behaviour under natural circumstances at the different plots.

Moisture content

The volumetric water content, temperature and electrical conductivity were measured with a Decagon GS3 device and stored on a Decagon EM50 data logger. The GS3 device was installed at every plot on four different depths ranging from 5 to 50 cm and measured with an interval of every 5 minutes. The accuracy of the Decagon GS3 is approximately 0.03 m^3/m^3 for de volumetric water content, 10% for the electrical conductivity between 0 to 10 dS/m and 1 °C for the temperature (Decagon Devices, 2011). At every plot also 2 to 4 Delta-T Devices PR1 probes were installed to measure the volumetric water content with an accuracy of approximately 0.06 m^3/m^3 (Van Bavel & Nichols, 2002). The length of the access tubes for the probes is 1 meter and enables measurement at 6 depths: 0.1, 0.2, 0.3, 0.4, 0.6, 1.0 meter. However, due to the stiff clays in the plots the probes could not be installed properly and this caused water to infiltrate along the probes. This resulted in unrealistic read-outs of the PR1 measurements therefore they were not used for this research. The amount of sprinkled water was measured with 4 rain gauges (measured in mm/m^2), a flow meter (m^3 with 4 decimals) and pressure meter (bar).

Electrical Resistivity Tomography

Electrical Resistivity Tomograpy (ERT) is a geophysical method to determine the soil resistivity distribution, which is based on a bulk physical property of materials that describe how difficult an electrical current can pass through the material. One of the factors where the electrical resistivity is determined by is the level of saturation of the material. The traditional electrical resistivity method is to install two pairs of electrodes into the ground, where one pair electrodes is used to send the direct-current electricity into the subsurface and the second pair is used to measure the potential difference in the earth. The resistance of the ground circuit can then be calculated according to the Ohm's law:

$$V = I \cdot R \tag{4.1}$$

Where:

V = Potential Difference across the conductor [V]

I = Current flowing through the conductor [A]

R = Resistance of the conductor [Ωm]

Subsequently, the resistivity of the soil can be calculated by the electrode geometry and the resistance, see equation 4.2. Finally it is also important to note that the resistivity is the reciprocal of the electrical conductivity (Dijkstra et al., 2011).

$$\rho = \frac{R \cdot A}{L} \tag{4.2}$$

Where:

ρ = Resistivity of the conductor material [Ωm]

A = Cross sectional area [m^2]

L = Length of the conductor [m]

The ERT that is also used for this fieldwork is an enhancement of the traditional electrical resistivity method and consist of an array with electrodes placed on equal spacing. This makes it possible to measure resistivity between different electrodes over different lengths and directions. The spacing of the electrodes is based on the desired depth of the penetration, the required resolution and the type of area. Larger electrode spacing provides deeper measurements, but a lower resolution and vice versa. For this fieldwork the 3D ERT was installed at every plot on a 5 by 5 m array with 100 electrodes, placed on 50 centimetres intervals in x and y direction. The electrodes were installed 10 cm deep into the ground.

To attain clear images of hydrological behaviour 6 or 7 acquisitions were conducted at every plot. The first acquisition was conducted prior to the sprinkler experiments and the last one the morning after the experiment. Each acquisition comprised hundreds of individual measurements with acquisition durations of approximately 1 hour and 10 minutes. The measurements consist of three components:

1) Inline dipole-dipole measurements along horizontal, vertical and diagonal directions with all possible combinations of dipole-length (α) to a maximum of α=1.5 m and dipole-separation (n) to a maximum of n=7;
2) Equatorial dipole-dipole measurements in the horizontal and vertical directions with α = 0.5 m maximum and all possible separations with n = 9 maximum;
3) Optimised configurations selected to enhance the model resolution (the basic algorithm for 2D lines is described in “Practical aspects of applied optimized survey design for electrical resistivity tomography” (Wilkinson, et al., 2012)

For more detailed information on the used ERT methodology one is referred to Dijkstra et al. (2011) and Wilkinson et al. (2012).

4.2.4 Analysis and interpretation

In order to structure, analyse and interpret the monitored data different data processing methods were used, which are described below.

Sprinkling rates and distribution

The amount of sprinkled rainfall per sprinkling block was measured with a flow meter and four rain gauges that were spatially distributed over the plot. From both measurements graphs are made that shows the sprinkling intensity per sprinkling block measured with the flow meter (total amount sprinkled water [m^3] divided by the surface area [m^2]), the average rainfall measured from the four rain gauges, and the maximum and minimum measured rainfall in the rain gauges. This resulted in a graph that shows the spatial and temporal heterogeneity of the sprinkling experiments.

Groundwater level and moisture content

The constant groundwater level measurements from the Sollinst Levelogger and the moisture content measurements from the GS3 are plotted together in a graph over time. This enables the comparison between responses of moisture contents over different depths and the groundwater level. Time scale is from a couple of hours before the experiment until the next morning after the experiments to show initial values and drawdowns. Besides, the GS3 moisture content measurements were used to develop a wetting front curve. This wetting curve shows the moisture content at the four measurements depths of the GS3 device per time step, with on the first time step the initial moisture content. This is of interest to identify different soil layers and their storage capacities over time in combination with the borehole profiles of Appendix II.

Electrical Resistivity Tomography

At every plot an initial ERT acquisition was performed before the start of the sprinkling experiment and subsequently every new acquisition started after approximately 1 hour and 20 minutes. The results of these acquisitions are presented in two different ways. The first one is the presentation of every acquisition in absolute values of resistivity (Ω-m) on natural logarithmic scale. The absolute values can be interpreted as the higher resistivity, the lower the moisture content and the lower the resistivity, the higher the moisture content. The second presentations of the ERT acquisitions are the relative ratios: The absolute values of the new acquisition divided by the absolute values of the first initial acquisition from before the start of the experiment (t_1-t_0, t_2-t_0, t_3-t_0 etc.). This means that when the ratio is 1 there is no change and when the ratio is negative the electrical resistivity became lower thus moisture content increased. Logically, a positive ratio indicates a decrease in moisture content.

Hydrological analysis

In order to determine the different water flows, reliability and outcomes of the sprinkling experiments a water balance is set up for each plot. The water balance is calculated for the complete duration of each sprinkling experiment, based on the following formula:

$$\mathrm{P} + Q_{GW\,in} = \mathrm{E} + Q_{GW\,out} + Q_{OF} + Q_{SSF} + \Delta\mathrm{S} \qquad (4.3)$$

Where:

P = Amount of sprinkled water [m^3]

$Q_{GW\,in}$ = Groundwater inflow [m^3]

$Q_{GW\ out}$ = Groundwater outflow [m^3]
E = Total evaporation during experiment [m^3]
Q_{OF} = Overland flow [m^3]
Q_{SSF} = Subsurface flow/exfiltration [m^3]
ΔS = Change in storage over the duration of the experiment [m^3]

Since only one piezometer was installed per plot it is very difficult to estimate the groundwater inflow and groundwater outflow, therefore it is assumed that inflow was equal to outflow and the two terms can be neglected. During the experiments the weather was predominantly grey and not warm, thus evaporation is also neglected. Overland flow was not observed during any experiment and exfiltration was only observed during the experiment at Plot 5, but could not be quantified. Therefore, the simplified water balance becomes:

$$\mathrm{P} = \Delta \mathrm{S} = \Delta S_{UZ} + \Delta S_{GW} \tag{4.4}$$

The change in storage from the start until the end of the experiment comprises of two parts, the change in storage due to changes in volumetric moisture content in the unsaturated zone (ΔS_{UZ}) and the change in storage due to the changes in groundwater level (ΔS_{GW}). The change in volumetric moisture content is calculated from the moisture content measurements that were performed in every plot at four depths with the GS3 device (θ_s- θ_i). At every measurement depth it is assumed that the layer above, until the surface level or next measurement depth, contains a homogeneous moisture content (these layers also often coincided with the borehole profile of Appendix II). For the deepest measurement depth (VMC_4) it is assumed that both, the layer above (until VMC_3) and the layer below (until water level) contain a homogeneous moisture content. The change in moisture content at every measurement depth is multiplied by the thickness of the layer. Subsequently, the sum of changes in all layers results in the total change in storage of the unsaturated zone:

$$\Delta S_{UZ} = \sum_{i=VMC_1}^{VMC_4} D_i * (\theta_s - \theta_i) * A \tag{4.5}$$

Where:
VMC_{1-4}= Measurement depths of GS3 from shallow (VMC_1) to deep (VMC_4) [m]
D_i= Layer depth above measurement depth [m]
θ_s= Measured saturated moisture content at the end of the experiment [-]
θ_i = Measured initial moisture content before the start of the experiment [-]
A = Area size of sprinkled plot, visually observed [m^2]

Beside the increase in moisture content in the unsaturated zone, there is an increase in water level. This increase in water level causes a change in storage which can be calculated with the following formula:

$$\Delta S_{GW} = \Delta h_g * (n - \theta_i) * A \tag{4.6}$$

Where:
Δh_g = Change in groundwater level from begin until end of the experiment [m]
θ_s = Measured saturated moisture content at VMC_4 [-]
θ_i = Measured average initial moisture content at VMC_4 [-]
A = Area size of sprinkled plot, visually observed [m^2]

In first case, the initial moisture contents of the deepest moisture content measurements were used to calculate the change in storage due to the increased water level. This resulted in very large change in storages: the change in storage was approximately 150% to 200% of the applied rainfall. These very high ratios were most likely caused by the air-entry value of approximately 40 cm, which is retrieved from the Rosetta program (Schaap et al., 2001) by giving in soil properties. Therefore, the moisture content values were used from after the jump due to exceedance of the water-entry value. This eventually yielded in more realistic values.

Groundwater level response

In advance of the infiltration experiments the Sollinst Leveloggers were installed in the piezometers at the five plots and monitored the groundwater levels for approximately one month. The sprinkling experiments give only insight in the responses of groundwater levels during short and high intensified rainfall experiments. Contrary, the one month groundwater level measurements can be used to characterize the different plots based on groundwater responses during natural circumstances and longer time series, which is found to be useful by Debieche et al. (2010) and Krzeminska (2012). The one month time series reveal different drawdowns of groundwater level, which are used to calculate decay factors from, according to the recession analysis. The decay factors are obtained by applying the hydrograph separation method and the linear reservoir concept in addition of a depletion curve (Peters, 1994; Tallaksen, 1995). The decay factor (k) is the depletion factor that indicates the depletion time of a storage. Assuming that the change in storage is a direct function of the change in groundwater level, the depletion factor can be calculated for the different segments of the drawdown curves by defining inflexion points on logarithmic plot of the water levels of time. This empirical method is explained by Linsley et al. (1975)

$$h_{t+\Delta t} = h_t * e^{\frac{-\Delta t}{k}} \quad (4.7)$$

Where:

h_t = Groundwater level at time t [m]

Δt= Temporal resolution of groundwater level observation [days]

k= Depletion factor of the storage [days]

4.3 Measurement results per plot

4.3.1 Plot 2

Plot 2 is located just near the sag pond below the first rotational landslide on the WMF. The site is on a planar slope that is slightly tilted backward and fully covered with grass. No fissures were visible on this plot. On the plot 4 rain gauges, 3 Delta-T PR1 access tubes, 1 piezometer and 1 GS3 device were installed (see Fig. 4.3). The GS3 device was installed at 0.05, 0.10, 0.20, 0.40 meter depth.

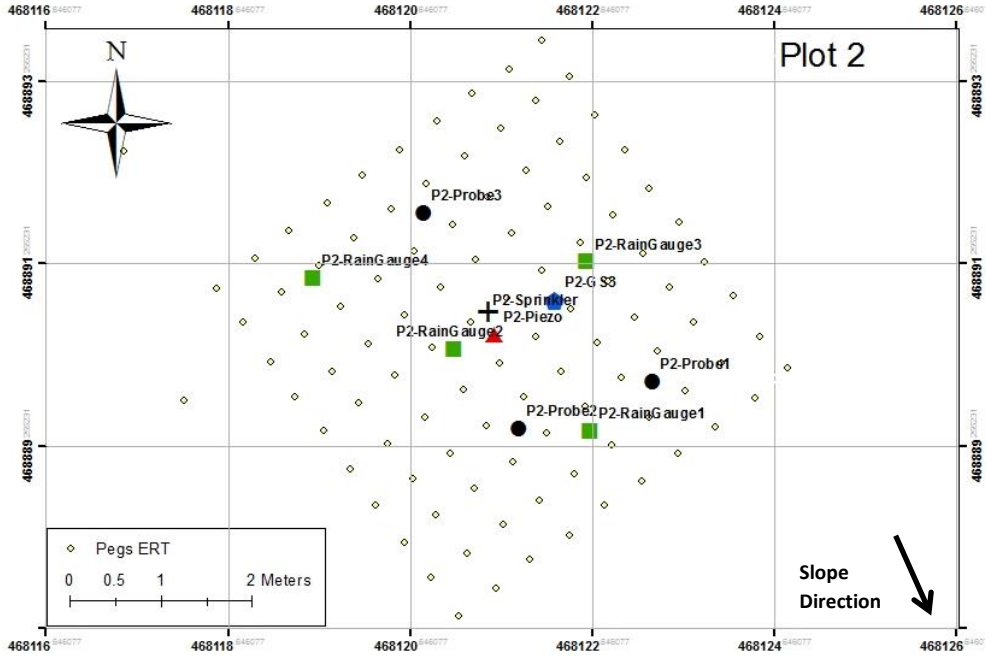

Fig. 4.3: Overview of the location and measurement devices of Plot 2.

During the days preceding of the experiment at Plot 2 it was dry and sunny. During the experiment itself it was cloudy and sunny, with two very light rainfalls of approximately 0.2 mm in total. No overland flow occurred during sprinkling and the sprinkling rate was kept relatively constant with an average of approximately 5 to 7 mm per half an hour (see Fig. 4.4).

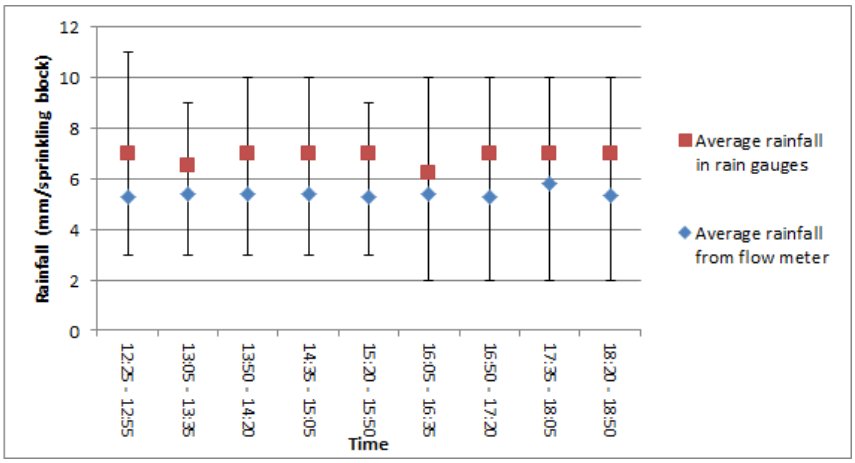

Fig. 4.4: Rainfall intensities from sprinkler at Plot 2, measured by rain gauges and flow meter in mm per block of sprinkling (30 minutes) with breaks of 15 minutes. The error bars show the minimum and maximum rainfall measured in the 4 rain gauges per sprinkling block.

Soil moisture contents and groundwater levels

The initial moisture content at Plot 2 was approximately between 0.40 and 0.48 m^3/m^3 prior to the experiment (see Fig. 4.5). After the start of the experiment a response of moisture content occurred with depth, first reaction at 0.05 m and last, steep response at 0.40 m depth. At the end of the experiment the soil was most likely saturated at all measurements depths with soil moisture contents ranging from 0.52 to 0.55 m^3/m^3. After the experiment moisture contents in the upper layers (0.05 m and 0.10 m depth) gradually decreased and moisture contents in the deeper layers continued to increase very mild (0.20 m and 0.40 m). The trends of measured volumetric moisture contents correspond with the trends of the measured electrical conductivities (see Appendix III). One hour after the start of the experiment the groundwater level in the piezometers started to increase gradually from 113 to 57 cm below surface at the end of the experiment. One hour and ten minutes after the end of the experiment the water level was at its highest point (56 cm below surface) and started to decline gradually again. Fig. 4.5 also shows that the groundwater level responded earlier than the moisture content at 0.40 m depth.

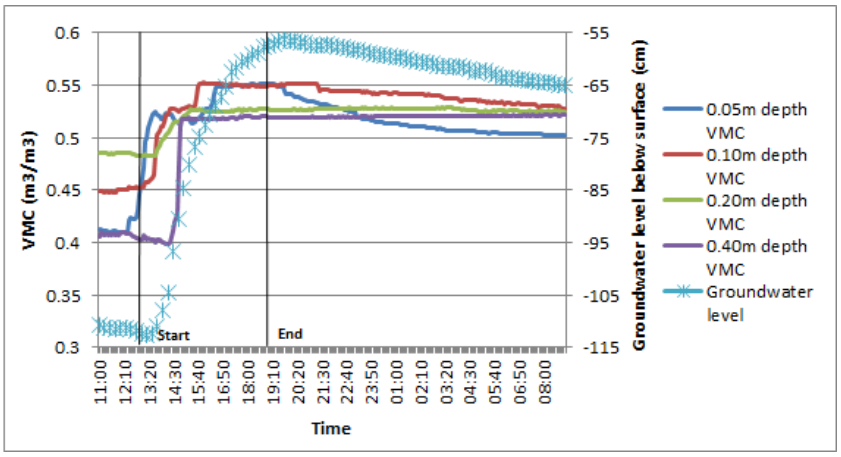

Fig. 4.5: Volumetric Moisture Content (VMC) in m3/m3 and groundwater level in cm below surface level at Plot 2.

Fig. 4.6 shows the wetting front curve for Plot 2 at four different depths over time. The wetting front curve shows that most storage was available in the topsoil until approximately 0.05 m - 0.10 m depth. The wetting front also shows the time of the largest response at each depth. At 0.5 m the largest response took place 1.5 hour after the start, at 0.1 m after 2 hours, at 0.3 m depth after 2.5 hours and at 0.40 m depth after 3 hours. After 5 hours soil moisture contents did not increase much anymore at all depths, probably because saturation of the soil was reached.

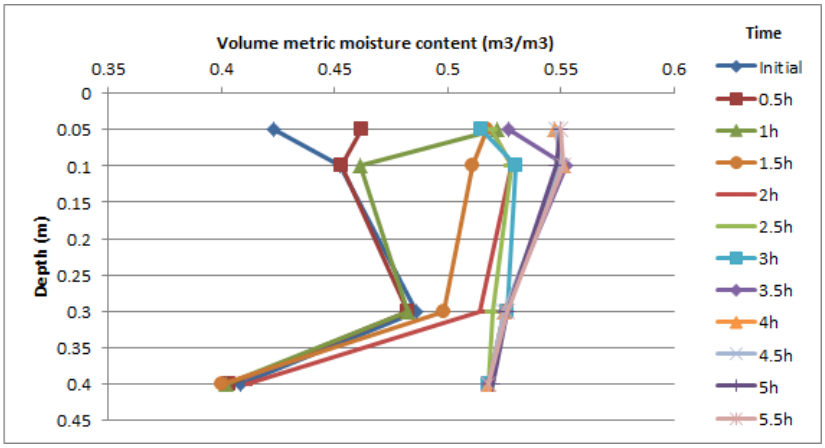

Fig. 4.6: Wetting front of volumetric moisture content in m^3/m^3 over depth in time steps of 30 minutes at Plot 2.

Electrical Resistivity Tomography

Fig. 4.7 shows the eight acquisition sets that were conducted before, during and after the rainfall experiment at Plot 2. Except for some spots the absolute resistivity outcomes do not clearly show a change in resistivity over time. The ratios of resistivity show that the sprinkler did not totally cover the right side of the plot and the same yields for the space surrounding the sprinkler in the middle of the plot. This spatial diversity in wetting is most likely caused by the heterogeneous spatial distribution of water from the sprinkler, which is also shown by the error bars in Fig. 4.4. The ratios also show that the topsoil of approximately 0.3 m gradually fills up and no preferential flow paths are visible. The resistivity in the plot did not change much after 20.8 hour (next morning).

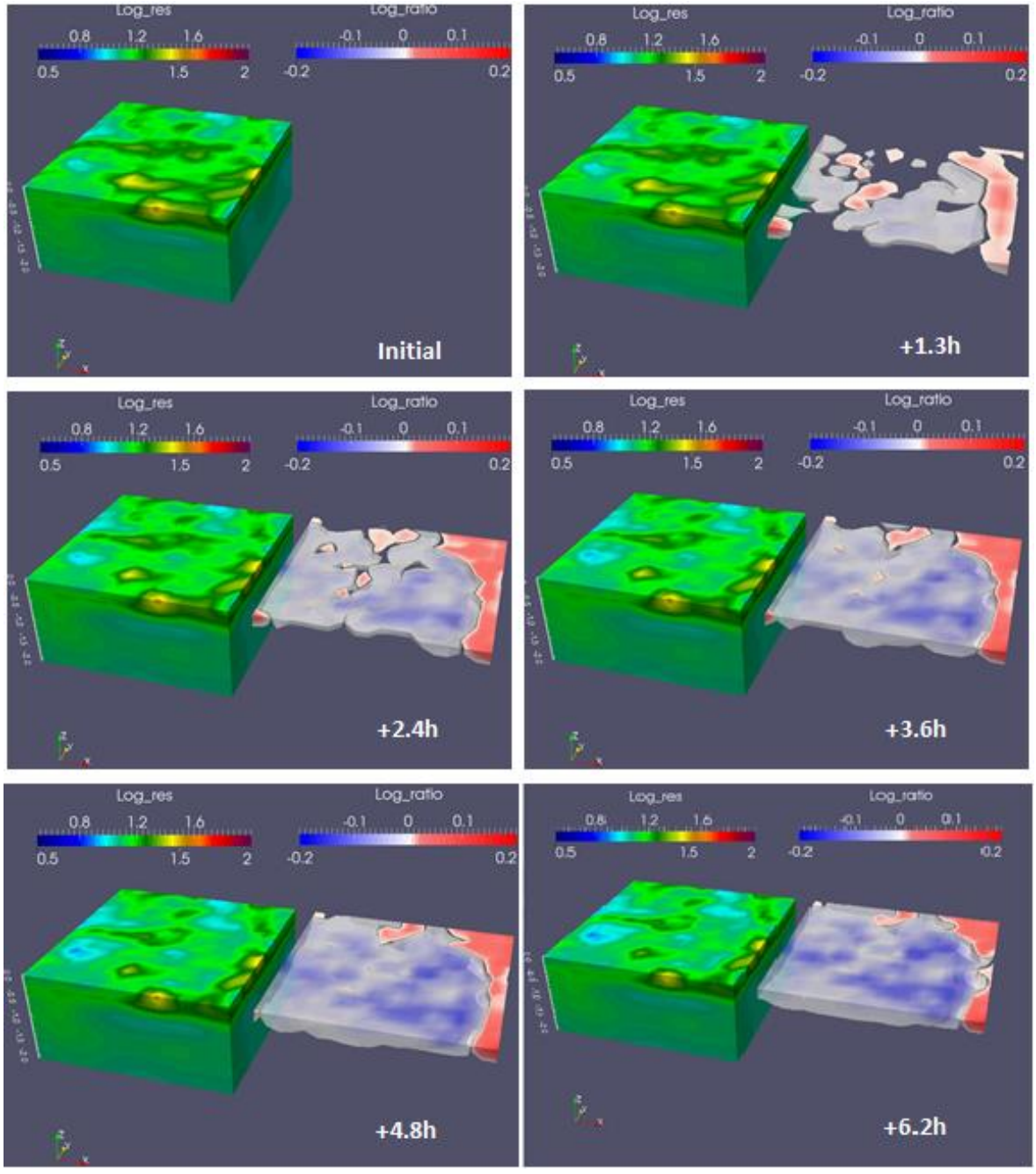

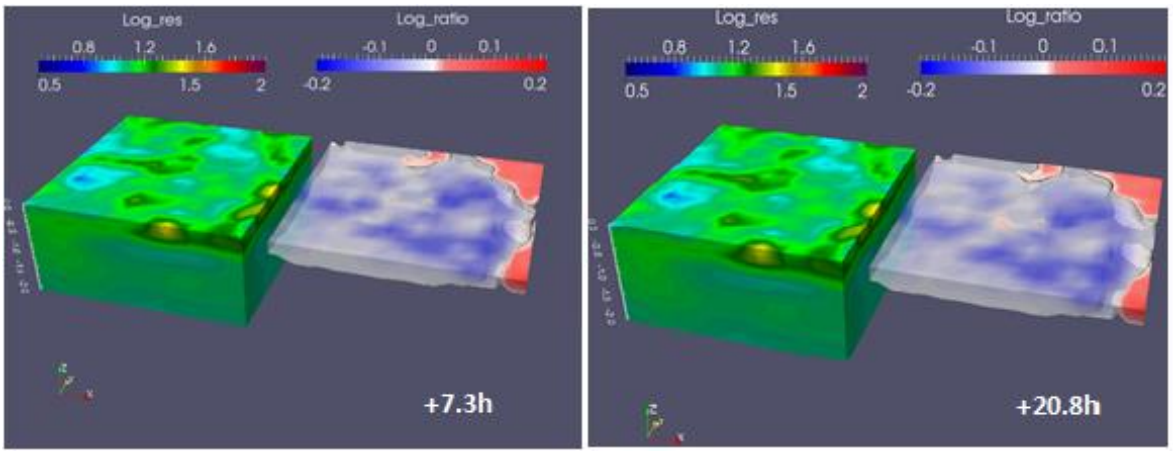

Fig. 4.7: Time serie of the ERT acquisition sets at Plot 2 with on each figure on the left the measured absolute resistivity in logarithm (Log_res) ranging from blue (wet) to red (dry). The right picture of each figure shows the ratio of the measured resistivity (logarithm) over the measured resistivity (logarithm) at the initial acquisition (Log_ratio) ranging from blue (wetter) to red (drier).

Hydrological analyses

The water balance in Table 4.2 shows that the change in storage is almost equal to the amount of the applied rainfall (103%). The 3% extra water can be caused by slow subsurface groundwater flow or the neglected evapotranspiration. The largest part of change in storage is found back in the increase of water level of 0.56 m (34.5%). The change in storage in the topsoil until 0.1 m below surface level is approximately 27.7%. Below this the change in storage is approximately 10% per 0.1 m.

Table 4.2: Water balance of Plot 2 with change in storage per layer (ΔS) calculated from the four volumetric moisture content (VMC) measurements and the change in groundwater level (Δh_g). The last column shows the ratio between the change in storage (ΔS) and the sprinkled water (P). The last row shows the total applied water, change in storage over all layers and the ratio of ΔS/P.

Plot 2	P [m³]	D [m]	θ_i [-]	θ_s [-]	ΔS [m3]	ΔS /P
VMC -0.05m		0.05	0.41	0.55	0.14	14.4%
VMC -0.1m		0.05	0.45	0.55	0.1	10.3%
VMC -0.2m		0.1	0.49	0.53	0.08	8.2%
VMC -0.4m		0.35	0.52	0.55	0.21	21.6%
Δh_s		0.56	0.52	0.55	0.336	34.5%
Total	0.973				1.002	***103%***

Interpretation

After the start of the experiment at Plot 2 a logical response in moisture content by depth took place and after the end of the experiment there was a gradual decrease in moisture content in the upper layers and a gradual increase in the lower layers. These mechanisms mostly indicate matrix infiltration, which is also visible in the ERT acquisitions. Nevertheless, the groundwater level responded before the response in moisture content at 0.4 m depth, which is remarkable and could be an indication of preferential flow paths. The largest storage found place in the organic topsoil (see also Appendix 1, Borehole 1).

4.3.2 Plot 3

Plot 3 is located on the WMF at the second scarp of the landslide. The site has a mild convex slope of approximately 3 degrees. The plot is fully covered with grass and contains 5 narrow surface fissures of a medium length from 40 cm to 100 cm and a medium depth from 20 cm to 40 cm. The aperture of the fissure was between 5 cm and 20 cm (see Fig. 4.8). On the plot 4 rain gauges, 4 Delta-T PR1 access tubes, 1 piezometer and 1 GS3 were installed. The fourth PR1 access tube was installed just downstream of the plot. The GS3 device was installed in the side of an open fissure on 0.05 m, 0.1 m, 0.2 m, and 0.3 m depth.

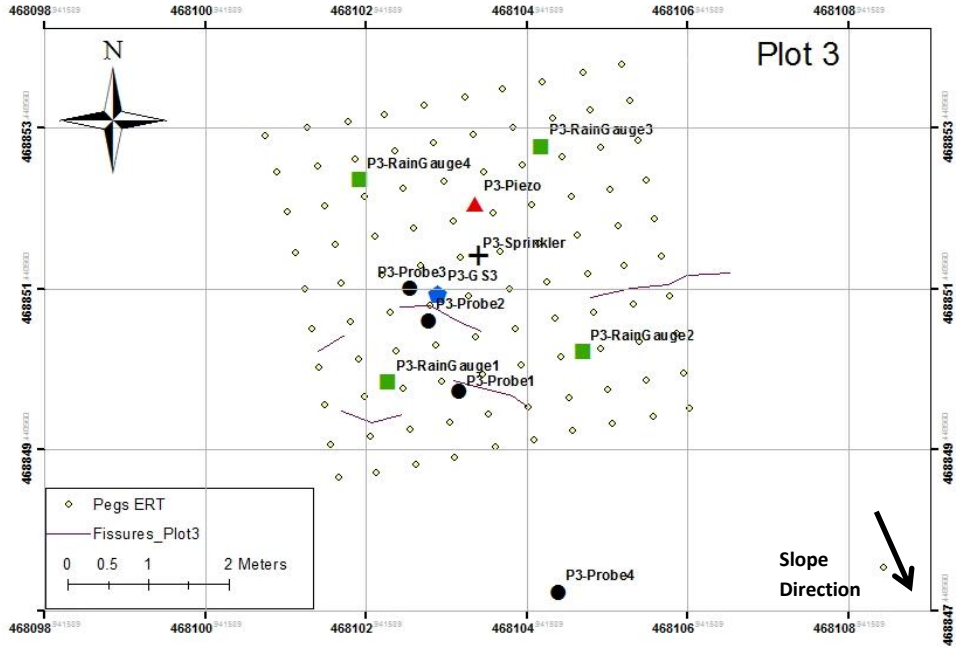

Fig. 4.8: Overview of the location, measurement devices and fissures of Plot 3.

The night before the sprinkling test weather remained dry and during the test one light rainfall occurred from 16:15 until 16:50 with approximately 1.5 mm rain. During the experiment the pressure was kept constant and average sprinkler rates were between 5 and 8 mm per half an hour. No overland flow was observed. Fig. 4.9 shows that the sprinkling rate remained relative constant thus no large differences in rainfall were measured in the four different rain gauges.

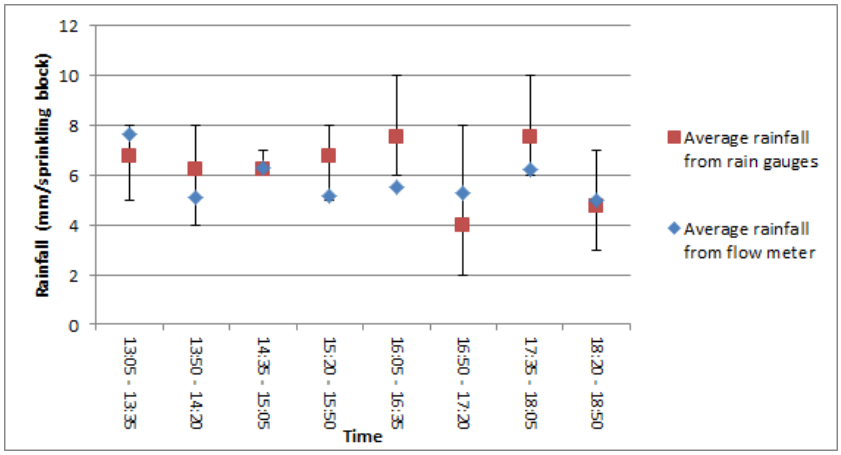

Fig. 4.9: Rainfall intensities from sprinkler at Plot 3, measured by rain gauges and flow meter in mm per block of sprinkling (30 minutes) with breaks of 15 minutes. The error bars show the minimum and maximum rainfall measured in the 4 rain gauges per sprinkling block.

Soil moisture contents and groundwater level

Fig. 4.10 shows that the initial soil moisture content in Plot 3 varied from 0.34 to 0.37 m^3/m^3, but a very fast response at all depths was observed after the start of the experiment. After the quick increase the graph shows a gradual increase in moisture contents until the end of the experiment. At the wettest moment (end of experiment) moisture contents range from 0.50 m^3/m^3 in the deeper clay ground (0.2 and 0.3 m depth) to 0.43 m^3/m^3 in the topsoil (0.05 and 0.1 m depth). After the sprinkling experiment was stopped moisture contents slowly decreased at all depths until 05:45 next morning, the time a rainfall occurred. The moisture content at 0.3 m depth shows two peaks that can be the result of the change in sprinkling intensity (see Fig. 4.9) or the result of wrong measurements, because the GS3 at 0.3 m depth later stopped working (after 21:45) due to unknown failure. The trends of measured volumetric moisture contents correspond with the trends of the measured electrical conductivities which are given in Appendix 2. The groundwater level started to increase 2 hour and 40 minutes after the start of the experiment from -120 cm to -90 cm below surface level at the end of the experiment (see Fig. 4.10). After the end of the experiment the groundwater level continued to increase for another approximately 5 or 6 hours until -83 cm the surface. After this the groundwater level gradually increased again to -85 cm at the next morning 04:45.

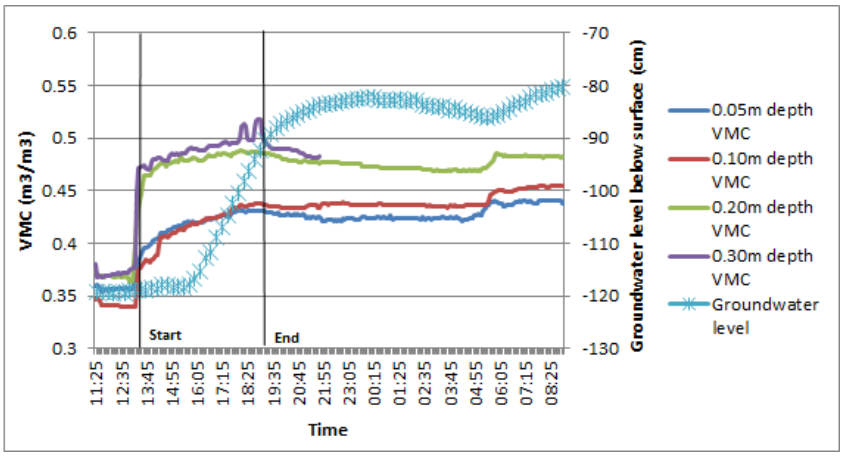

Fig. 4.10: Volumetric Moisture Content (VMC) in m^3/m^3 and groundwater level in cm below surface level at Plot 3.

Fig. 12 shows that the moisture content at all depths responded during the first half hour. After this first response the moisture contents at 0.05 and 0.1 m depth continued to increase slowly until 5 hours after the start of the experiment, at 0.20 and 0.30 m depth this increase was almost negligible.

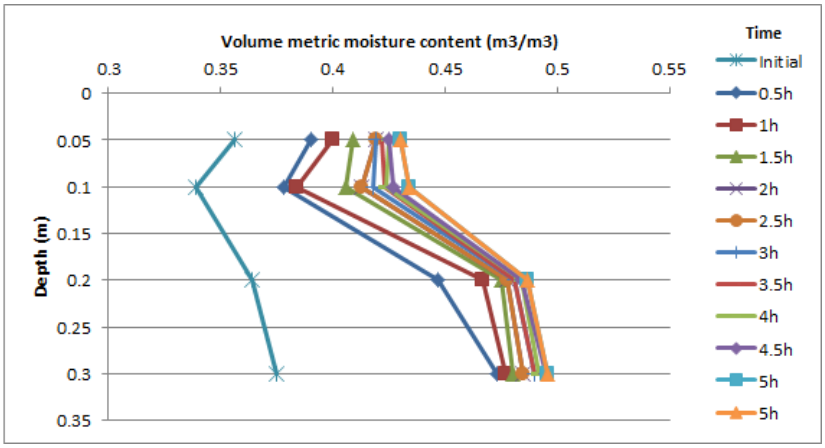

Fig. 4.11: Wetting front curve of volumetric moisture content in m^3/m^3 over depth in time steps of 30 minutes at Plot 3.

Electrical Resistivity Tomography

The initial ERT acquisition of Plot 3 shows that on the locations of the fissures (see also Fig. 4.8) the electrical resistivity is higher, meaning a drier soil. A possible explanation for this is that electrical pulses between pegs with fissures go through the air of the open fissures or have to go around the fissures, which causes higher resistivity. The side view of the resistivity measurements of each plot show a higher resistivity (lower water content) in the first 10 to 20 cm of the soil and a lower resistivity (higher water content) from 30 to 50 cm, this also corresponds with the wetting front curve in Fig. 4.12. After the start of the experiment the ratio of the first acquisition (+1h) shows quite some spatial differences, especially on the location of the fissures. During later acquisitions these spatial differences become smaller.

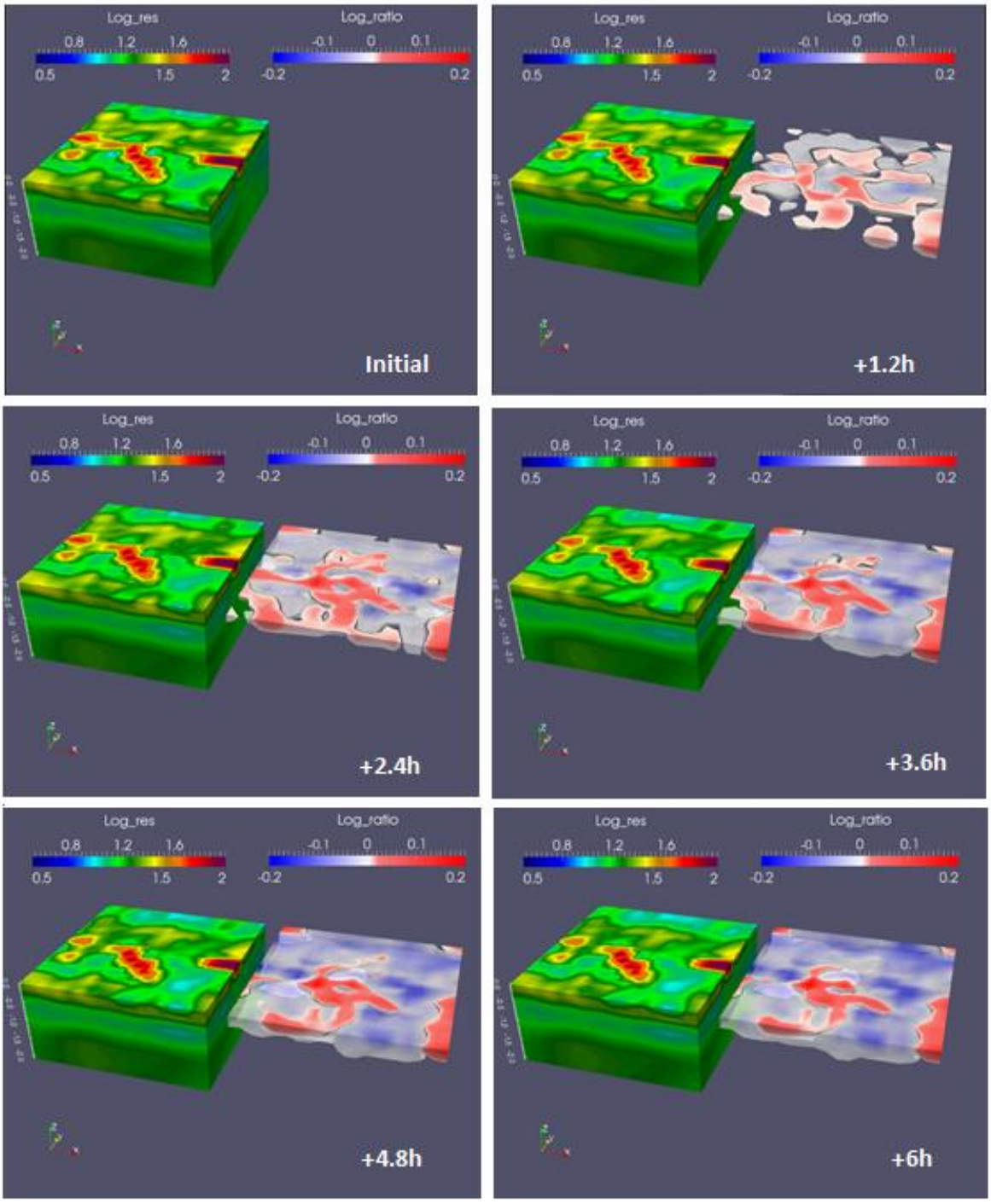

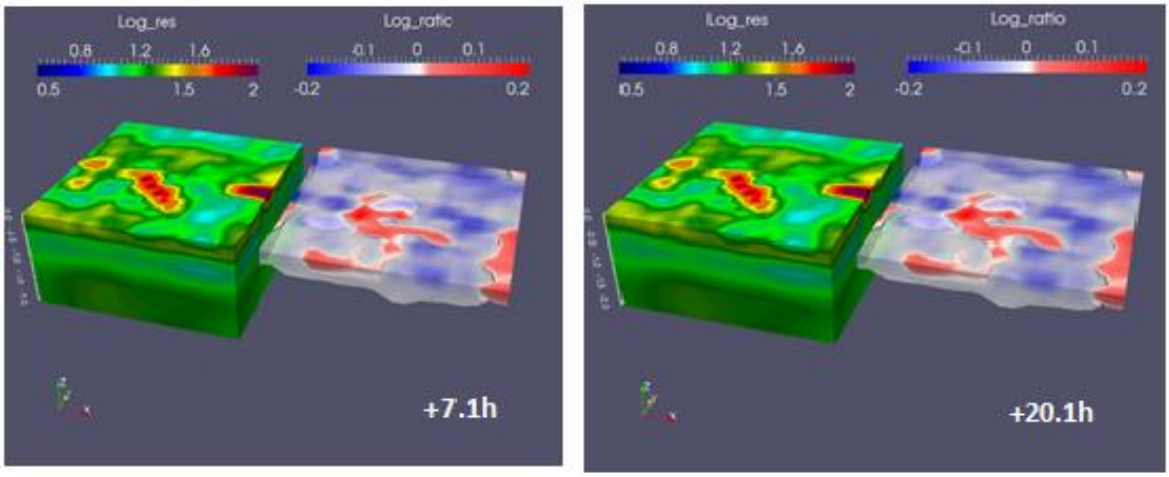

Fig. 4.12: Time serie of the ERT acquisition sets at Plot 3 with on each figure on the left the measured absolute resistivity in logarithm (Log_res) ranging from blue (wet) to red (dry). The right picture of each figure shows the ratio of the measured resistivity (logarithm) over the measured resistivity (logarithm) at the initial acquisition (Log_ratio) ranging from blue (wetter) to red (drier).

Hydrological analysis

The water balance of Plot 3 in Table 4.3 shows that approximately 92% of the applied water is found back in change in storage. The increase in groundwater level of 0.3 m caused a change in storage of approximately 19.5%. The largest change in storage took place in the unsaturated zone between 0.2 m and 0.9 m below surface level (45%). Nonetheless, the storage in the topsoil until 0.1 m below surface level was 0.17 m^3 and from 0.2 m to 0.9 m only approximately 0.07 m^3 per 0.1 m

Table 4.3: Water balance of Plot 3 with change in storage per layer (ΔS) calculated from the four volumetric moisture content (VMC) measurements and the change in groundwater level (Δh_g). The last column shows the ratio between the change in storage (ΔS) and the sprinkled water (P). The last row shows the total applied water, change in storage over all layers and the ratio of ΔS/P.

Plot 3	P [m³]	D [m])	θ_i [-]	θ_s [-]	ΔS [m3]	ΔS /P
VMC -0.05m		0.05	0.36	0.43	0.07	7.6%
VMC -0.1m		0.05	0.34	0.44	0.1	10.8%
VMC -0.2m		0.1	0.45	0.49	0.08	8.7%
VMC -0.3m		0.7	0.47	0.5	0.42	45.5%
Δh_g		0.3	0.47	0.5	0.18	19.5%
Total	0.924				0.85	***92%***

Interpretation

The soil moisture content measurements of Plot 3 show a very quick response with large increases at all depths. This mostly likely caused by the fact that the GS3 device was installed in the side of an open fissure, which was wetted from the side at all depths on the same time. After the first response a gradual increase took place followed by a gradual decrease of moisture content after the end of the experiment. This can presumably be explained by matrix flow. This same yields for the groundwater level that shows a logical delayed response. The spatial acquisition of the ERT do show some diversities in moisture content that could be an indication of preferential flow paths, but can also be the result of the spatial diversity in rainfall.

4.3.3 Plot 4

Plot 4 is located at the translating-prograding western lobe of WMF materials over the SSF (see Chapter 3.4). The plot is located on an uneven planar slope covered with grass and open parts due to fissures. The plot contains two large fissures of each 200 long, 10 cm aperture and 30 cm depth, which are almost connected. A third fissure is approximately 200 cm long, 20 cm wide and 30 cm deep (see Fig. 4.13). During the experiment it was very windy, which caused the sprinkled water to be blown to one direction. In order to counteract this, the sprinkler was moved from the middle of the plot to the side (see also Fig. 4.13), which caused a better spatial distribution of sprinkled water. Since it was still difficult to maintain an equal plot size and proper spatial distribution of sprinkled water, Plot 4 was also used to investigate what sprinkler rate/intensity would cause surface ponding.

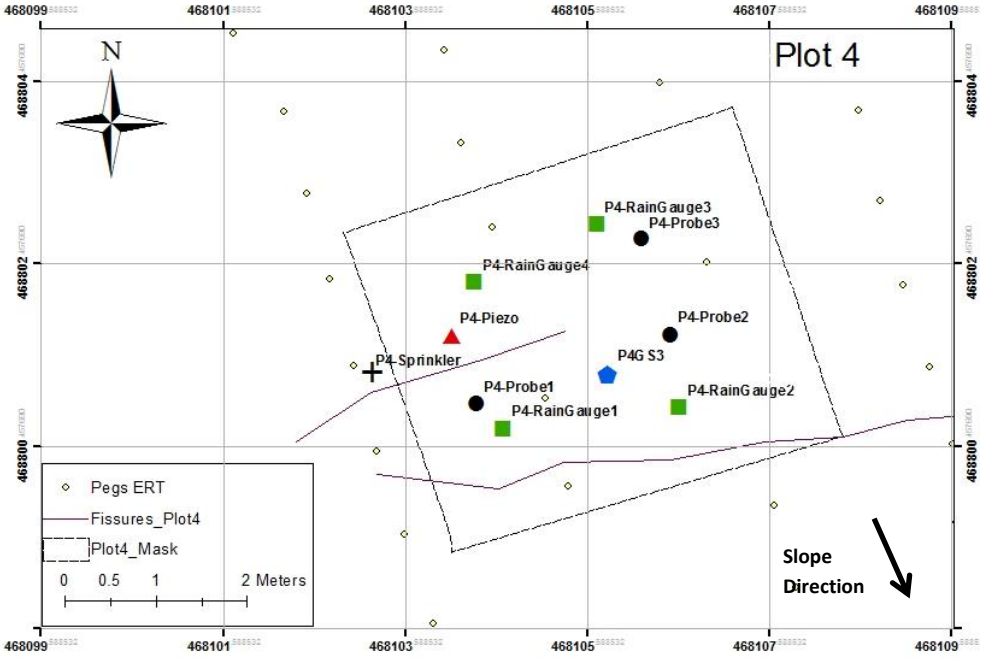

Fig. 4.13: Overview of the location, measurement devices and fissures of Plot 4 that is located in the existing ERT array. The mask shows the sprinkling area.

In the night preceding of the experiment approximately 5 mm of rainfall was measured. During the experiment the weather was cloudy and dry, but very windy. The experiment was performed in 4 sprinkling blocks (see Fig. 4.14). The intensity during the first block was adjusted to approximately 10 mm per half an hour and the error bars show that the spatial distribution remained relatively equal. During the second block from 11:00 to 12:00 the intensity was increased to an average of 55 mm per hour (calculated from the flow meter), but the error bars showed a very high spatial diversity with deviations of 30 mm. The very high intensity caused light surface ponding of several millimetres, but no overland flow occurred even though the soil was already quiet saturated from the night before.

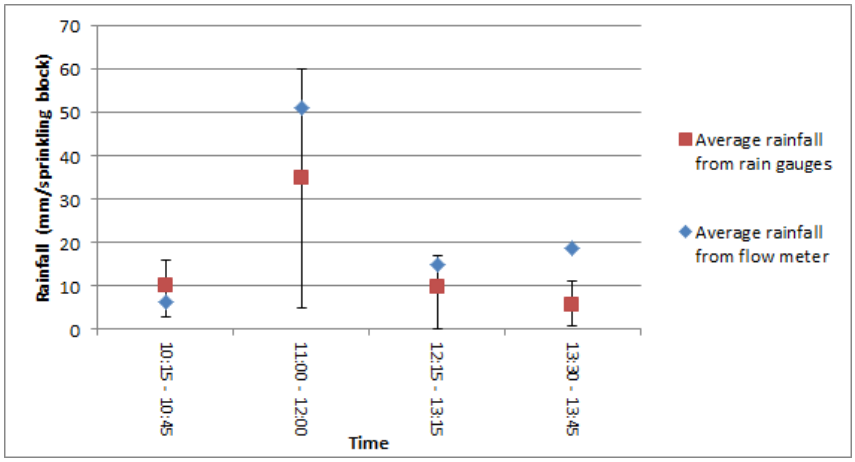

Fig. 4.14: Rainfall intensities from sprinkler at Plot 4, measured from rainfall meters and flow meter in mm per block of sprinkling (1 hour) with breaks of 15 minutes (except last block from 13:30 – 13:45). The error bars show the minimum and maximum rainfall measured in the 4 rain gauges.

Soil moisture contents and groundwater level

Fig. 4.15 shows that the initial moisture contents were approximately 0.51, 0.46, 0.49 and 0.5 m^3/m^3 on respectively 0.1, 0.2, 0.3 and 0.5 m depth. Quickly after the start of the experiment the different depths responded (one after each other) from 0.1 m depth onward, with a very little response at 0.5 m depth. After the first response moisture contents did not increase much more. After the experiment was stopped, the moisture contents at 0.1 m and 0.2 m depth started to decrease slowly and moisture contents at 0.3 m and 0.5 m depth continued to increase. Groundwater level monitoring revealed a deep groundwater level at approximately 180 cm below surface level that did not change during the experiment.

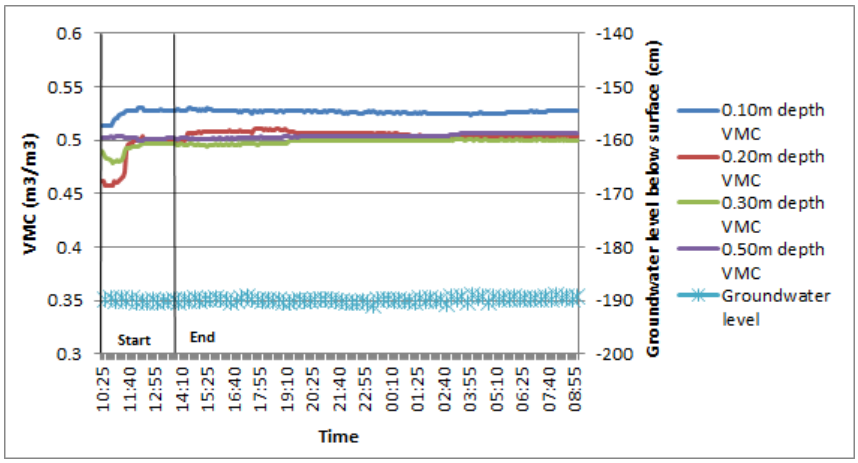

Fig. 4.15: Volumetric Moisture Content (VMC) in m^3/m^3 and groundwater level in cm below surface level at Plot 4.

The wetting front curve of Plot 4 in Fig. 4.16 shows that at all depths moisture contents increased after the start of the experiment, except at 0.5 m depth. The increases in moisture contents were relatively small at 0.1 m and 0.3 m depth (approximately 0.02 m^3/m^3) and a little bit larger at 0.2 m depth (0.03 $m^3/^3$). The figure also shows that the largest increase took place at 0.2 m depth during the sprinkling block from 11:00 to 12:00 with the high intensity.

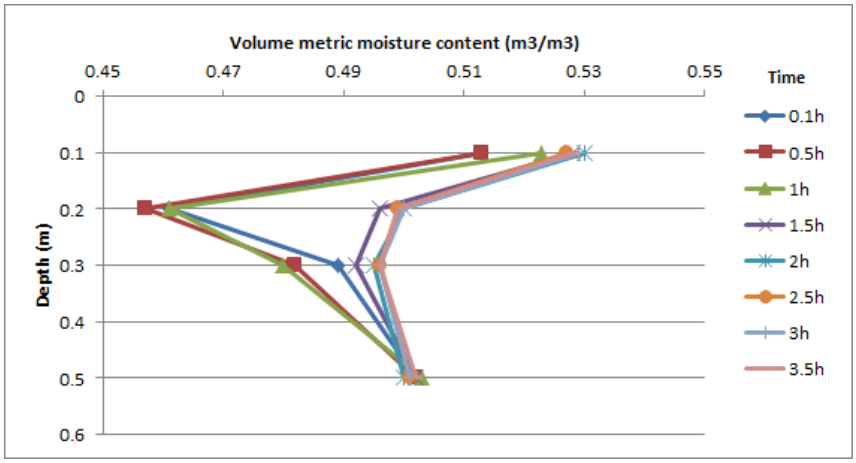

Fig. 4.16: Wetting front curve of volumetric moisture content in m^3/m^3 over depth in time steps of 30 minutes at Plot 4.

Electrical Resistivity Tomography

Plot 4 was located in the existing ERT array of the BGS, therefore no extra ERT was installed during the experiment. However, the results of the existing ERT measurement could not be downloaded and processed due to time limitations.

Hydrological analysis

Table 4.4 shows that only 31.2% of the applied rainfall was found back in change in storage in Plot 4. All measured change in storage took place in the unsaturated zone (31.2%). The topsoil until 0.1 m below surface level stored approximately 0.04 m^3 and the topsoil from 0.1 m to 0.2 m 0.1 m^3. Below this, the change in storage per 0.1 m decreased again to 0.064 m.

Table 4.4: Water balance of Plot 4 with change in storage per layer (ΔS) calculated from the four volumetric moisture content (VMC) measurements and the change in groundwater level (Δh_g). The last column shows the ratio between the change in storage (ΔS) and the sprinkled water (P). The last row shows the total applied water, change in storage over all layers and the ratio of ΔS/P.

Plot 4	P [m³]	D [m]	θ_i [-]	θ_s [-]	ΔS [m3]	ΔS /P
VMC -0.1m		0.1	0.51	0.53	0.04	4.4%
VMC -0.2m		0.1	0.46	0.51	0.1	11%
VMC -0.3m		0.2	0.48	0.5	0.08	8.8%
VMC -0.5m		1.6	0.5	0.502	0.064	7%
Δh_g		0	-	-	-	0%
Total	0.910				0.284	***31.2%***

Interpretations

Soil moisture content measurements show after the first response only a slight increase, because the soil at this depth was most likely already close to saturation due to antecedent rainfall. Also compared with the previous two plots the moisture content values at start of the experiment already indicated a near saturated situation. Since the accuracy of the GS3 device is approximately 0.03 m^3/m^3 and the measured changes were lower than this, the changes can actually be neglected. Only 31.2% of the applied water is found back in change in storage in the unsaturated zone, which can have several explanations. A first explanation for this is that the water balance assumes that the unsaturated zone from 0.3 m below surface level until the water level at 1.8 m below surface level is homogeneous (saturated as at measurement depth 0.5 m) and therefore less change in storage is calculated than actually occurred. A second explanation is that a perched water table is located

above the measured water table, because the borehole profiles (Appendix 1) also show a sandy layer from 130 until 170 cm below surface level. Another possible cause is the fact that Plot 4 is located on a relatively steep slope (approximately 12%), which made it possible that all water drained as subsurface flow out of the plot before it reached the groundwater. Finally, the water can also be drained quickly by fissure flow. Nevertheless, the experiment at this Plot 4 also experienced other uncertainties as the large variations in sprinkling intensities and the location of the sprinkler, which caused a high spatial heterogeneity of rainfall at the plot (visually observed). Unfortunately this cannot be checked due to the missing ERT measurements.

4.3.4 Plot 5

Plot 5 is located on the scarp of the translational-prograding eastern lobe in the WMF. In the plot are 5 fissures of approximately 50 to 200 cm and 1 large fissure with a length of 650 cm and a maximum aperture of 80 cm (see Fig. 4.17). In the plot 3 Delta-T PR1 access tubes, 1 deep piezometer of 5 meters, 1 shallow piezometer of 2.5 meters, 4 rain gauges and 1 GS3 on 0.1, 0.2, 0.3, 0.5 m depths were installed.

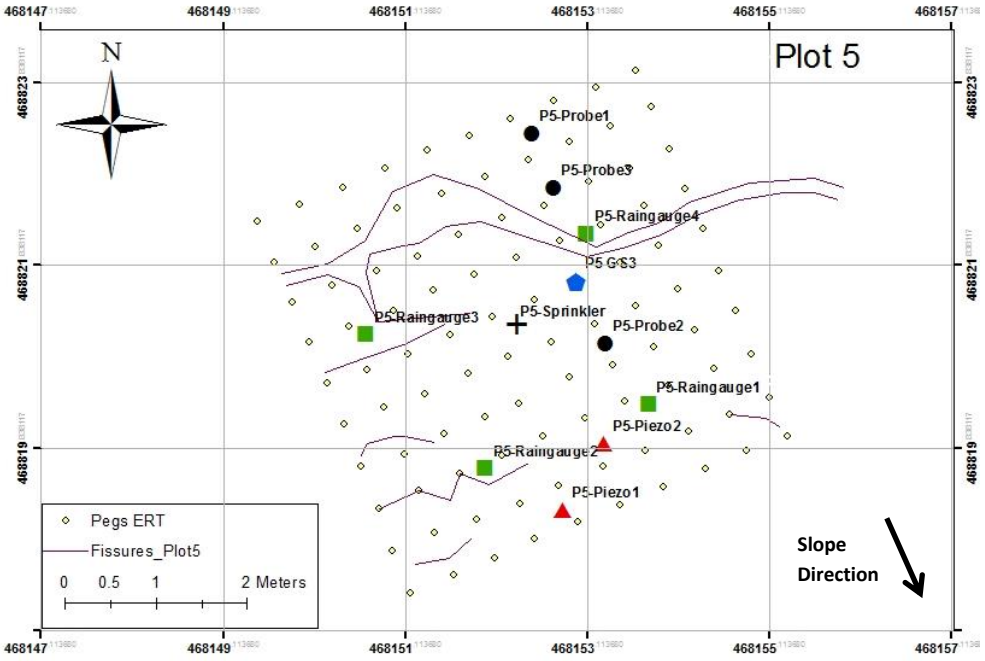

Fig. 4.17: Overview of the location, measurement devices and fissures of Plot 5.

Before the start of the experiment approximately 3.5 mm rainfall was measured and during the experiment itself another 4.5 mm of natural rainfall including a hail storm was observed. The weekend before the experiment, from Friday evening until Monday morning it was also very wet with approximately 14 mm rainfall. Due to time limitations the sprinkling blocks had to be increased to 1 hour with 15 minutes breaks.

Fig. 4.18 shows that the average intensity ranged from 9 to 15 mm per hour with large spatial diversities during the third and fourth blocks (error bars of 8 mm). At the end of the experiment small puddles of water with increased salinities were observed at approximately 5-7 meter downslope of the plot. These puddles most likely developed due to exfiltration.

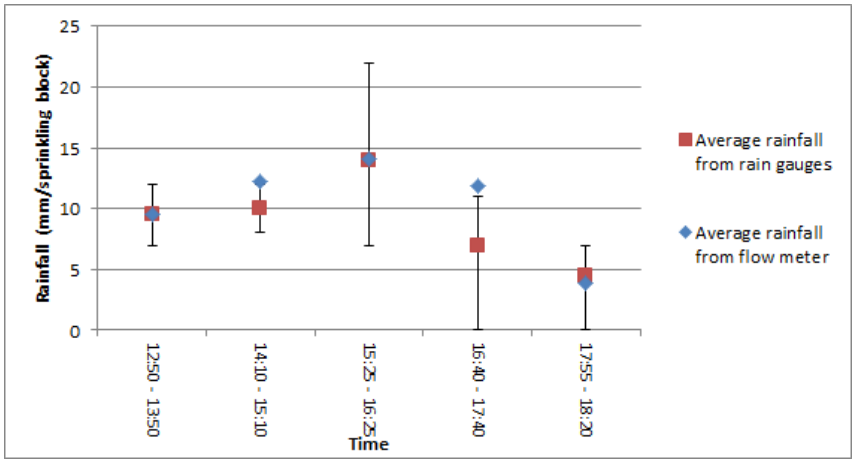

Fig. 4.18: Rainfall intensities from sprinkler at Plot 5, measured from rainfall meters and flow meter in mm per block of sprinkling (30 minutes) with breaks of 15 minutes (except last block from 17:55 – 18:20). The error bars show the minimum and maximum rainfall measured in the 4 rain gauges.

Soil moisture contents and groundwater levels

The monitored volumetric moisture contents in Plot 5 barely show a response to the sprinkled water (see Fig. 4.19). Moisture contents ranged from 0.51 m^3/m^3 in the deeper layers to 0.54 m^3/m^3 in the topsoil. Rainfall events antecedent of the sprinkler experiment caused the groundwater level to increase before the sprinkler test had started. At the start of the experiment the measured groundwater level was relatively close to surface at a depth of 43 cm, but during the installation of the piezometer groundwater was also found at depth of 140 and 170 cm (see Appendix 1). The effect of sprinkling is visible after approximately 30 minutes after the start of the test. Groundwater level increased with 7 cm to approximately 33 cm below surface level. Just before the end of the test the groundwater level decreased again to -38 cm at the end of the test.

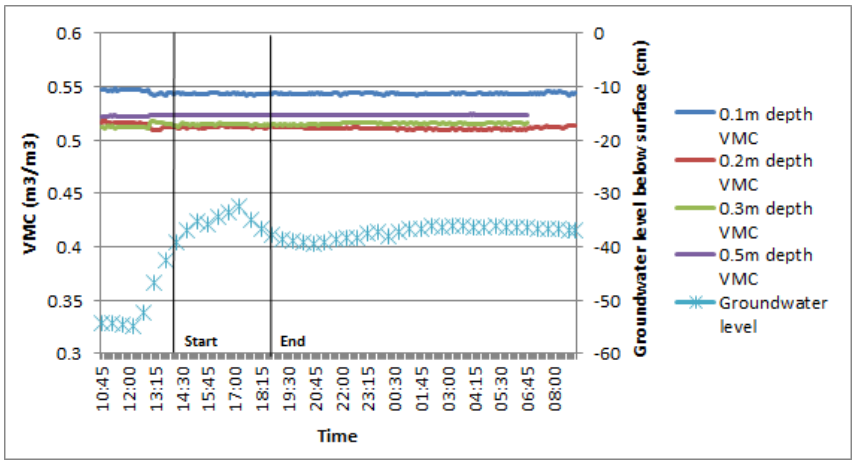

Fig. 4.19: Volumetric Moisture Content (VMC) in m^3/m^3 and groundwater level in cm below surface level at Plot 5.

The wetting front curve in Fig. 4.20 also shows that no response of volumetric moisture content was measured over the four depths and that the topsoil at 0.1m depth consists of relatively high moisture content.

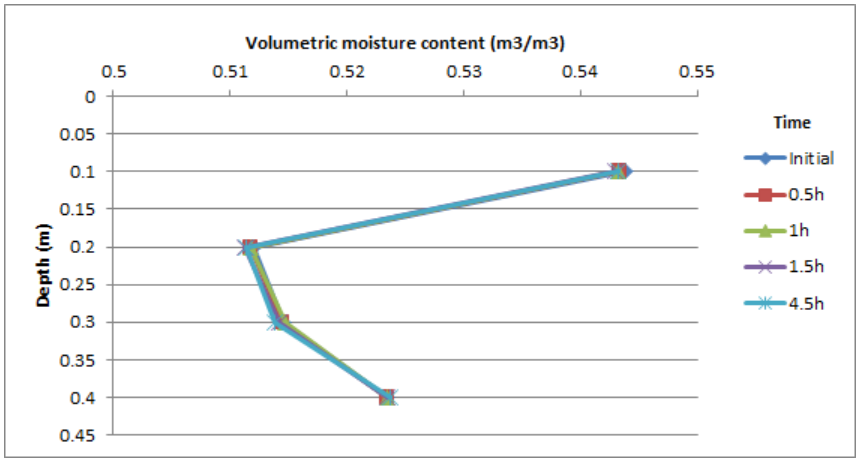

Fig. 4.20: Wetting front curve of volumetric moisture content in m^3/m^3 over depth in time steps of 30 minutes at Plot 5.

Electrical resistivity Tomography

At Plot 5 six ERT acquisitions were conducted, one up front of the experiment, three during and one the after the experiment. The absolute ERT acquisitions show much heterogeneity with in certain areas higher resistivity values. These areas are however not remarkable in the figures with the ratios and thus show less change over time. The ERT acquisitions also show a blue lens between 0.75 and 1.5 m depth with low electrical resistivity. The different ratios over time show a red area with a positive ratio in the middle of the plot (area became drier during experiments). The ratios also show a gradually filling up of the topsoil.

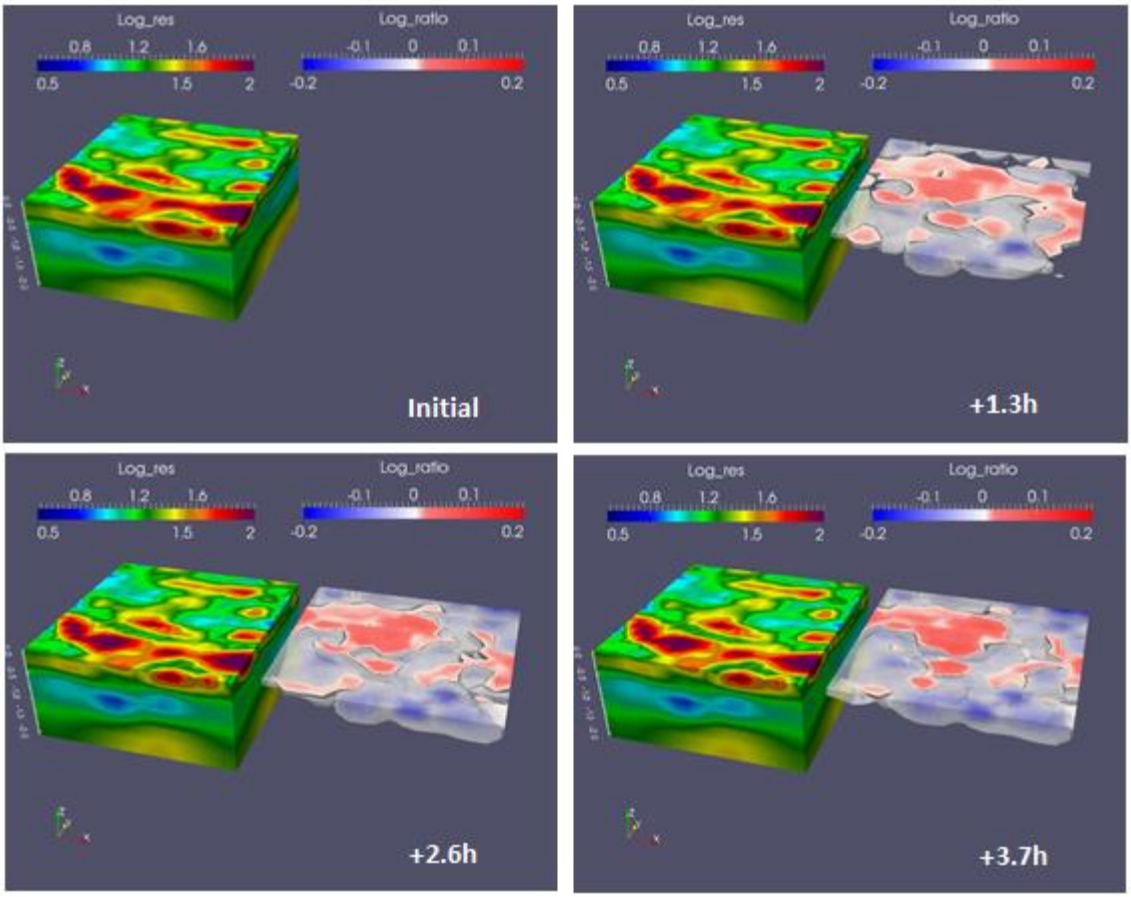

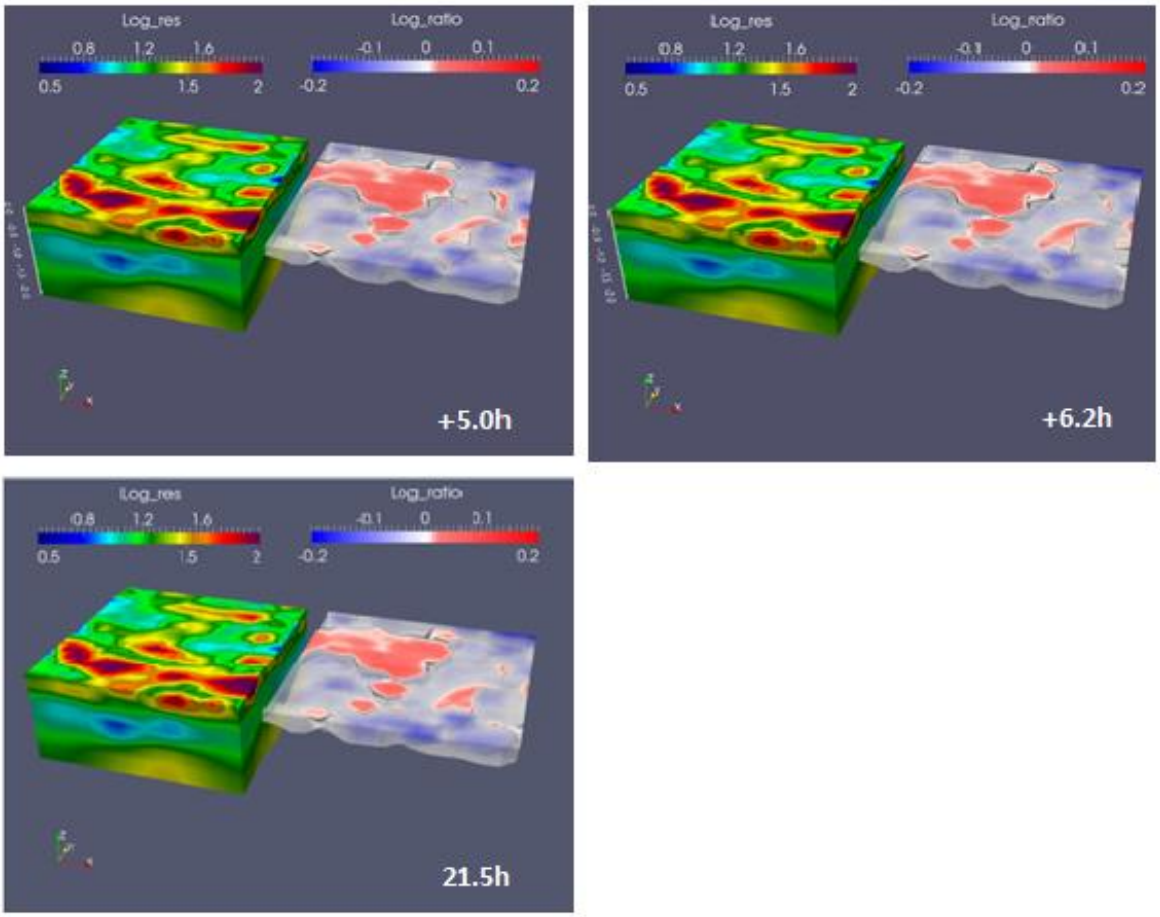

Fig.4.21: Time series of the ERT acquisition sets at Plot 5 with on each figure on the left the measured absolute resistivity in logarithm (Log_res) ranging from blue (wet) to red (dry). The right picture of each figure shows the ratio of the measured resistivity (logarithm) over the measured resistivity (logarithm) at the initial acquisition (Log_ratio) ranging from blue (wetter) to red (drier).

Hydrological analysis

Table 4.5 shows that in Plot 5 only 2.9% of the applied rainfall is found back in the change in storage, which is a result of the increase in groundwater level of 5 cm.

Table 4.5: Water balance of Plot 5 with change in storage per layer (ΔS) calculated from the four volumetric moisture content (VMC) measurements and the change in groundwater level (Δh_g). The last column shows the ratio between the change in storage (ΔS) and the sprinkled water (P). The last row shows the total applied water, change in storage over all layers and the ratio of ΔS/P.

Plot 5	P [m³]	D [m]	θ_i [-]	θ_s [-]	ΔS [m3]	ΔS /P
VMC -0.1m		0.1	0.54	0.54	0	0%
VMC -0.2m		0.1	0.51	0.51	0	0%
VMC -0.3m		0.1	0.51	0.51	0	0%
VMC -0.5m		0	0.52	0.52	0	0%
Δh_g		0.05	0.5	0.53	0.03	2.9%
Total	1.034				0.03	***2.9%***

Interpretation

Due to rainfall before the start of the experiment at Plot 5 the groundwater level already had started to increase, but another response/increase was measured during the experiment and in especial when the sprinkling intensity was increased (around 15:25). The decrease in groundwater level before the end of the experiment is also a strong indication for fissure drainage behaviour. The ERT acquisitions show higher electrical resistivity values (drier soil) around the locations of the fissures, but this can also be caused by spatial heterogeneity of the rainfall. The blue lens, visible deeper in the soil, in the ERT measurements is most likely the perched water table that is measured during the sprinkler experiment (other water table found between 140 and 170 cm below surface level, see Appendix II). The water balance only shows a change in storage of 2.9%. As described earlier exfiltration was observed downstream from Plot 5 during the experiment, thus the low change in storage or small groundwater level increase could be caused by a lateral subsurface flow or by the other explanations described in Plot 4: Interpretation.

4.3.5 Plot 6

The last plot is located on the translational WM, just above the SSF. The plot is located on a planar surface which is slightly tilted to the west-south. In this plot no fissures were observed and 4 rain gauges, 1 piezometer, 1 Delta-T PR1 access tubes and 1 GS3 device on 0.1, 0.2, 0.3 and 0.5 m depth were installed.

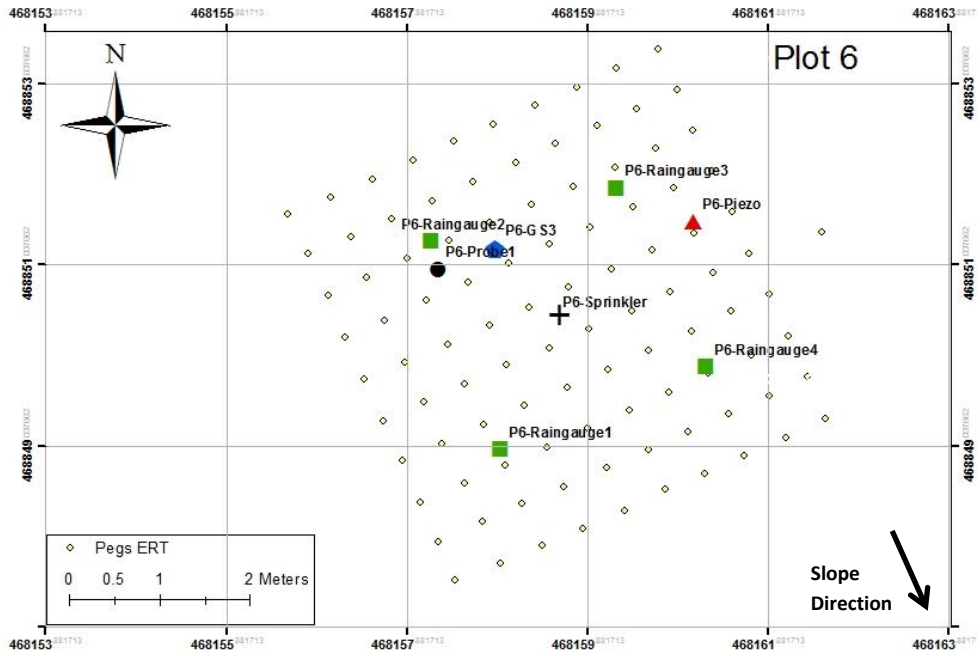

Fig.4.22: Overview of the location and measurement devices of Plot 6.

After the wet days before and during the experiment at Plot 5 it also rained the night antecedent of the experiment at Plot 6 approximately 3.7, but during the sprinkling test it remained dry and sunny. The sprinkling test at Plot 6 consisted of 1 contiguous block from 13:15 until 15:30 without breaks. Fig. 4.23 shows that the average sprinkler intensity was approximately 10 to 12 mm per hour and spatial differences were not more than 2 mm.

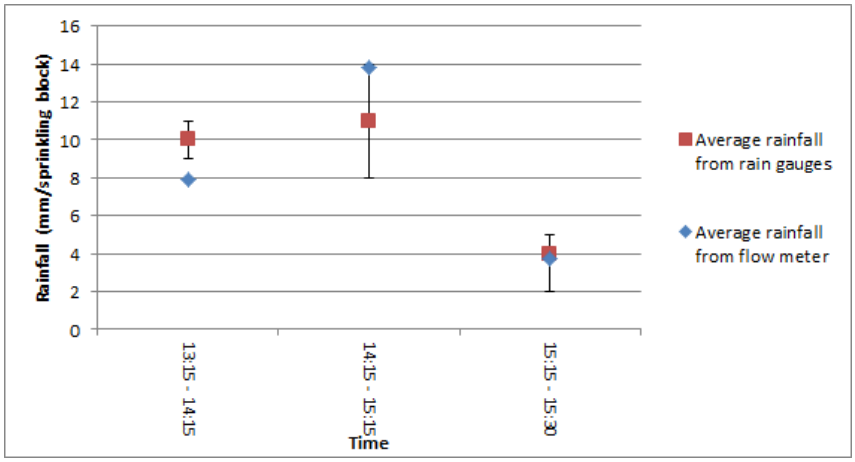

Fig. 4.23: Rainfall intensities from sprinkler at Plot 6, measured from rainfall meters and flow meter in mm per block of sprinkling (1 hour, except last block, which was from 15:15 until 15:30) without break. The error bars show the minimum and maximum rainfall measured in the 4 rain gauges.

Soil moisture contents and groundwater level

The initial moisture contents at Plot 6 ranged from approximately 0.46 to 0.50 m^3/m^3 (see Fig. 4.24). Almost immediately after the start of the experiment a slow gradual increase in moisture contents occurred that lasted until the end of the experiment. After the end of the experiment the moisture content at 0.1 m depth was approximately 0.51 m^3/m^3 and subsequently started to decrease very slowly. At 0.3 m depth the moisture content was approximately 0. 49 m^3/m^3 and remained at this value until the end of the measurements next morning. Due to unknown causes the GS3 at depth 0.1 and 0.5 m stopped working after 16:00. Fig. 4.24 shows that the monitored groundwater level responded approximately 90 minutes after the start of the experiment and increased from 108 cm to 104 cm below surface level at the end of the experiment. During the 105 minutes after the end of the experiment the groundwater level continued increasing to 98 cm below surface level. 105 minutes after the end of the experiments the groundwater level started to decrease gradually until next morning to 115 cm below surface level. The first response of groundwater level, 90 minutes after the start of the experiment was before the moisture content at 0.3 m depth reached saturation.

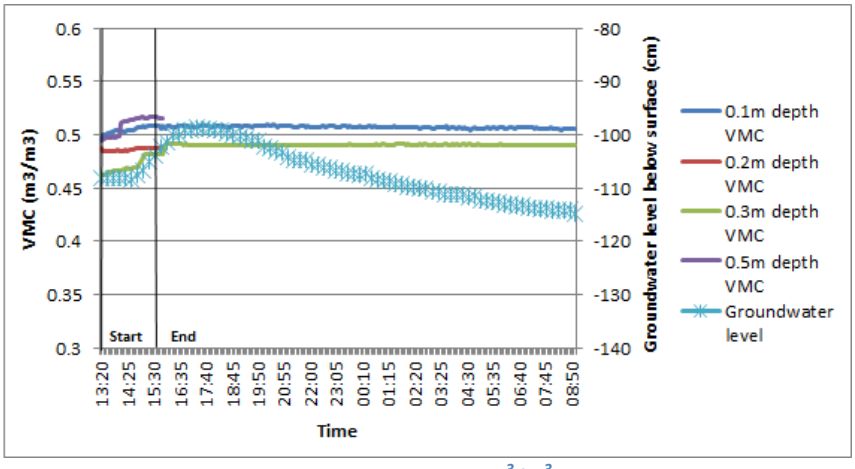

Fig. 4.24: Volumetric Moisture Content (VMC) in m^3/m^3 and groundwater level in cm below surface level at Plot 6.

The wetting front curve of Plot 6 in Fig. 4.25 shows moisture content measurements in a rotated triangle shape. At 0.1 m depth the moisture content is relatively high (0.51 m^3/m^3), below this it decreases until 0.3 m depth to 0.46 m^3/m^3 and after this the moisture content increases again to 0.51 m^3/m^3. Moreover the increase in moisture contents over time becomes larger by depth.

Another interesting point is that the moisture content at 0.5 m depth responses earlier (after 1h) than the moisture content at 0.3 m depth (after 2.5h). This could also be a result of preferential flow.

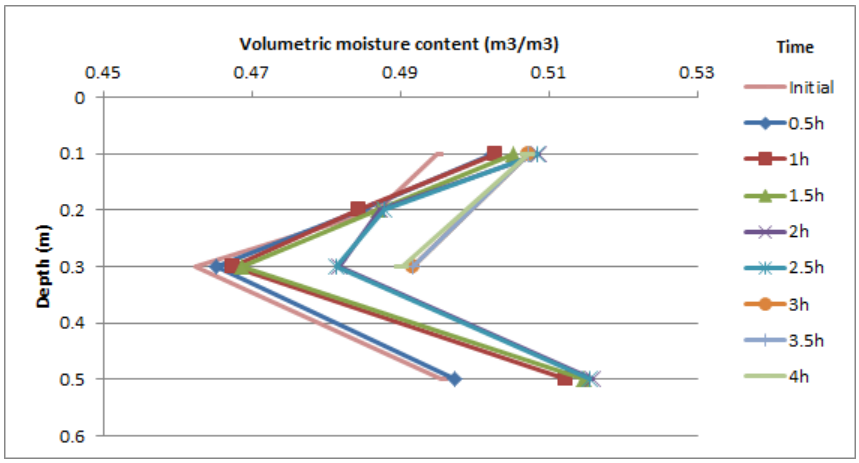

Fig. 4.25: Wetting front curve of volumetric moisture content in m^3/m^3 over depth in time steps of 30 minutes at Plot 6.

Electrical Resistivity Tomography

Plot 6 on the last day of the experiments only lasted for a bit more than 2 hours thus one acquisition was conducted before the experiment, one during and one after the experiment. The three electrical resistivity acquisitions show a drier topsoil (green) with a thin wetter lens (yellow) underneath it that lies on a drier soil again (green). Below this a blue lens is located between 0.75 and 1.5 m depth that indicates a wetter zone again. The ratios show a red area in the middle of the plot again with increased resistivity, which is most likely caused by heterogeneous area of the sprinkler again.

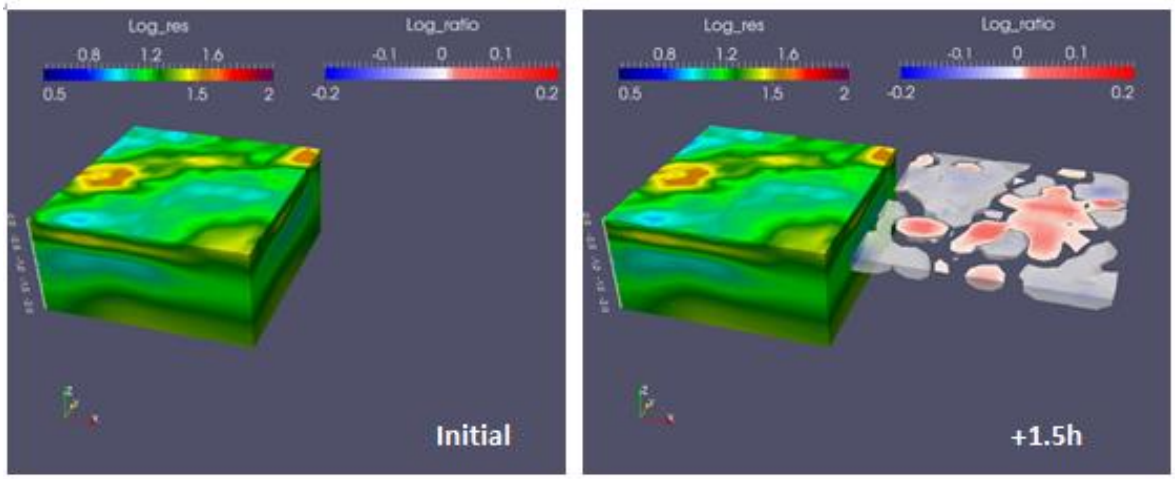

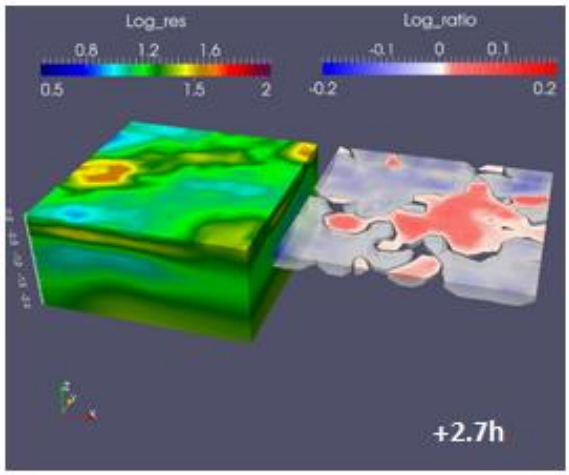

Fig. 4.26: Time series of the ERT acquisition sets at Plot 6 with on each figure on the left the measured absolute resistivity in logarithm (Log_res) ranging from blue (wet) to red (dry). The right picture of each figure shows the ratio of the measured resistivity (logarithm) over the measured resistivity (logarithm) at the initial acquisition (Log_ratio) ranging from blue (wetter) to red (drier).

Hydrological analysis

The water balance of Plot 6 shows that approximately 80% of the applied rainfall is found back in change in storage (see Table 4.6). The largest part of the applied rainfall is found back in the change in storage of the unsaturated zone between 0.3 m and 1.04 m below surface level (58.8%). In this part the change in storage is approximately 0.04 m^3 per 0.1 m. In the first 0.1 m and second 0.1 m the change in storage is only 0.02 and 0.01 m^3 respectively. The increased ground water level of 4 cm caused a change in storage of 3.9%.

Table 4.6: Water balance of Plot 6 with change in storage per layer (ΔS) calculated from the four volumetric moisture content (VMC) measurements and the change in groundwater level (Δh_g). The last column shows the ratio between the change in storage (ΔS) and the sprinkled water (P). The last row shows the total applied water, change in storage over all layers and the ratio of ΔS/P.

Plot 6	P [m³]	D [m]	θ_i [-]	θ_s [-]	ΔS [m3]	ΔS /P
VMC -0.1m		0.1	0.5	0.51	0.02	3.9%
VMC -0.2m		0.1	0.485	0.49	0.01	2%
VMC -0.3m		0.1	0.46	0.49	0.06	11.8%
VMC -0.5m		0.74	0.495	0.515	0.296	58.3%
Δh_g		0.04	0.5	0.525	0.02	3.9%
Total	0.508				0.406	***80%***

Interpretation

The rotated triangle shape of measured moisture contents (high to low and to high again) is quite remarkable. It could be caused by different layers of soil with different soil properties, resulted from the translational flows. Another explanation could be the antecedent rainfall, which infiltrates by matrix flow as a lens (yellow lens in ERT) to the groundwater. The response in groundwater level 90 minutes after the start of the experiment and the response of moisture content at 0.5 m depth were before the response in soil moisture content at 0.3 m depth and could therefore indicate preferential flow.

4.4 Analysis of observed natural groundwater dynamics

Fig. 4.27 shows the one month groundwater level measurements in natural logarithm scale (primary y-axis) and linear scale (secondary y-axis) for every plot. For each plot several drawdown parts are used to calculate the decay constants (see Chapter 4.2.4, equation 4.7). Krzeminska (2012) assumed that the steeper segments of the drawdown curves indicate faster drainage that represent preferential flow and the milder slopes of the curve indicate slower drainage that represent matrix flow (see also Chapter 2.1). Based on this theory, the five different plots with all own fissure properties, and geomorphological and hydrological characters can be compared.

When looking at the one month time series it can be observed that at Plot 2, 3 and 5 groundwater levels show much quicker increases and drawdowns than Plot 4 and 6. This is logical because the groundwater levels at Plot 4 and 6 are deeper located (approximately 100 to 195 cm below surface level) and most likely less to not influenced by fissures anymore. At Plot 2, 3 and 5 the groundwater levels are roughly located on the same depth (50 to 100 cm below surface level). Comparing the drawdown segments of the three different plots it can be obtained that Plot 2, where no fissures were observed, shows milder slopes and larger decay factors. The graphs of Plot 3 and 5 show that the fast drawdowns are mostly observed when groundwater levels closer to surface level, above approximately 60 cm below surface level. This is most likely related to the depth of the fissures at the plots that ranged from 20 to 40 cm.

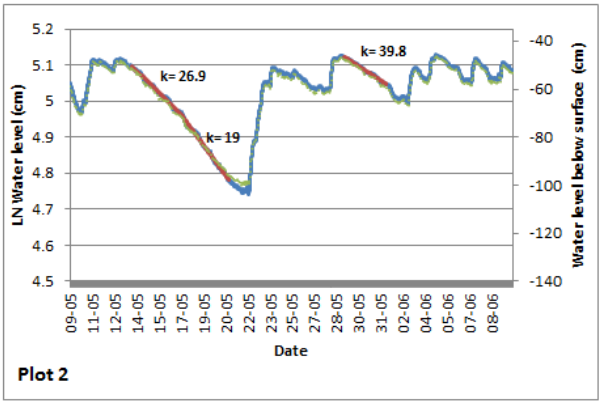

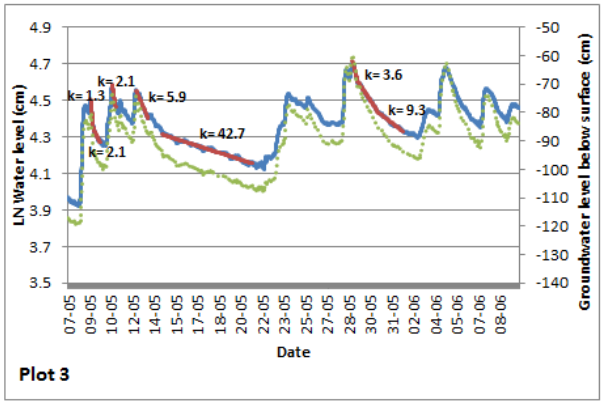

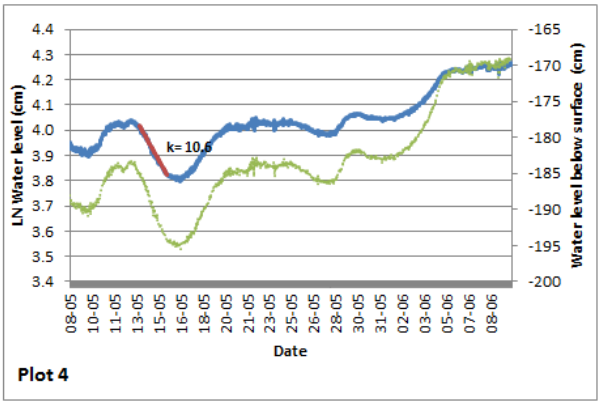

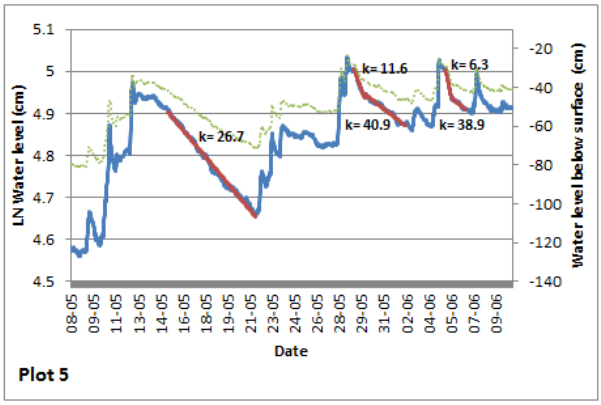

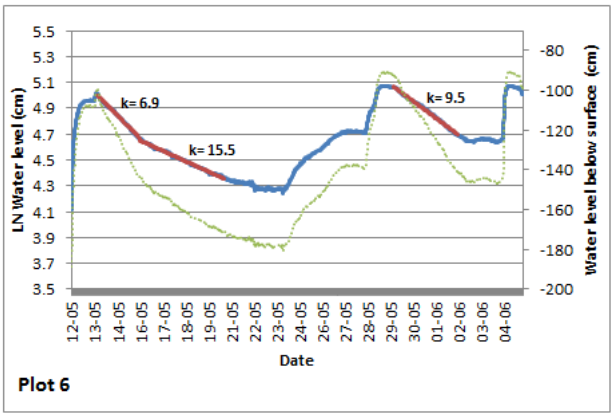

Fig. 4.27: The groundwater levels plotted on natural logarithm scale over time (blue line, primary y-axis) are used to indicate the steeper and milder segments of the linear drawdown (red lines). The depletion factors (k) for the different segments are given in days. The green dashed line shows the absolute groundwater level below surface levels (secondary y-axis).

4.5 Hydrological conceptualisation

The analysis of the different monitoring data revealed useful insights in the hydrological processes of each plot, but to relate this to the different zones of the landslide it is desired to compare the results of the different plots. Below the plots will be compared based the results of the measurements and their locations on the different zones of the landslide, see Fig. 4.28.

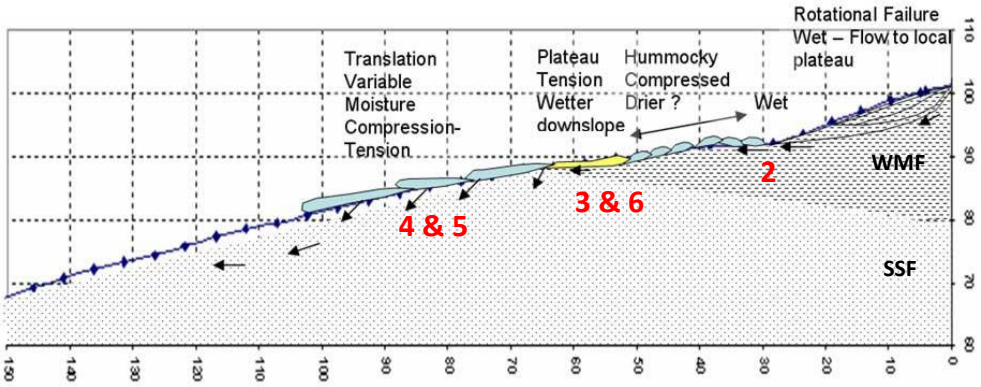

Fig. 4.28: Conceptual model of Hollin Hill with the dryer and wetter zones and locations of plots in red (BGS, 2014).

Summarizing the infiltration experiments at the plots and the one month groundwater level measurements it can be concluded that the infiltration and draining processes at Plot 3 and 5 are most likely influenced by fissures. The one month time series show these influences especially after longer wetter periods, when groundwater comes close to the bottom of the fissures (approximately 40 cm below surface level). Plot 3 is located higher on the landslide, at the top of the translational landslide where tension fissures develop and Plot 6 lower on the landslide at the prograding lobes, where both tension and compression fissures play a role.

Plot 2 is located on the first wet plateau from top to bottom on the landslide, just below the rotational zone (see Fig. 4.28). At the plot no fissures were visible and also the one month time groundwater level measurements do not indicate preferential flow. However, the sprinkling experiments at Plot 2 caused the largest increase in groundwater level of all plots and the groundwater also responded earlier than moisture contents at more shallow depths. This could be caused by the larger porosity in the soil matrix of the plot (see also Table 4.7). Another cause could

be that the area wherein Plot 2 is located is slightly tilted backward, which causes a smaller gradient for groundwater to flow downslope and therefore accumulation is larger and faster.

Table 4.7: Overview of main hydrological aspects of the different plots with h_0= groundwater level below surface before experiment in cm, h_t groundwater level end experiment, Δ S= change in storage, P= sprinkled water, n= porosity, k= depletion factor.

Plot	h_0 [cm]	h_t [cm]	Δh [h_t–h_0]	ΔS/P (%)	n [-]	k_{min} - k_{max} [days]
2	-113	-57	56	102	0.55	19 -39.8
3	-120	-90	30	92	0.5	1.3 – 9.3
4	-189	-189	0	31.2	0.53	10.6
5	-43	-38	5	2.9	0.53	6.3 – 40.9
6	-108	-104	4	80	0.53	5.5 – 16.9

The results from Plot 4 and 6 do not show any clear influences of fissures on hydrological behaviour at the plots. This most likely caused by the fact that the groundwater level is located too deep from the fissures. However, Plot 4 shows strange errors in the water balance, just as at Plot 5. Both plots are located in the upper part of the translational lobes of the landslide and in both plots fissures were observed. Plot 5 is located on the eastern lobe and Plot 4 a bit more downslope at the western lobe. In both plots was only respectively 31.2% and 2.9% of the applied water found back in change in storage. Moreover, the groundwater level at Plot 4 was located at 189 cm depth and at Plot 5 at approximately 40 cm depth, which is remarkable since both plots are located on roughly the same location on the slope. The errors in the water balance can possibly described to the presence of perched water tables in the sandy layers (also visible in ERT measurements and borehole description in Appendix II) that drain the water before it reaches the deeper groundwater and presumably also form the slip planes of the translation lobes. Both plots are also located on relatively steep slopes that could cause faster subsurface flows or preferential flows, which is also revealed by the observation of exfiltration, downslope of Plot 5 during the experiment. The perched water tables and subsurface flow are therefore probably also the cause of the translational movements of mudflows and lobes.

A general observation from all plots is the highly permeable topsoil of 0.1 to 0.2 m that most likely prevented the occurrence of overland flow during all experiments. Even with a sprinkling intensity of approximately 50 mm/hour at Plot 4 overland flow did not occur. This is most likely the result of the permeable organic rich topsoil, which functions as a buffer from where later on drainage to the underlying clay takes place. This can also be observed in the moisture content readings that show decreasing moisture contents at shallow depths (0.05 – 0.20 m depth) and continuing increasing moisture content at the deeper measurements locations.

4.6 Discussion and conclusion

The conducted infiltration experiments at the Hollin Hill landslide showed that a relatively simple experiment setup with a water bowser, water hose and garden sprinkler (including flow meter and pressure regulator) seem to be an efficient method to conduct medium scale infiltration experiment. The Gardena sprinkler was relatively easy to adjust in intensity and sprinkling area, but was quite sensible for wind disturbances that affected spatial distributed rainfall, which was visible at the ERT measurements. The Decagon GS3 for soil moisture content measurements and the Sollinst Levelogger for groundwater level measurement were very useful to investigate the infiltration and percolation processes during the experiments. Moreover, the response times of moisture contents and groundwater level during the infiltration experiment was useful to give possible indications of preferential flow mechanisms, but the derived decay constant from the one month groundwater measurement were due to quantification more reliable. The used water balance is quite simplified because the point measurement of moisture content and water level were assumed to yield for the entire plot area. Groundwater inflow and outflow were neglected, but could have been taken into account by conducting also measurement upslope and downslope of the plot. The results of the ERT were less useful than desired. It was expected that the ERT acquisitions would reveal the presence of preferential flow paths, but this was not the case. Most likely the resolution of the ERT measurements was too coarse to monitor the effects of the fissures with apertures of approximately 10 cm and depths of 40 cm. Installing the electrodes closer to each other could maybe fix this problem, but this would have resulted in less deep measurements (Zhou et al., 2000). Nevertheless, ERT did found to be useful to trace groundwater flows during larger scale infiltration experiments (Westhoff, 2011) and research in hydrological processes (Chambers et al., 2011).

The groundwater measurement confirmed the theories about the effects of fissures on both faster infiltration and more rapid drainage (Van Asch et al., 1999; Krzeminska, 2012). The measurements of Plot 3 especially showed that fissures mostly affected groundwater behaviour when the groundwater level was already close to the bottom of the fissures, thus after longer wetter periods. The highly permeable topsoil at the Hollin Hill landslide is also found in other studies that highlighted the possibilities of shallow subsurface flow in landslides and called it an organic layer interflow (Weiler & McDonnell, 2004; Schneider et al., 2014). This is possibly the process that occurred during the experiments at Plot 4 and 5 and longer term causes the movement of the lobes. When looking at the Hollin Hill specifically, Gun et al. (2013) describes the presence of sag ponds near Plot 2 and assumes: 'It is suspected that surface waters would collect in these zones, infiltrate and raise the moisture levels of failed materials, allowing the translation downslope' (p. 2029). The infiltration experiments in this study moreover revealed the largest groundwater level increases in this zone, presumably due to small gradients in groundwater level. Thus in addition to the collection of surface runoff on this location, little groundwater flow causes an extra increase in wetting of this area and thus higher change of instability. The observation from the infiltration experiments at Plot 4 and 5 on the lobes also indicated the perched water tables and subsurface flows, which probably cause the prograding lobes, which move as cascade mudflows over the hill and are also mentioned by Gunn, et al., 2013. Moreover, Van Asch et al. (1999) concluded that these perched groundwater tables can temporary store rainwater, from where it is supplied to the fissures that are connected to the slip surface.

5. Modelling the Hollin Hill landslide

5.1 Introduction

In slow moving landslides, such as the Hollin Hill landslide, fissures develop due to compression and extension of the earth mass. These fissures form preferential flow paths that influence the infiltration into the landslide and which subsequently affect the hydrology and thus slope stability of the hill (see Chapter 2.1). The aim of this chapter is to study the importance and relations of fissure flow on the hydrological behaviour and slope stability of the Hollin Hill landslide with the STARWARS model (see Chapter 2.3). The chapter starts with a general model description of STARWARS and is followed by the incorporation of the Hollin Hill landslide into the model, with information gained from the literature study and fieldwork. Subsequently, the calibration methodology and model results are described. Lastly, the model results are discussed and conclusions are drawn from the different results.

5.2 The STARWARS model

5.2.1 General model description

The conceptual model STARWARS is a distributed model, which couples hydrology and stability dynamics (Van Beek, 2002). For this research the adapted STARWARS model with detailed inclusion of hydrological and mechanical feedback mechanisms of fissures is used (Krzeminska et al, 2011). A conceptualization of the STARWARS model is shown in Fig. 5.1, with in the middle the core model that resolves the dynamic equations of saturated and unsaturated flow and around the modules that escribe the hydrological processes as interception, transpiration, snow cover or snow melt.

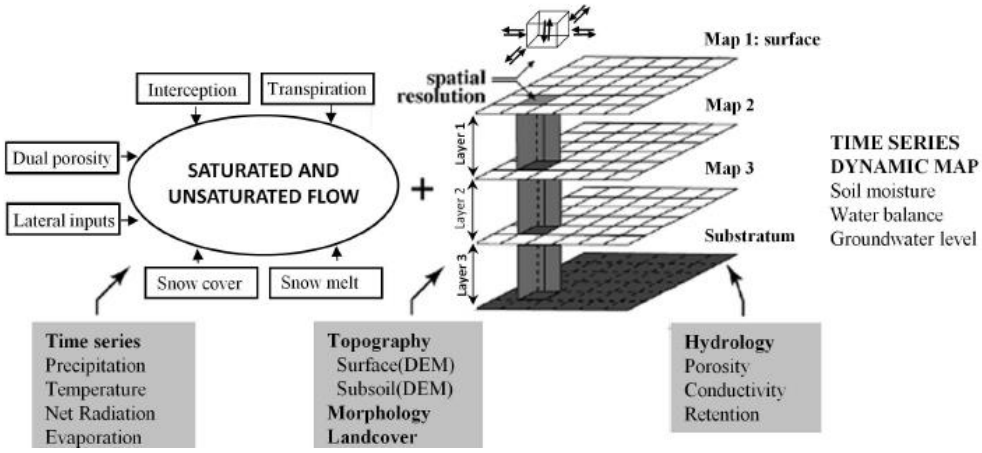

Fig. 5.1: Schematic overview of the core model and sub-models of the STARWARS model and schematic overview of the model representation (Krzeminska, 2012, based on Van Beek, 2002).

The model accommodates a landslide consisting of three layers overlying a semi-impervious bedrock. The boundary condition at the top of the first layer is determined by precipitation and evaporation. At the bottom of the third layer the boundary condition is determined by percolation, as base loss, into the underlying bedrock reservoir. All other boundaries of the model domain can be specified as in-, out-, or no flow-boundaries.

Fissure representation

The concept of fissure flow in the original STARWARS model is based on a dual-permeability approach (Jarvis, 2007) consisting of two overlapping and interacting domains: the fissures and the matrix blocks, see Fig. 5.2b. Both blocks are both present with their own characteristics and properties (porosity, hydraulic conductivity).

The model adapted by Krzeminska (2012) assumes that fissures are distinct from the matrix and are represented within each cell as a continuous network of highly pervious zones surrounded by matrix blocks, see Fig. 5.2b. The fissures are represented as near-vertical voids that are prescribed as the fraction of the area occupied by fissures (F_{fis} [m^2m^{-2}]) and the mean aperture (a_{fis} [m]). The fissures are evenly distributed throughout the cells, extend vertically over a full layer (Fig. 5.2c), but can terminate after the first or second layer. The fissure fraction and its aperture can be set per cell and per layer.

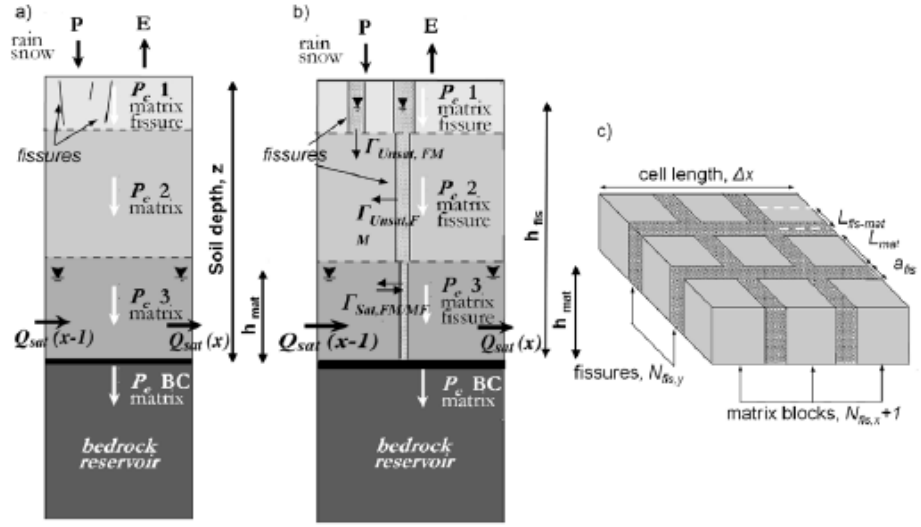

Fig. 5.2: (a) Schematisation of the original model (Malet et al., 2005; Van Beek, 2002), (b) hydrological model implemented by Krzeminska (2012), (c) fissure representation of a single layer of the soil column.

The model considers that the fissures are partly refilled with material and therefore have own soil properties and retain own water level and soil moisture content. The number of fissures is calculated per column is calculated according to the cell length, fissure density and fissure aperture:

$$N_{fis,x} = N_{fis,y} = (1 - \sqrt{1 - F_{fis}}) \cdot \frac{\Delta x}{a_{fis}} \quad (5.1)$$

Where:

$N_{fis,x/y}$ = Numbers of fissures is equal in x and y direction [-]

F_{fis} = Fraction of the surface area covered by fissures [m^2m^{-2}]

Δx = Cell length [m]

a_{fis} = Aperture of fissures [m]

The fractional area and aperture of fissures can be spatial distributed and set for all three layers. In a cell all fissures are contained by matrix, which means that the distance between the fissures equals the width of the matrix block L_{mat} [m]:

$$L_{mat} = \left(\sqrt{1 - F_{fis}}\right) \cdot \frac{\Delta x}{N_{fis,x}+1} \quad (5.2)$$

Subsequently the distance from the centre of a fissure to the centre of each matrix block can be calculated to define the different gradients by equation 5.3:

$$L_{mat-fis} = \frac{1}{2}\left(L_{mat} + a_{fis}\right) \quad (5.3)$$

5.2.2 Calculations of the model

During a model run the calculation of particular processes within each soil column take place in the following order:

1) Reading of the initial conditions of water levels and soil moisture content in matrix and fissures;
2) Evaluating of upper and lower boundary condition, which consists of precipitation (input) and evapotranspiration (calculated according to the Penman-Monteith equation (Monteith, 1981)), and base loss;
3) Calculation of vertical fluxes (see paragraph Vertical fluxes) and updating the storages;
4) Evaluating lateral fluxes (see next paragraph al Fluxes) and updating storages which also set new initial condition for the next step;
5) Calculation of factor of safety (see paragraph Factor of safety).

Vertical fluxes

In the unsaturated zone of both matrix and fissures water flows through percolation which is gravitational and vertical only. The unsaturated flow is controlled by the unsaturated hydraulic conductivity in matrix and fissure domain respectively. The unsaturated hydraulic conductivity (k_r [-]) for both domains is calculated according to the Millington & Quirk (1959) equation:

$$k_r(\theta_E) = \theta_E^{\tau} \frac{[\exp(2\cdot\alpha\cdot\theta_E) - 2\cdot\alpha\cdot\theta_E - 1]}{[\exp(2\cdot\alpha) - 2\cdot\alpha - 1]} \quad (5.4)$$

Where:

θ_E = Effective degree of saturation [-]
α = shape factor [-]
τ = Tortuosity parameter set to 4/3 [-]

For both matrix (mat) and fissure (fis) domain respectively the relationship between soil matrix tension and the effective degree of saturation (θ_E) is defined by the soil water retention curve (Farrel & Larson, 1972):

$$\theta_{E,mat/fis} = 1 - 1 - \frac{1}{\alpha_{mat/fis}} \ln\left(\frac{|h_{mat/fis}|}{h_{A,mat/fis}}\right) \quad (5.5)$$

Where:

$|h|$ = Absolute matrix suction [m]
$\alpha_{mat/fis}$ = Shape factor for matrix and fissures [m]
h_A = Air entry value for matrix and fissures [m]

The relation in equation 5.5 is used "to determine the relative degree of saturation upon the first-time drainage of a fully saturated layer and to determine the storage at which the potential evaporation is reduced. When the percolation flux in the lowest layer exceeds the basal loss, a groundwater table is formed and it rises upward with the assumption that it is vertically contiguous (for both, matrix and fissures fraction)" (Krzeminska, 2012, p. 97).

The total storage capacity of a cell is the combination of the capacity of the fissure fraction and the capacity of the matrix. The infiltration of the fissure fraction is not limited as the matrix fraction. This means that all water that cannot infiltrate into the matrix is passed on to the fissures. When the water storage in the fissures exceeds their capacity after calculation of all the fluxes (percolation and lateral exchange), it is returned to the surface as overland flow.

Lateral fluxes

Within the cells also lateral exchange (Γ [L^3T^{-1}]) is possible, but only between the saturated zones of matrix and fissure fractions ($\Gamma_{sat\ FM/MF}$) and saturated zone of the fissure fraction and unsaturated zone of the matrix when the groundwater level in the fissure fraction is higher than the water level in matrix fraction ($\Gamma_{unsat\ Fm}$). Between the unsaturated zones of the fissure network and matrix is no lateral flow possible (see also Fig. 5.2b).

Between the cells lateral flow (Q_{sat}) occurs across the saturated zone as result of difference in total piezometeric heads between the adjacent nodes in the x- and y-direction (based on the Darcy's law, see equation 5.6). The lateral flow across the cell boundaries is the specific discharge that depends on the transmissivity, which is the product of saturated permeability (matrix or fissure), water height (in matrix or fissure) and width (matrix width of fissure width in cell):

$$Q_{sat} = -K_{sat} \frac{\Delta h}{\Delta x} A \tag{5.6}$$

Where:

Q_{sat} =	Saturated flow [$m^3 day^{-1}$]
K_{sat} =	Saturated hydraulic conductivity of the soil [$m\ day^{-1}$]
Δh =	Absolut head difference between two cells, dependent on ground water level in the cell and also height of the cell in DEM [m]
Δx =	Cell length [m]
A =	Cross-sectional area, groundwater level times the cell width [m^2], through which the water is flowing.

The model contains a fissure connectivity that represents the chance for fissures to be connected laterally between the adjacent soil columns. This means that the transmissivity is modified to that of the fissure network instead of the less permeable matrix. As such, there is no particular fissure to fissure flow in adjacent cells, but a total saturated lateral flow that is distributed over both matrix and fissure domains, based on the modified transmissivity.

Factor of safety

For each time step the infinite slope model is computes the factor of safety. This factor of safety is the ratio between the maximum shearing resistance to failure and the amount that is mobilized to withstand the shear stress. It assumes therefore limiting equilibrium and the slope is stable (f_s >1) or unstable (f_s <= 1). The infinite slope model is used to calculate the slope stability (Skempton, 1964):

$$f_s = \frac{c+(\sigma-u)\tan\varphi}{\frac{W_{fis}+W_{mat}}{\Delta x^2}\sin\beta\cos\beta} \quad (5.7)$$

Where:

f_s =	Factor of safety [-]
c =	Cohesion of the soil [kPa]
φ =	Angle of internal friction [-]
$W_{fis/mat}$ =	Weight of the fissure and matrix [M]
Δx^2 =	Surface area [m^2]
β =	Slope angle [-]

Wherein the total normal stress (σ [kNm^{-2}]) is given by:

$$\sigma = \frac{(W_{fis}+W_{mat})}{\Delta x^2}\cdot\cos^2\beta \quad (5.8)$$

And the pore pressure (u [kNm^{-2}]) by:

$$u = F_{fis}\cdot h_{fis}\cdot\gamma_w\cos^2\beta + (1-F_{fis)}\cdot h_{mat}\cdot\gamma_w\cos^2\beta \quad (5.9)$$

Where:

F_{fis} =	Fraction of the surface area covered by fissures [m^2m^{-2}]
$h_{fis/mat}$ =	Groundwater height above shear surface within fissures and matrix fraction
γ_w =	Density of water [kN m^{-3}]

For a more comprehensive description of the model is referred to Van Beek (2002) and on the adaptation of fissure flow to Krzeminska (2012).

5.2.3 Dynamic feedback mechanisms

As described in Chapter 2.1 dynamic processes as the hydrological and mechanical feedback mechanisms take place in precipitation-induced landslides. Krzeminska (2012) included these dynamic processes by adapting the STARWARS model.

Hydrological feedback

In order to elaborate the dynamic nature of fissure connectivity a hydrological feedback mechanism was adopted by Kzreminska (2012), in which the fissure connectivity is made dependent on the changing degree of saturation. This means that when the soil becomes more saturated the water exchange (lateral flow) between the fissures in the soil columns also increases, and vice versa. The used relationship is shown in equation 5.11:

$$C_{fis,i} = \begin{cases} C_{fis,min} + \frac{\overline{\theta_{E,i}}-\overline{\theta_{E,fc}}}{\theta_{E,Sat}-\overline{\theta_{E,fc}}}\cdot\left(C_{fis,max}-C_{fis,min}\right) & for\ \theta_{E,i} \geq \theta_{E,fc} \\ C_{fis,min} & for\ \theta_{E,i} < \theta_{E,fc} \end{cases} \quad (5.10)$$

Where:

$C_{fis,I}$ =	Fissure connectivity at time step I [-]
$C_{fis,min/max}$ =	Minimal and maximal fissure connectivity [-]
$\overline{\theta_{E,i}}$ =	Effective saturation of the soil column at time step I [-]
$\overline{\theta_{E,fc}}$ = $\overline{\theta_{E,pF=2.0}}$=	Effective saturation at field capacity [-]

$\theta_{E,sat} = 1$ = Degree of full saturation is 1 [-]

The average effective saturation of the soil column over three layers can be calculated according to the following equation:

$$\overline{\theta_{E,i}} = \frac{\sum L_{dis,i}\left(\left(D_i - H_{mat,i}\right) \cdot \theta_{E,i} + H_{mat,i}\right)}{\sum D_i \cdot L_{mat,i}} \quad (5.11)$$

Where:

$L_{mat,i}$ = Width of matrix block between fissures of each layer [m]

D_i = Depth of each layer [m]

$H_{mat,i}$ = Groundwater level in each layer [m]

And the average effective saturation at field capacity is defined by equation 5.12:

$$\overline{\theta_{E,fc}} = \frac{\sum D_i \cdot L_{mat,i} \cdot \theta_{E,Fc}}{\sum D_i \cdot L_{mat,i}} \quad (5.12)$$

Mechanical feedback

Beside the hydrological feedback, the mechanical feedback mechanism of Krzeminska (2012) is adapted and included in the model. The mechanical feedback is the relation between stability of the slope and fissure fractions. When a slope becomes unstable and starts to move, differential displacements occur and influence fissure fractions (see Chapter 2.1). For the mechanical feedback is assumed that an unstable cell ($f_s < 1$) represents movement of the slope. Thus the dynamic fissure fraction is related to the change in safety factor of every cell. When the safety factor is for the current time step (i) and previous time step (p) below 1 and it decreases ($f_{s,i}$ compared to $f_{s,p}$), it can be assumed that differential displacements occur and fissure fractions become larger, and vice versa. When the safety factor is for the previous or the current time step above 1, fissure fractions will not change, see equation 5.13:

$$C_{fis,i} = \begin{cases} F_{fis,i} = \frac{f_{s,i}}{f_{s,p}} \cdot F_{fis,i} & for\ f_{s,i} < 1\ and\ f_{s,p} < 1 \\ F_{fis,i} \end{cases} \quad (5.13)$$

Where:

$F_{fis,i}$= Fraction of the surface area covered by fissures at time step i [m^2m^{-2}]

$f_{s,i/p}$ = Factor of safety at current (i) and previous (p) time step [-]

5.3 Hollin Hill model set-up

5.3.1 Landslide representation

In STARWARS a model representation is set up for the area comprising the Hollin Hill landslide. The size of the model is 29 rows by 29 columns with a cell size of 10 by 10 m, resulting in a 290 by 290 m large slope. The digital elevation model (DEM) extents from 106 m.a.s.l. at the north-western top, to 41 m.a.s.l. at the southeast bottom of the landslide (see Fig. 5.3L). This corresponds to a planar diagonal slope over the grid with an average angle of approximately 22.4°.

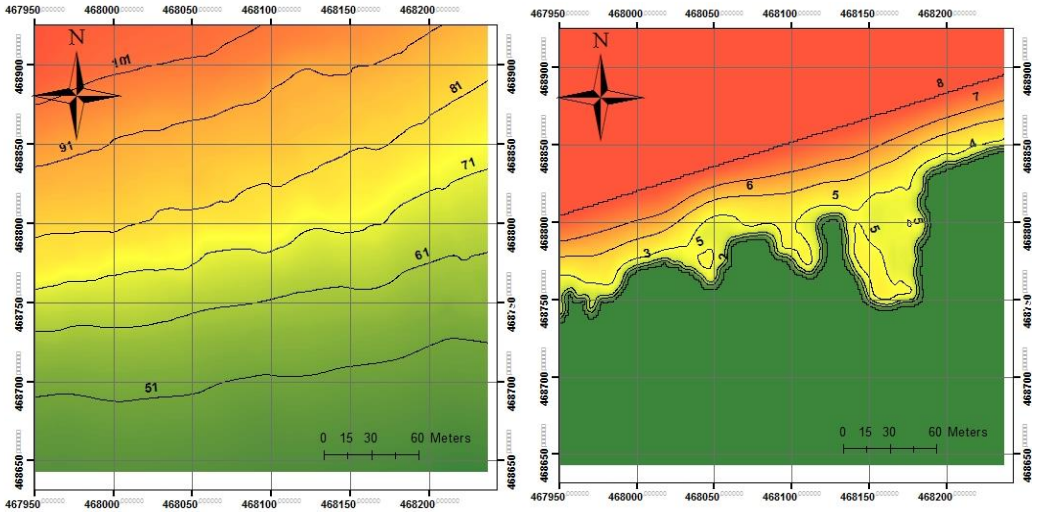

Fig. 5.3: (L) DEM in m.a.s.l. and; (R) soil depth (m).

Fig. 5.2(R) shows the soil depth of the landslide is received from the BGS and derived from the approximated daylighting boundary between WMF and SSF, and the assumption that this boundary dips about 5 degrees into the slope (see Chapter 3.6). In the model the soil depth is distinguished among three layers: a silty clay topsoil, the clayey Whitby Mudstone Formation and the silty sandy clay Staithes Sandstone Formation (see Appendix II). Since the model was built up of three layers at every location, the Whitby Mudstone becomes very small in the south of the landslide (0.2 m) where in reality the Staithes Sandstone Formation is located rightly underneath the topsoil. Only the Whitby Mudstone Formation varies by depth over the landslide, the topsoil and Staithes Sandstone Formation remain the same soil depth of 0.2 m and 2 m respectively.

Every layer has its own soil properties as hydraulic conductivity, porosity, air-entry value and alpha for both matrix and fissures (see Table 5.1). The values of the specifications are attained by a combination of both field measurements (moisture content measurements) and the Rosetta program (Schaap et al., 2001), which reveals the different values as a result of giving in the soil types. As a last step the different values are calibrated and validated (Chapter 5.2.4).

Table 5.1: Model input for the three geological layers of the Hollin Hill landslide in STARWARS.

Soil Property	Description	Layer 1: Silty clay topsoil		Layer 2: Clayey WMF		Layer 3: Silty clayey sand SSF	
		Matrix	*Fissures*	*Matrix*	*Fissures*	*Matrix*	*Fissures*
K_{sat}	Hydraulic conductivity [md^{-1}]	0.01	0.012	0.013	0.015	0.11	0.13
θ_{sat}	Saturated moisture content [-]	0.51	0.53	0.48	0.5	0.38	0.45
θ_{res}	Residual moisture content [-]	0.05	0.07	0.1	0.12	0.06	0.08
h_A	Air entry value [m]	0.016	0.016	0.015	0.15	0.033	0.033
α	Alpha [-]	14	14	13	13	12	12

5.3.2 Fissure representation and boundary conditions

During the fieldwork in May 2014 fissures were mapped by visual observations in combination with a detailed aerial photo and tape-measure to measure fissure sizes. The different areas with fissures such as backscarp, lobes, etc. (see Chapter 3.4) were drawn on a map and subsequently the average fracture of fissures (F_{fis}) and average aperture of fissures (a_{fis}) per 10 by 10 m area was calculated in every fissure area.

In the field two main areas of fissures were visible, one at the backscarp of the landslide and another one at the translational zone of the landslide (see Fig. 5.4). The latter one is divided into fissures caused by tearing of the land (just above the lobes), and fissures caused by pushing of the land (at the end of the lobes on the lower part of the landslide). The largest fissure fractions were found at the backscarp and translational zone of the eastern lobe, with both a fraction of approximately 0.15. During the fieldwork the maximum fissure depths were measured at approximately 40 to 60 cm. It was also observed that some fissures terminate earlier and also become narrower. Therefore the fraction of the fissure map was set for the first, second and third layer to 1, 0.7 and 0.01 respectively. The aperture of the fissures for the first, second and third layer was set to 0.2, 0.1, and 0.01 m respectively. A complete neglect of fissures in the third layer caused errors in the model outcomes.

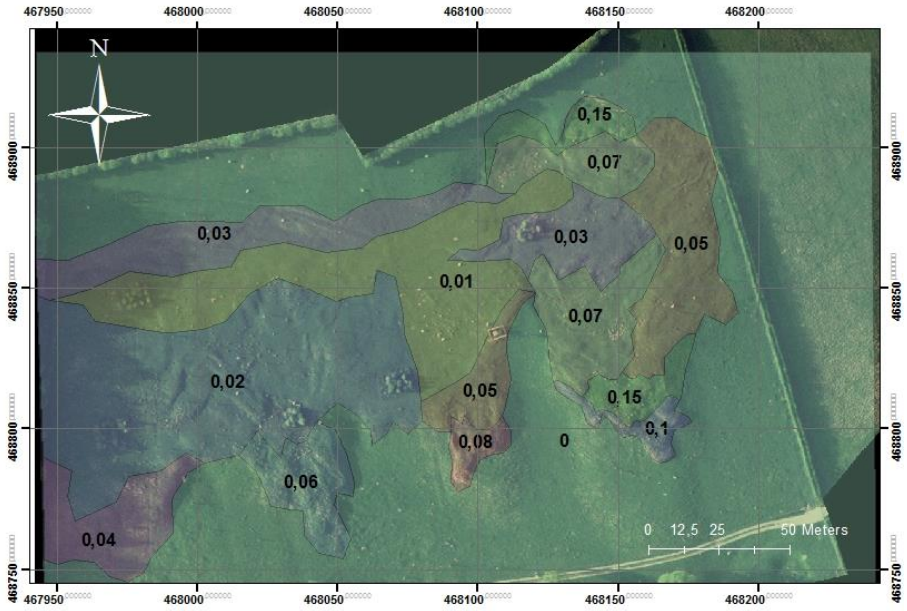

Fig. 5.4: Fissure map of Hollin Hill with fissure fraction of matrix per cell of 10 m by 10 m.

Inflow or outflow rates at the boundaries of the landslide are difficult to measure or determine. Therefore is assumed that the inflow rates are equal to the outflow rates in the model. Thus, the boundaries at the north, east, south and west were all set to no-flow boundaries. The boundary condition for the topsoil was determined by the income of precipitation and outflow of evaporation (both provided by the meteorological data input). Moreover, the topsoil consists of a fully covered short grassland with a leaf-area index of 2.53 (Ramirez-Garcia et al., 2012). The bottom of the third layer is located on a non-permeable bedrock thus constitutes a no flow boundary condition.

5.3.3 Meteorological input

For the meteorological input of the Hollin Hill model three weather stations are used. Since only a short recent period of meteorological data is available that is measured at the Hollin Landslide itself, two other MIDAS weather stations are used (see Table 5.2). The first weather station is at Dishforth Airfield in North Yorkshire, 30 kilometres from Hollin Hill, which is used for temperature data. The other weather station, East Ness in North Yorkshire, is located approximately 10 kilometres from Hollin Hill and is used for precipitation data. The correlation coefficient of the average daily temperature data from Disforth Airfield compared to the average daily temperature data measured at Hollin Hill from 15 November 2011 until 1 January 2013 is R^2=0.9325. The daily precipitation data from East Ness contains shows a lower correlation coefficient of R^2=0.2411, but zero values for dry days were included in the calculation. However, the total precipitation over the time is quiet equal with 995 mm at Hollin Hill and 1033 mm at East Ness. Since the largest part of the MIDAS data is used for the spin up of the period and only a small part for the actual period analysed, it does most likely not has too much influence on the model results.

Table 5.2: Name of the weather station, location in Latitude (Lat), Longitude (Long) and elevation (El), available data as precipitation (Prec) and temperature (Temp) and used time frame.

Weather station	Location	Data	Used time
Hollin Hill	Lat: 54.111, Long: -0.960 El: 77	Prec & Temp	15-11-2011 until 31-12-2012
Dishforth Airfield	Lat: 54.134, Long: 1.414, El: 33	Temp	1-1-1993 until 15-11-2011
East Ness	Lat: 54.200, Long: -0.934, El: 43	Prec	1-1-1993 until 15-11-2011

Beside the temperature and precipitation data, evaporation data is necessary to run the model. Since evaporation measurements are not available at any of stations in the vicinity of Hollin Hill and no other data than temperature and precipitation is available, the Hargreaves Method (Hargreaves & Samani, 1985) is used to calculate the reference potential evapotranspiration. The Hargreaves Method uses only the minimum and maximum day temperatures and daily extra-terrestrial radiation to calculate the reference potential evaporation. Nevertheless, the method has produced good results, because at least 80 per cent of the reference potential evapotranspiration depends on temperature and solar radiation (Shahidian et al., 2012). Since the minimum and maximum day temperature are only available from the two MIDAS dataset the potential evaporation will be calculated for the entire time series (spin up and model run) from the Disforth Airfield data. The daily extra-terrestrial radiation is estimated from the solar constant, solar declination and time of the year by an equation given in Allen et al. (1998). The Hargreaves method is given in equation 5.14 and an overview of the meteorological input is showed in Fig. 5.5:

$$ET_o = 0.0135\, K_T (T + 17.78)(T_{max} - T_{min})^{0.5}\, (R_a 0.408) \qquad (5.14)$$

Where:

ET_o = Reference Potential Evapotranspiration [mm day^{-1}]
K_T = Empirical coefficient is 0.170 [-]
T = Average daily temperature at 2 m height [°C]
T_{max} = Maximum daily temperature [°C]
T_{min} = Minimum daily temperature [°C]
R_a = Extra-terrestrial radiation [MJ m^{-2} day^{-1}]

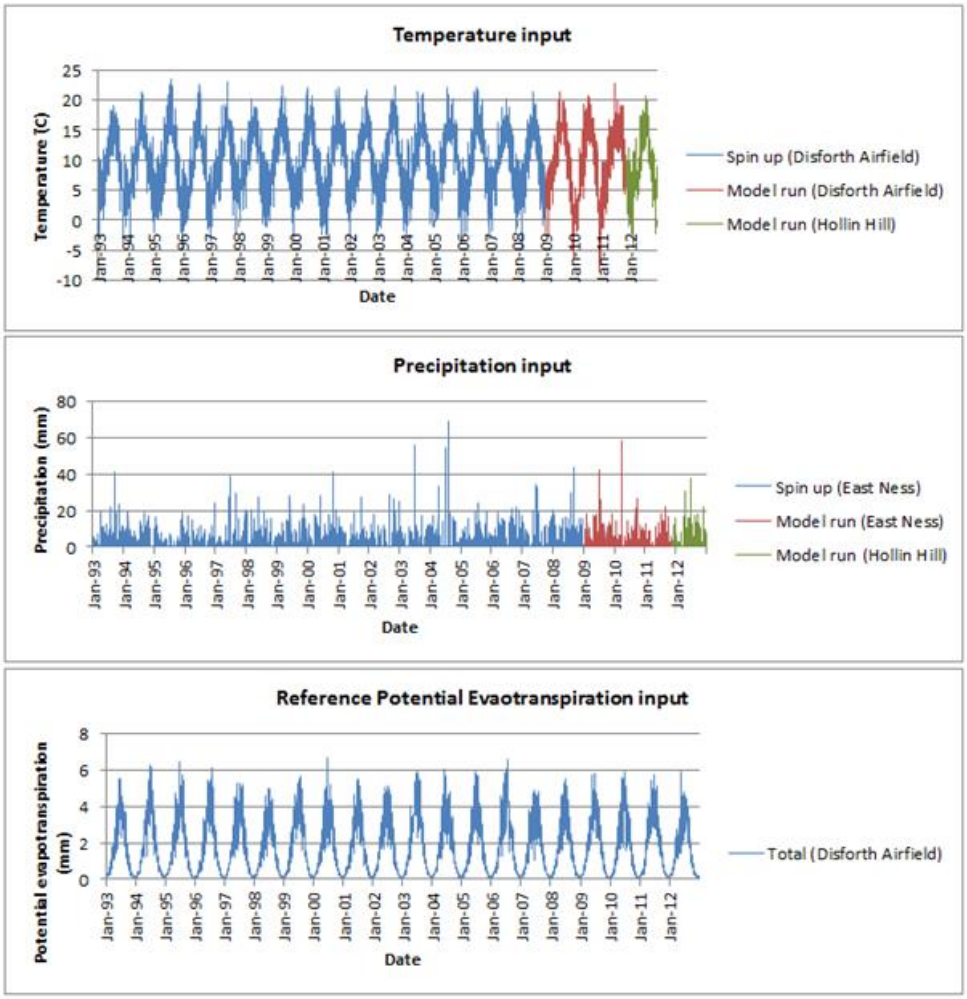

Fig. 5.5: Meteorological input for temperature, precipitation and evapotranspiration composed from three weather stations for spin up of the model and model run itself.

5.3.4 Modelling strategy and calibration

To investigate the influence of fissures on the Hollin Hill landslide and what effects the dynamic feedbacks have on the hydrology and stability of the landslide, the model is evaluated for four configurations/scenarios in STARWARS:

- No Fissures - without fissures in the landslide;
- No feedbacks - no hydrological feedback and no mechanical feedback;
- No Hydrological Feedback – only mechanical feedback is included;
- Both Feedbacks - with hydrological feedback and mechanical feedback.

For the four different scenarios the retrieved information of soil properties and meteorological input from the literature and fieldwork was used to calibrate the model. All scenarios were carried out with a spin up period in prior to the original model run to generate the initial conditions. For the spin up period the meteorological data from the two MIDAS weather stations was used from 1-1-1993 until 31-12-2008. The last conditions of this spin up period were used for the initial condition of the model run from 1-1-2009 until 31-12-2012 with daily time-steps. The Hollin Hill weather data was only available from 16-11-2011 until 31-12-2012, thus the model run starts from 1-1-2009 until 15-11-2011 with MIDAS data.

Calibration and validation

For the calibration and validation of the Hollin Hill model, groundwater level measurements were available of two locations at the Hollin Hill landslide from 24-9-2009 until 18-12-2013 (see Fig. 5.6). The measured groundwater levels in the eastern lobe show clear fluctuation, which were used to compare with the model results. The jumps in the measured groundwater levels in the western were less useful and are most likely caused by the presence of perched water tables and heterogeneous soils (see also Chapter 4.6).

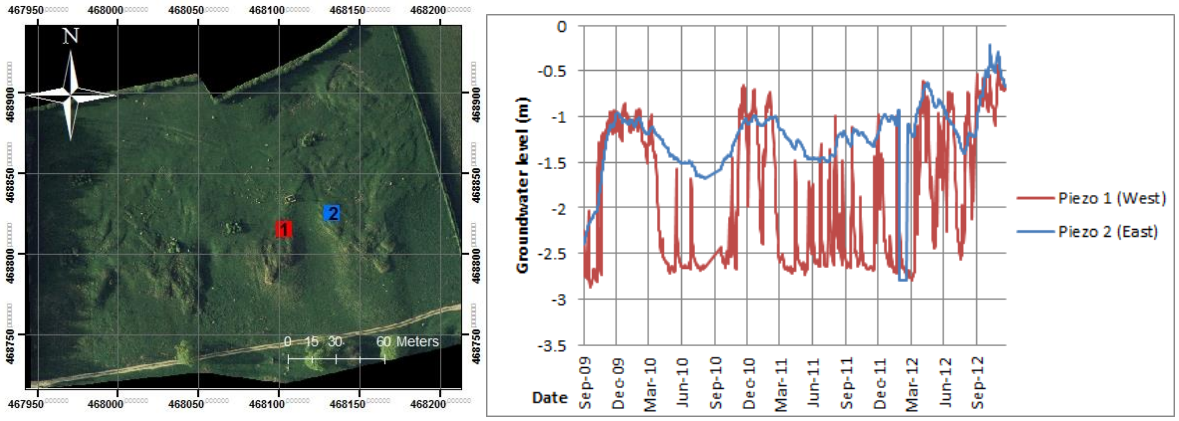

Fig. 5.6: (L) Locations of the western (2) and eastern piezometer (2) on the Hollin Hill landslide and; (R) corresponding groundwater levels.

The calibration of the model was carried out on the Both Feedbacks scenario which was found to present the natural dynamics of a fissures influenced landslide the most (Krzeminska, 2012). For the calibration the measured groundwater levels from the eastern piezometer were used from 24-9-2009 until 24-09-2010. The model was calibrated by changing the saturated hydraulic conductivity and porosity, because the hydrological model is most sensitive to their variations (Van Beek, 2002; Malet et al., 2005, Krzeminska, 2012). Also for each scenario all model outcomes (e.g., groundwater levels, moisture content, water balances, safety factors, etc.) were checked on numerical stability over the modelling period. For the stability calculations of the landslide the cohesion (c) and angle of internal friction (φ) were set for the entire landslide to 2 kPa and 0.4 respectively. This was recommended by the BGS and also gave the best results in factor of safety (F_s), which showed results to oscillate around unity at the most active areas of the Hollin Hill landslide (see Fig. 3.4 and Chapter 5.4.4).

The validation of the model was carried out against the measured groundwater levels from the eastern piezometer for the period from 24-9-2010 until 31-12-2012, because no meteorological data is available from after 31-12-2012. The validation of the produced factors of safety from the model is mainly compared with the field observations and information from literature.

5.4 Results

5.4.1 Temporal groundwater

Fig. 5.8 presents the observed groundwater levels and modelled groundwater levels from the four scenarios over the period from January 2009 until December 2012. The measured groundwater levels start in September 2009 relatively low, probably due to the time that was needed for the groundwater level in the piezometer to come in equilibrium. The general height and fluctuations of the three modelled scenarios with fissures follow the measured groundwater levels quite good. The scenario without fissures shows much lower groundwater levels and smallest fluctuations, but still coincides with the fluctuations of the measured water levels. The scenario with both feedbacks starts on approximately the same height as the measured water levels, but where the measured groundwater levels built up over time, the scenario with both feedbacks shows decreasing water levels. The scenario without hydrological feedback shows a slightly higher groundwater levels than measured, but does shows a built up of water levels towards the end of the modelling time. The scenario with no feedbacks shows not much difference from the scenario without the hydrological feedback thus one can conclude that the mechanical feedback does not have much influence. The water levels from the scenario with both feedbacks shows lower peaks and drainage times are quicker. As example, the lowest water level in April 2012 occurs with both feedback mechanisms 6 days earlier than with the other two with feedbacks. At peak period the highest water levels can also occur 1 or 2 days earlier with both feedback mechanisms. The Root Square Mean Error (RSME) (Chai & Draxler, 2014) is calculated for the scenarios with feedbacks, no hydrological feedback no feedbacks and no fissures. The RMSE values are 0.72, 0.45 and 0.46 and 2.3 m respectively.

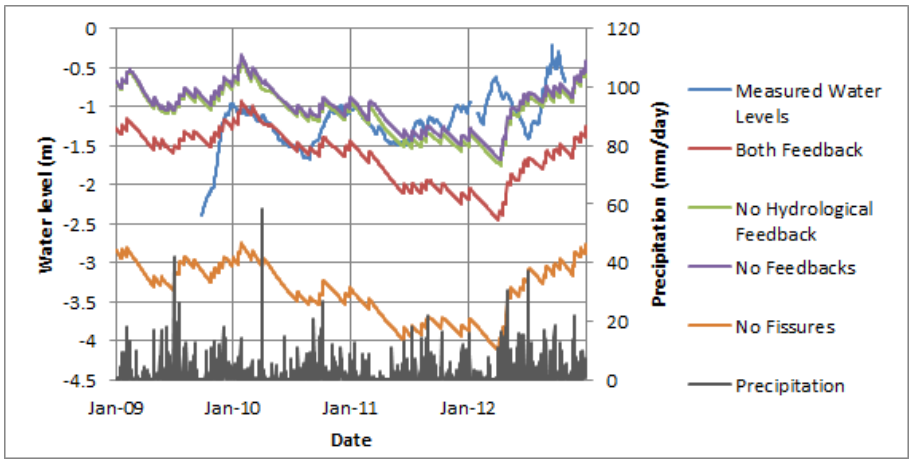

Fig. 5.7: Model outcomes for groundwater levels in matrix (a), safety factor (b) and moisture content (c) at the location of the eastern piezometers. Besides the measured groundwater levels of the eastern piezometer are shown.

5.4.2 Spatial groundwater

Fig. 5.8 shows the spatial difference of the distance between groundwater levels and surface levels in 2011 for the four scenarios. The figure shows that in the upper part of the landslide groundwater levels are lower and in the middle of the landslide the highest groundwater levels occur for all scenarios. In this area of the landslide also Plot 2 and 3 were located during the fieldwork, where at both locations high water levels were measured (see Chapter 4.4). In the middle of the eastern and western lobes, blue areas are located with lower water levels than the surrounding. At the middle of the western lobe Plot 4 was located, where lower groundwater levels were measured than at other

plots during fieldwork. Below the lobes of the landslide (in the blue zone) groundwater levels reach with every scenario fully saturation. This is because of the slope of the model that causes water to flow from the top to bottom of the model, where a no flow boundary is set. The scenario with both feedbacks shows the lowest average, minimum and maximum groundwater levels of the scenarios with fissures. The scenario without feedbacks and the scenario without hydrological feedback do not differ much from each other and also show the same minimum of groundwater levels. The figure also stresses that with the both feedbacks scenario the minimum and maximum groundwater levels show less deviation from the average groundwater levels than for the other two scenarios.

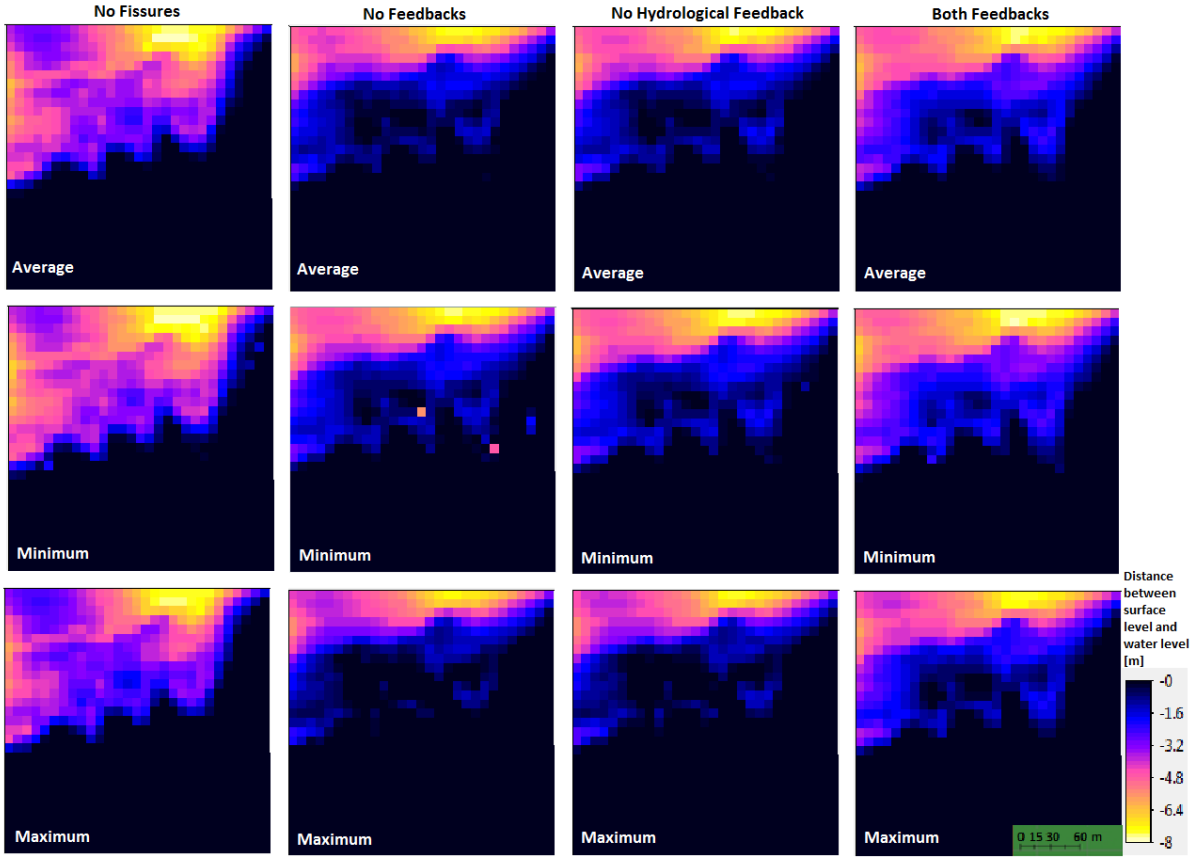

Fig. 5.8: The average, minimum and maximum distances between surface level and groundwater levels produced by the model in 2011 for the four scenarios.

5.4.3 Temporal stability

Fig. 5.9 shows the total number of unstable cells (f_s <1) per time step [day] over the model time from January 2009 until December 2012 One can see that on average the scenario without fissures shows the lowest number of unstable cells per days. However, the all-time lowest number of unstable cells per day is attained by the both feedback scenario in June 2011, due to the smaller fluctuation of the scenario without fissures and the largest fluctuations of the scenario with both feedbacks. Moreover the figure shows the incorporation of fissures causes peaks to last longer than without fissures. For the no feedbacks and no hydrological feedback scenarios the number of unstable cells is relatively the same at the start of the modelling period, but after time this changes. The number of unstable cells of the scenario without hydrological feedback becomes smaller, but with steeper fluctuations than the no feedback scenario. The third lowest numbers of unstable cells per day are visible with both feedbacks. The dynamic fissure connective causes both, increased infiltration and increased drainage, which results in larger fluctuations in the number of unstable

days. The table in Fig. 5.9 shows the average per cent of area with unstable cells from the entire landslide over the entire model period for each scenario. The scenario without fissures has logically the smallest average unstable area of 3.5%. The scenario without any feedback mechanism produces the largest area of unstable cells of 9.3%, the scenario without hydrological feedback 8.7% and the scenario with both feedbacks 5.3%.

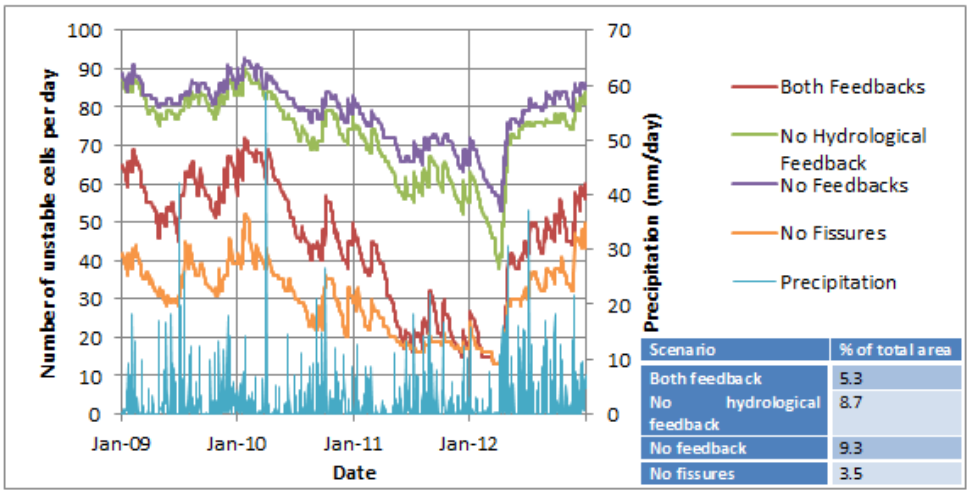

Scenario	% of total area
Both feedback	5.3
No hydrological feedback	8.7
No feedback	9.3
No fissures	3.5

Fig. 5.9: Number of unstable cells (f_s<1) per day over the entire landslide of 841 cells. The table in the right corner shows the average fraction of unstable cells over the entire modelling period.

Looking at the unstable area of the Hollin Hill landslide compared to the precipitation over time, one can obtain that during the winter and summer most precipitation occurs and instability increases after a couple of weeks to one months after the heavy precipitation. During spring and autumn less precipitation occurs and the slope also becomes more stable again. During the three years that are modelled, the year from 2011 is the driest year, which also results in a much smaller area of unstable cells. This in especial applies for the scenario with both feedbacks, which shows a quick decrease of unstable cells in 2011. However, when more precipitation occurs again around May 2012, the area of unstable cells also increases quickly again.

5.4.4 Spatial stability

In Fig. 5.10 the spatial distribution of unstable cells is shown for the average, minimum and maximum produced safety factors of 2011 for the four scenarios. The light blue areas contain unstable cells with f_s<1, the green areas are close to unstable and the red cells are stable. For all scenarios the location of the backscarp at the Hollin Hill landslide is visible with blue cells from west to east at the top. Also lower on the landslide unstable cells are visible around the lobes. The areas are also stipulated as critical areas of the landslide in Chapter 3.4. The figure shows that the scenario without feedbacks produces the largest area and the lowest minimum of safety factors. The scenario without fissures results in the smallest area of unstable cells, but the lowest minimum safety factors are lower than lowest minimum safety factors of the both feedbacks scenario. The scenario without hydrological feedback and the scenario without any feedbacks produce approximately the same area of unstable cells, but the scenario with no feedbacks shows lower minimum safety factors. Comparing the average with the minimum and maximum safety factors one can see that the differences are not much and for every scenario roughly the same, but one should also keep in mind that the average factors of safety are underestimated.

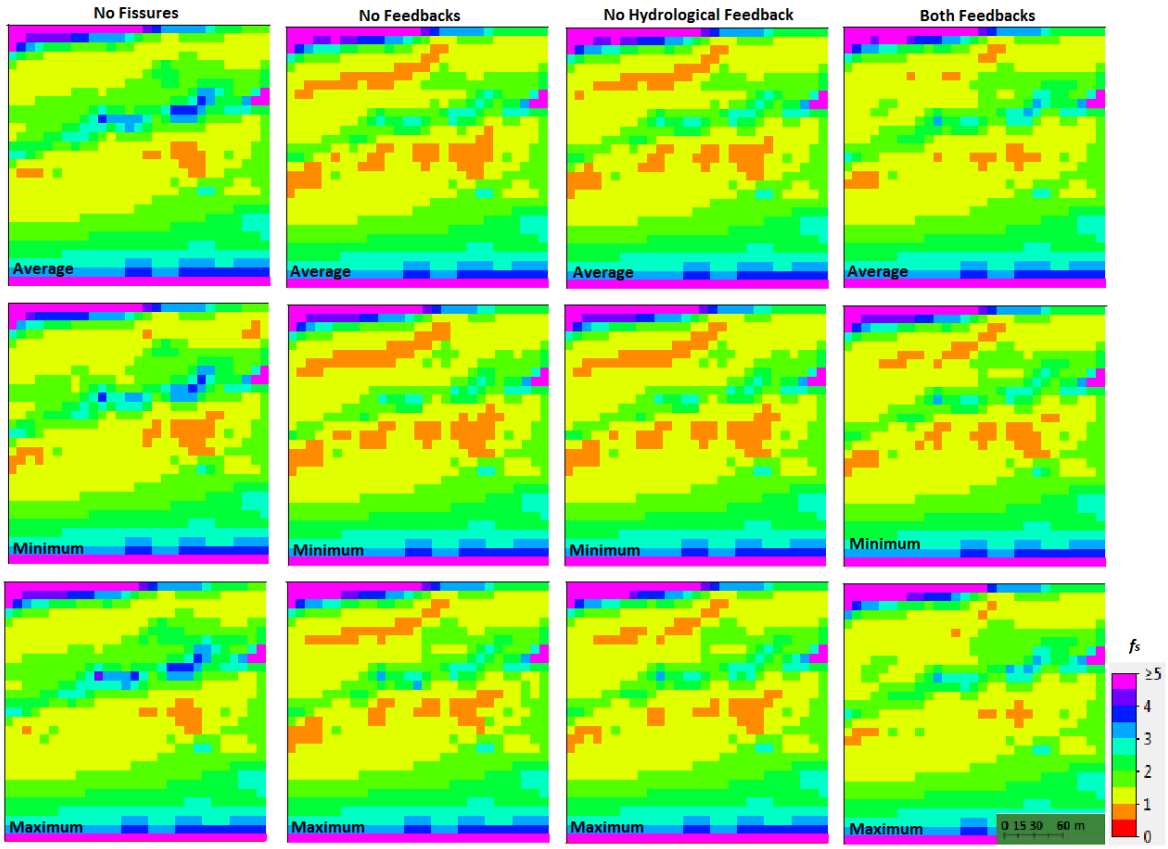

Fig. 5.10: The average, minimum and maximum factor of safety outcomes over the year 2011 for the four different scenarios, the orange/red cells show instability (f_s<1).

5.6 Discussion and conclusion

The literature study and fieldwork provided useful lithological and meteorological information to set up a conceptual model of the Hollin Hill landslide. The possibility to implement spatial distributed input in STARWARS such as the fissure map can be seen as a great advantage of the model. This was also stressed by the fieldwork, which revealed the heterogeneity of the soil, hydrology and fissures at the Hollin Hill landslides. However, in this research the hydraulic conductivity and porosity values were incorporated into the model as homogenous values, since detailed and exact spatial measurements were missing due to time and money limitations. The development of the spatial distributed fissure fraction map was relatively easy and took not more than 1 day in the field. The meteorological input for the model was collected from three different weather stations because the Hollin Hill weather station was installed only recently. Al though the temperature data and total precipitation did not deviated much from the Hollin Hill data, the correlation coefficient (R^2) for precipitation data was quite small (0.2411).

The calibration of the Hollin Hill model was quite poor since it was only based on the groundwater levels from one piezometer over a one year time period thus annual variations were not taken into account. The calibration was also just based on the Both Feedback scenarios, which causes an unfair comparison of the scenarios during the validation. Nevertheless, the model reproduced the observed groundwater level from the eastern piezometer quiet well, but response times and sizes of fluctuations of the modelled and measured groundwater levels show some deviations. The spatial outcomes of groundwater levels and stability factors coincide with the literature (Chapter 3) and fieldwork (Chapter 4). The modelled higher groundwater levels in the middle of the landslide were

also found during fieldwork at Plot 2 and the modelled lower groundwater levels in the middle of the lobes were found as well during fieldwork at Plot 4. The model shows unstable areas at the backscarp and beginning of the lobes of Hollin Hill, which are in the literature and fieldwork both indicated as unstable areas with tension cracks.

In Table 5.1 the four different scenarios are ranked on different hydrological and stability outcomes from the STARWARS model. The table shows that the scenario without fissures results in the lowest water levels that deviate the most from the measured groundwater levels (RMSE of 2.3 m). Besides, the scenario with only matrix flow shows the smallest fluctuations, the lowest number of unstable cells and also the largest minimum safety factors. The implementation of fissures in the model without feedbacks results in the highest water levels with highest number of unstable cells and the lowest minimum of safety factors, but not the smallest fluctuations in water levels. This can be explained by the extra infiltration due to fissures, which feed the matrix with water.

Table 5.3: Rankin of the model results from the four different scenarios on different outcomes

	Highest water levels	Largest fluctuations water levels	Highest number of unstable cells	Lowest minimum safety factors
No Fissures	4	4	4	4
No Feedbacks	1	3	1	1
No Hydr. Feedback	2	2	2	2
Both Feedbacks	3	1	3	3

The scenario without hydrological feedback results in water levels with a RMSE of 0.45 m and do not differ much from the water levels of the scenario with no feedbacks (RMSE = 0.46 m). From the results can be concluded that the mechanical feedback does have not much impact on the height of the water levels and only causes a small increase of fluctuation of water levels. Moreover, the difference between the no feedback and the no hydrological feedback scenario in the number of unstable cells per time step is larger than the difference in groundwater levels for the two scenarios. This can be explained by the mechanical feedback, which causes larger fissure fractions at unstable cells that become even more unstable. This subsequently leads to quicker responses in groundwater levels and even more instability again. At periods that the unstable cells become more stable, this mechanism works vice versa. The both feedback scenario yields the largest and quickest fluctuations in groundwater levels, because of implementation of the hydrological feedback. The incorporation of the hydrological feedback with dynamic fissures connectivity causes during wet periods higher transmissivity, which allows more drainage. During dry periods this works vice versa. This results in a dampening of the peaks, and quicker and lower peaks. This increase in fluctuations occurs also for the number of instable cells. The seasonality of the produced number of unstable cells shows that the largest unstable areas occur around the summer and winter in the landslide. During autumn and spring it is relatively drier and the area of unstable cells decreases quickly again. Looking over the three year one can obtain that 2011 was a relatively dry year with only a small area of unstable cells. However, after the first heavy precipitation days in 2012, the area of unstable cells increases quickly again. From the four scenarios the one without hydrological feedback results in the smallest RMSE, best corresponding fluctuations and most-fitted built up of the water level compared to the measured groundwater levels. The scenario with both feedbacks causes too much drainage, resulting in decreasing water levels, which is a result of the overestimated hydrological feedback. The static fissure connectivity without hydrological feedback might be enough for the Hollin Hill slide. The simplicity of the dynamic feedbacks is stressed by Krzeminska (2012) and Wenker (2013).

6. Synthesis and recommendations

6.1 Tracing fissures with field scale infiltration experiments

The small scale infiltration experiments at plots of approximately 20 m^2 with a garden sprinkler and different measurement devices offered great data sets. These data sets, together with the hydrograph separation method of the one month groundwater level measurements helped to gain a better understanding of local hydrological behaviour. The ERT measurements were less useful than expected, because unique flow paths were not clear on the images. Nevertheless, the ERT revealed the spatial distribution of the sprinkled water, the percolation processes and the existence of perched water tables, which possibly also affect landslide hydrology and stability (Van Asch et al., 1999; Huat et al., 1999). Also the water balances were found to be a useful application to check the reliability of the infiltration experiments.

The infiltration experiments revealed that fissures cause both quicker and increased, infiltration and drainage capacities. The one month groundwater levels also showed that fissures especially play a role when groundwater comes close to the bottom of the fissures. At Hollin Hill this was approximately 40 cm below surface level. Besides, the infiltration experiments revealed the high infiltration capacity of the organic topsoil, which most likely functions as a storage from where water can infiltrate to the deeper grounds. The plots on the different zones of the landslides revealed the heterogeneity of soil properties, hydrology and fissures at the landslide. The borehole profiles showed that beside lithology, the differential displacements play a role in this. Such as in the prograding lobes were besides fissures, also perched water tables probably affect the hydrological behaviour.

6.2 Model input STARWARS and different scenarios

The STARWARS model with dual-permeability approach of an overlapping fissure and matrix domain was used to help understanding relations and possible impacts of preferential fissure flow on landslide hydrology and stability. The literature study (Chapter 2 and 3) and fieldwork (Chapter 4) formed an good understanding to set up the conceptual model and determine parameters as porosity and fissure fraction with a spatial distributed fissure map. The possibility of spatial distributed input in the PCRaster is experienced as a great advantage. The calibration of the model was relatively poor since only one piezometer was available at the Hollin Hill landslide. Nevertheless, the model produced spatial outcomes, which coincide with the literature and fieldwork observations.

The three outcomes of unstable area per time step from the STARWARS model shows that the in the winter and summer the largest area of the landslide is unstable. The response of instability on precipitation is relatively quick with approximately one to several weeks. Looking at the four scenarios, one can obtain that the scenarios without fissures underestimated the groundwater levels and overestimated the stability of the landslide. The scenario with fissures, but no feedbacks overestimated the groundwater levels a little, but showed coinciding fluctuations with the measured groundwater levels. The scenario with only a mechanical feedback and no hydrological feedback produces the best model outcomes with the smallest RMSE of 0.45 m. The scenario with both feedbacks produced groundwater level that fitted good to the measured water levels in the beginning of the time serie, but at the end of the time serie the scenario produced much lower

water levels due to too much drainage. This is probably caused by the effect of the hydrological feedback, which overestimated the fissure connectivity and causes too much drainage.

6.3 The influence of fissures on the Hollin Hill landslide

The field scale infiltration experiments outlined the spatial heterogeneity of soil properties, hydrology and fissure influence over the landslide. Responses of groundwater levels and moisture content measurements revealed the influence of fissures by quicker increases in both, infiltration and drainage of the groundwater. These effects on groundwater behaviour are especially visible when water levels are close to the bottom of the fissures, at approximately 40 cm below surface level for Hollin Hil. Beside the influence of fissures on landslide hydrology, the fieldwork showed that existence of perched water tables might also influence landslide hydrology. The model, with the inputs gained from literature and fieldwork, gave insight in the relations between landslide hydrology and stability. The STARWARS model revealed that fissures cause higher groundwater levels to occur in the landslide and increased instability. From the four scenarios can be concluded that the incorporation of a hydrological feedback in the model overestimates the draining capacities of the fissures for the Hollin Hill landslide. Meanwhile, the scenario with mechanical feedback results in the best fitted model outcomes. However, one should keep in mind that the incorporation of the feedback mechanisms also introduces more parameters into the model and thus more uncertainties.

From the conducted fieldwork and conceptual model in this thesis can be concluded that the influence of fissures on precipitation-induced slow-moving landslides, like the Hollin Hill landslide, is of great importance to hydrological responses and landslide stability in nature and modelling. However, the fieldwork and model also showed the importance of influences of disturbing layers and perched water tables on landslide hydrology.

6.4 Recommendations

In order to improve and extend field scale infiltration experiments to trace influence of fissures on landslide hydrology, the follow recommendations are defined:

- A tent can be used as a windshield to maintain a constant spatial distributed rainfall. The tent can also be installed a few days before the experiment to avoid pre-wetting of the plot, which result in more clear measurement results;
- For future similar sprinkling experiments one should keep in mind to have enough height difference between the water bowser and sprinkler to create enough water pressure. This was the reason why Plot 1 had to be cancelled during this research;
- More investigation is necessary to define a suitable ERT setup that can identify characteristics of unique preferential flow paths;
- The identification of preferential flow paths at Hollin Hill can be improved by using chemical or dye tracer, as was done in the studies of Krzeminska 2012 and Schneider et al. (2014);
- Long term ERT measurements of applied salt water by infiltration experiments may also reveal the influence of perched water tables on landslide hydrology.

Recommendations for the Hollin Hill model in STARWARS and the general STARWARS model:

- For future research the incorporation of spatial and temporal distributed maps, based on more field measurements is recommended to improve the model results. This in specially

yields for the hydraulic conductivity and porosity, which were found to be important parameters of the STARWARS model (Malet et al., 2005; Krzeminska, 2012);

- The data from the two MIDAS weather stations deviated not much from the Hollin Hill data and was only used for short time of the model period. However, a correction of the data based on altitude and location could still improve model results;
- Regarding to heterogeneity it is recommended to conduct the calibration with more piezometers and longer time series. Besides, the modelled moisture contents can be compared with ERT images. Also the produced safety factors from the model could be compared with displacement data, such as from Dixon & Smith (2014);
- Future research studies in the monitoring of fissures characteristics and their variation over time would allow better understanding of the hydrological and mechanical feedback mechanism and might lead to improvement of the mechanisms. It may even be better to calculate the mechanical feedback with velocity of the landslide, based on Saint-Venant equation as Van Asch et al. (2007) and Wenker (2013) did;
- The mechanical feedback causes increasing and decreasing fissures and thus changes in the mass of each soil column, because fissure and matrix soil properties differ. To improve this, the effects of a mass balance of the soil needs to be checked after every simulation;
- The soil columns in PCRaster are solid and not move over time. This means that for example the soil depth map does not change over time, which is of course different in reality;
- Finally, the spatial distributed input of STARWARS allows the implementation of perched water tables in the layers of the model; this would be interesting to investigate.

References

Allen, R., Pereira, L., Raes, D., & Smith, M. (1998). *Crop evapotranspiration - Guidelines for computing crop water requirements - FAO Irrigation and drainage paper 56.* Rome: FAO.

Altman, S., Arnold, B., Bernard, R., Barr, G., Lio, C., McKenna, S., et al. (1996). *Flow Calculations for Yucca Mountain Groundwater Travel Time (GWTT-95).* Albuquerque, N. Mex.: Sandia National Laboratories.

Beven, K., & Germann, P. (1982). Macropores and water flow in soils. *Water Resources Reserach*(18), 1311-1325.

BGS. (2014). *The Hollin Hill Landnslide Observatory, Yorkshire*. Opgeroepen op July 15, 2014, van British Geological Survey: http://www.bgs.ac.uk/landslides/hollinHill.html

Bogaard, T., Buma, J., & Klawer, C. (2004). Testing the potential of geochemical techniques for identifying hydrological systems within landslides in partly weathered marls. *Geomorphology, 58*, 323-338.

Bogaard, T., Guglielmi, Y., Marc, V., Emblanch, C., Bertrand, C., & Murdy, J. (2007). Hydrogeochemistry in landslide research: a review. *Bull. Soc. Géol. Fr.*(2), 113-126.

Brabb, E. (1991). The world landslide problem. *Episodes*(14), 52-61.

Burton, A., & Bathurst, J. (1998). Physically based modelling of shallow landslide sediment yield at a catchment scale. *Environmental Geology*(35), 2-3.

Chai, T., & Draxler, R. (2014). Root mean square error (RMSE) or mean absolute error (MAE)? - Arguments against avoiding RMSE in the literature. *Geoscientific Model Development*, 1247-1250.

Chambers, J., Weller, A., Gunn, D., Kuras, O., Wilkinson, P., Meldrum, P., et al. (2008). Geophysical anatomy of the Hollin Hill landslide, North Yorkshire, UK. *Near Surface 2008*, 15-17.

Chambers, J., Wilkinson, P., Kuras, O., Ford, J., Gunn, D., Meldrum, P., et al. (2011). Three-dimensional geophysical anatonmy of an active landslide in Lias Group mudrocks, Cleveland Basin, UK. *Geomorphology*(4), 472-484.

Chen, H., & Lee, C. (2003). A dynamic model for rainfall-induced landslides on natural slopes. *Geomorphology*(51), 269-288.

Collison, A., Wade, S., Griffiths, J., & Dehn, M. (2000). Modelling the impact of predicted climate change on landslide frequency and magnitude in SE England. *Engineering Geology*, 55:205-218.

Corominas, J., Moya, J., Ledesma, A., Rius, J., Gili, J., & Lloret, A. (1999). Monitoring of the Vallcebre landnslide, Eastern Pyrenees, Spain. *Proceeding Intern. Symp. on Slope Stability Engineering: IS-Shikoku '99, 2*, 1239-1244.

Daily, W., & Ramirez, A. (1992). Electrical Resistivity Tomography of Vadose Water Movement. *Water Resources Research, 5*, 1429-1442.

Debieche, T.-H., Bogaard, T., Marc, V., Emblanch, C., Krzeminska, D., & Malet, J.-P. (2010). Hydrological and hydrochemical processes observed during a large-scale infiltration experiment at the Super-Sauze mudslide (France). *Hydrological processes, 26 (14)*, 2157-2170.

Decagon Devices. (2011). GS3 - Water Content, EC, Temperature Sensor - Operator's Manual.

Dijkstra, T., Wearmouth, M., & Dixon, N. (2011). *Models and correction algorithms for geophysics; thermal corrections and moisture content interpretations for ALERT electrical resistivity arrays at BIONICS.* Internal report for the BGS Transportation Geotechnics Group.

Dixon, N., & Smith, A. (2014). Acoustic emission monitoring of active waveguides to quantify slope stability.

Farrel, D., & Larson, W. (1972). Modelling the pore structure of porous media. *Water Resources Research, 8*, 699-706.

Greco, R. (2002). Preferential flow in macroporous swelling soil with internal catchment: model development and applications. *Journal of Hydrology, 269*, 150-168.

Gunn, D., Chambers, J., Hobbs, P., Ford, J., Wilkinson, P., Jenkins, G., et al. (2013). Rapid observations to guide the design of systems for long-term monitoring of a complex landslide in the Upper Lias clays of North Yorkshire, UK. *Quarterly Journal of Engineering Geology and Hydrogeology*.

Hargreaves, G., & Samani, Z. (1985). Reference crop evapotranspiration from temperature. *Applied Engineering in Agriculture, 1*, 96-99.

Havenith, H., Torgoev, I., Meleshko, A., Alioshin, Y., Torgoev, A., & Danneels, G. (2006). Landslides in the Mailuu-Suu Valley, Kyrgyzstan - Hazards and Impacts. *Landslides*(3), 137-147.

Hencher, S. (2010). Preferential flow paths through soil and rock and their association with landslides. *Hydrological Processes, 24*, 1610-1630.

Hendrickx, J., & Flury, M. (2001). Uniform and preferential flow mechanisms in the vadose zone. In N. R. Council, *Conceptual Models of Flow and Transport in the Fractured Vadose Zone* (pp. 149-187). Washington DC: National Academy Press.

Highland, L., & Bobrowsky, P. (2008). *The landslide handbook - A guide to understanding landslides.* Reston, Virginia, U.S.: Geological Survey Circular.

Huat, L., Ali, F., Mariappan, S., & Soon, P. (1999). Effects of perched water table on slope stability in unsaturated soils. *Slope Stability Engineering*, 393-397.

Inada, R., & Takagi, M. (2010). Method of landslide measurement by ground based LiDAR. *International Archives of the Photogrammetry, Remote Sensing and Spatial Information Science*(38).

Jarvis, N. (2007). A review of non-equilibrium water flow and solute transport in soil macropores: principles, controlling factors and consequences for water qualitiy. *Europoean Journal of Soil Science, 58*, 523-546.

Keaton, J., & De Graff, J. (1996). Surface observation and geologic mapping. In A. Turner, & R. Schluster, *Landslides Investigation and Mitigation* (p. 247). Washington, DC: National Academy Press.

Krzeminska, D. (2012). *The influence of fissures on landslide hydrology.* PhD thesis, Delft University of Technology.

Krzeminska, D., Bogaard, T., Asch, T., & Van Beek, L. (2011). A conceptual model of the hydrological influence of fissures on landslide activity. *Hydrol. Earth. Sci. Discuss.*(8), 11039-11073.

Kuriakose, S., Van Beek, L., & Van Westen, C. (2009). Parameterizing a physically based shallow landslide model in a data poor region. *Earth Surface Processes and Landforms*, 867-881.

Lane, J., Day-Lewis, F., Johnson, C., Dawson, C., Nelms, D., Eddy-Miller, C., et al. (2008). Fiber-optic distributed temperature sensing: A new tool for assessment and monitoring of hydrologic processes. *Symposium on the Application of Geophysics to Engineering and Environmental Problems.* Philadelphia, Pennsylvannia: Proceedings, Environmental and Engineering Geophysical Society.

Lepore, C., Arnone, E., Noto, L., Sivandran, G., & Bras, R. (2013). Physically based modeling of rainfall-triggered landslides: a case study in the luquillo fores, Puerto Rico. *Hydrol. Earth. Sci.*(7), 3371-3387.

Linsley, R., Kohler, M., & Paulhus, J. (1975). *Hydrology for engineers.* McGraw-Hill Incorporated.

Malet, J.-P., van Asch, T., van Beek, R., & Maquaire, O. (2005). Forecasting the behaviour of complex landslides with a spatially distributed hydrological model. *Natural Hazards and Earth System Science, 5*, 71-85.

McDonnel, J. (1990). The influence of macropores on debris flow initiation. *Quarterly Journal of Engineering Geology*(23), 325-331.

Met Office. (2014). *High Mowthorpe 1971–2000 averages*. Opgeroepen op August 2014, 06, van Met Office: http://www.metoffice.gov.uk/public/weather/climate/gcxec3t0r

Millington, R., & Quirk, J. (1959). Permeability of porous media. *Nature, 183*, 387-388.

Monteith, J. (1981). Evaporation and surface temperature. *Quartely Journal of the Royal Meteorological Society, 107*, 1-27.

Nettleton, I., Martin, S., Hencher, S., & Moore, R. (2005). Debris flow types and mechanisms. In M. Winter, F. Macgregor, & L. Shackman, *Scottish Road Network Landslide Study.*

Newmark, R., Daily, W., & Ramirez, A. (1999). *Electrical Resistance Tomography Using Steel Cased Boreholes as Electrodes.* Livermore, Ca.: Lawrence Livermore National Laboratory.

Nieber, J., & Sidle, R. (2010). How do disconnected macorpores in sloping soils facilitate preferential flow. *Hydrological Processes, 24*, 1582-1594.

Nobles, M., Wilding, L., & McInnes, K. (2004). Pathways of dye tracer movement through structurred soils on a macroscopic scale. *Soil Science, 169*, 229-242.

Noguchi, S., Tsuboyama, Y., Sidle, R., & Hosoda, I. (1999). Morphological characteristics of macropores and the distribution of preferential flow pathways in a forested slope segment. *Soil Science Society of American Journal, 169*, 1413-1423.

Oberdoerster, C., Vanderborght, J., Kemma, A., & Vereecken, H. (2009). Monitoring Preferential Flow Processes in a Forest Soil with TDR and ERT. *Geophysical Research Abstracts, 12*.

Peters, N. (1994). Hydrologic Processes.

Petley, D. (2008). The global occurence of fatal landslides in 2007. *Geophycial Research Abstract, 10*.

Pierson, T. (1983). Soil pipes and slope stability. *Quarterly Journal of Engineering Geology and Hydrogeology, 16*, 1-15.

Raia, S., Alvioli, M., Rossi, M., Baum, R., Godt, J., & Guzzetti, F. (2013). Improving predictive power of physically based rainfall-induced shallow landslide models: a probabilistic approach. *Geosci. Model Dec. Discuss.*(6), 1367-1426.

Ramirez-Garcia, J., Almendros, P., & Quemada, M. (2012). Ground cover and leaf area index relationship in a grass, legume and crucifer crop. *Plant Soil Environmen, 58*, 385-390.

Reichenbach, P., Carrara, A., & Guzzetti, F. (2002). Assessing and mapping landslide hazards and risk. *Natural Hazards and Earth System Sciences*, 1-2.

Reid, M., Baum, R., LaHusen, R., & Ellis, W. (2008). Capturing landslide dynamics and hydrologic triggers using near real-time monitoring. *Landslides and Engineered Slopes*.

Ritsma, C., & Dekker, L. (1994). How water moves in a water reppelent sandy soil: 2. Dynamics of fingered flow. *Water Resources Research*(30), 2519-2531.

Roth, K. (1995). Steady state flow in an unsaturated, two-dimensional, macroscopically homogeneous, Miller-similar medium. *Water Resources Research*(31), 2127-2140.

Roulier, S., & Schulin, R. (2008). Guest Editor's preface to special issue on preferential flow. *European Journal of Soil Science, 59*.

Schaap, M., Martinus, F., & Van Genuchten, T. (2001). ROSETTA: a computer program for estimating soil hydraulic parameters with hierachical pedotransfer functions. *Journal of Hydrology, 251*, 163-176.

Schneider, P., Pool, S., Strouhal, L., & Seibert, J. (2014). True colors - experimental identification of hydrological processes at a hillslope prone to slide. *Hydrology and Earth System Science*, 875-892.

Schulz, W., McKenna, J., Kibler, J., & Biavati, G. (2009). Relation between hydrology and velocity of continuously moving landslide - evidence of pore-pressure feedback regulating landslide motion? *Landslides*(6), 181-190.

Shahidian, S., Serralheiro, R., Serrano, J., Teixeira, J., Haie, N., & Santos, F. (2012). Hargreaves and Other Reduced-Set Methods for Calculating Evapotranspiration. In A. Irmak, *Evapotranspiration - Remote Sensing and Modeling.*

Shen, H., & Fernandez-Steeger, T. (2011). Monitoring and Modeling of Landslide in Earthquake Environment. *Moderne Bodenmechnik in der Geotechnik*, 403-416.

Sidle, R., Noguchi, S., Tsuboyama, Y., & Laursen, K. (2001). A conceptual model of preferential flow systems in forested hillslopes: evidence of self-organization. *Hydrological Processes, 15*, 1675-1692.

Sidle, R., Tsuboyama, Y., Noguchi, S., Hosada, I., Fujieda, M., & Shimizu, T. (2000). Stormflow generation in steep forested headwaters: a linked hydrogeomorphic paradigm. *Hydrological Processes, 14*, 369-385.

Šimůnek, J., Jarvis, N., Van Genuchten, M., & Gardenas, A. (2003). Review and comparison for models describing non-equilibrium and preferential flow and transport in the vadose zone. *Journal of Hydrology, 272 (1-4)*, 14-35.

Skempton, A. (1964). The long-term stability of clay slope. *Geotechnique, 14*, 95-102.

Solinst. (2013). Levelogger Series, Model 3001 Data sheet. Canada.

Tallaksen, L. (1995, September). A review of baseflow recession analysis. *Journal of Hydrology, 165*, 349-370.

Tsuboyama, Y., Sidle, R., Noguchi, S., & Hosada, L. (1994). Flow and transport through the soil matrix and macropores of hillslope segment. *Water Resources Research, 30*, 879-890.

Van Asch, T., Buma, J., & Van Beek, L. (1999). A view on some hydrological triggering systems in landslides. *Geomorphology, 30*, 25-32.

Van Asch, T., Malet, J.-P., Van Beek, L., & Amitrano, D. (2007). Techniques, advances, problems and issues in numerical modelling of landslide hazard. *Bulletin de la Société Géologique de France*(178), 65-88.

Van Bavel, M., & Nichols, C. (2002). *Theta and Profiler Soil Moisture Probes - Accurate Impedance Measurement Device - New Application. Technical Report.*

Van Beek, L. (2002). *Assessment of the influence of changes in land use and climate on landslide activity in a Mediterranean environment.* PhD Thesis. University of Utrecht, Netherlands.

Van Beek, L., & Van Asch, T. (1999). A combined conceptual model for the effects of fissures-induced infiltration on slope stability. *Process modelling and landform evolution*, 147-167.

Van Beek, L., & Van Asch, T. (2004). Regional assessment of the effects of land-use change on landslide hazard by means of physically based modelling. *Natural Hazards, 31*, 289-304.

Van Genuchten, M. (2011, September 12-16). Dual-porosity approximations of the hydraulic properties of unsaturated structured media. *Brazilian Meetiing of Soil Physics*.

Van Genuchten, M., Schaap, M., Mothanty, B., Šimůnek, J., & Leij, F. (1999, November 24-26). Modelling flow and transport processes at the local scale in space and time. Leuven, Belgium: Wageningen Pers.

Van Schaik, N., Schanbel, S., & Jetten, V. (2008). The influence of preferential flow on hillslope hydrology in a semi-arid watershed (in the SPanish Dehesas). *Hydrological Processes, 22*, 3844-3855.

Varnes, D. (1978). *Slope movement types and processes.* National Academy of Science, Transportation and Road Research Board, Washington D.C.

Vecchia, G., & Cosentini, R. (2011). Electrical resistivity tomography: monitoring of hydro-chemical processes and parameter estimation. In F. Barends, J. Breedeveld, R. Brinkgreve, M. Korff, & L. van Passen, *Geotechnical Engineering: New Horizons, Proceeding of the 21st European Young Geotechnical Engineers' Conference* (pp. 312-317\).

Weiler, M., & McDonnel, J. (2007). Conceptualizing lateral preferential flow and flow networks and simulating the effects on gauged and ungauged hillslopes. *Water Resources Research, 43*.

Weiler, M., & McDonnell, J. (2004). Virtual experiments: a new approach for improving process conceptualization in hillslope hydrology. *Journal of Hydrology*, 3-18.

Westhoff, M. (2011). High resolution temperature observations to identify different runoff processes. *PhD Thesis, Delft Universitiy of Technology*.

Wienhöfer, J., Lindenmaier, F., & Zehe, E. (2010). Challenges in Understanding the hydrologic Controls on the Mobility of Slow-Moving Landslides. *Vadoze Zone*(9), 496–511.

Wilkinson, P., Loke, M., Meldrum, P., Chambers, J., Kuras, O., Gunn, D., et al. (2012). Practical aspects of applied optimized survey design for electrical resistivity tomography. *Geophysical Journal International*, 428-440.

Zhou, W., Beck, B., & Stephenson, J. (2000). Reliability of dipole-dipole electrical resistivity tomography for defining depth to bedrock in covered karst terranes. *Environmental Geology, 39*, 760-766.

Acknowledgements

During this thesis three organizations were involved; Utrecht University, Delft University of Technology and the British Geological Survey. This gave me the opportunity to meet a lot of new inspiring people, which I see as one of the most beautiful aspects of life.

In the beginning of my thesis I was still a bit afraid that the collaboration of three different parties involved could cause some indistinctness, but time has shown that this were unnecessary worries. The ideas and goals of my supervisors; Rens van Beek, Thom Bogaard and Tom Dijkstra were on one line and I knew who I had to contact for every problem I had.

First of all, I would like to express my thanks to Rens van Beek from the Utrecht University for helping me out with the questions I had about the STARWARS model in PCRaster, which was totally new for me. Also his clear feedbacks to structure and improve my thesis were of great help.

My favourite part of the thesis research was the fieldwork at the Hollin Hill landslide. This was also triggered by Thom Bogaard his enthusiasm and stories about his worldwide fieldwork experiences. His experience and help were of great value to prepare and conduct my fieldwork at the Hollin Hill landslide. Therefore, I would like to thank him.

The thesis could not have taken place without the British Geological Survey, represented by Tom Dijkstra who gave me the opportunity to use the Hollin Hill landslide as a case study and to conduct the fieldwork. I would like to thank the team of the British Geological Survey; Tom Dijkstra, Jonathan Mackay, Jon Chambers and Seb Uhlemann for the help during the fieldwork and carrying out the Electrical Resistivity Tomograph. In especial, I would like to express my gratitude for the hospitality of Tom Dijkstra and also his family which made the trip to England to a great memory. The different memories such as the tours in the Subaru and pick-up trucks, and during fieldwork the beers and steak and ale pies will be forever in my memories.

As last, but not least I would like to thank my family, friends and girlfriend for all kind of support in motivation, relaxation and love.

Appendix I

Pictures of the five different plots.

Plot 2

Plot 3

Plot 4

Plot 5

Plot 6

Appendix II

Borehole descriptions of each plot.

Borehole plot 2

Depth from surface (cm)	Description
0-15	Soft, dark brown, organic silty CLAY (topsoil);
15-95	Soft, lightbrown silty CLAY with occasional fragments of DF (1-5 mm), iron staining becoming progressively more abundant with depth, increasingly gleyey [pocket penetrometer undrained shear strength indication <20kPa]
95 – 130	Soft, lightbrown silty CLAY with occasional fragments of DF (1-5mm), abundant iron staining, mottled grey/brown to redbrown becoming slightly friable [<20kPa]
130-160	Soft, lightbrown silty CLAY with frequent fragments of DF (1-5mm), abundant iron staining, mottled grey/brown to red-brown [<20kPa]
160-185	Soft to very soft, grey and brown mottled, slightly silty CLAY, gleyey [<20kPa]
185-215	Soft light brown, occasionally dark brown, organic (?) silty CLAY with heavy iron staining (former topsoil?) [~50kPa]
215-	WMF [>200kPa]

Borehole plot 3

Depth from surface (cm)	Description
0-15	Soft, dark brown, organic silty CLAY (topsoil);
15-120	Soft, orange-brown slightly silty CLAY, wet at 60 to 70 with water possibly entering through fissures, from 90 increasingly grey/brown mottled [pocket penetrometer undrained shear strength indication <20kPa]
120-130	grey fine uniform SAND (~210micron)
130-150	Soft, orange-brown slightly silty CLAY [<20kPa]
150-160	Soft to very soft, grey and brown mottled, slightly silty CLAY, gleyey (old topsoil?) [<50kPa]
160-	WMF [~100-150kPa]

Borehole plot 4

Depth from surface (cm)	Description
0-15	Soft, dark brown, organic silty CLAY (topsoil);
15-100	Soft to very soft, light brown slightly silty CLAY, wet at 60 to 80 with water possibly entering through fissures [pocket penetrometer undrained shear strength indication <20kPa]
100-105	Very thin band of very soft, light yellow-grey-brown silty CLAY (possible slip surface material)
105-130	Soft, mottled, grey-brown slightly silty CLAY
130-170	Brown-grey, slightly clayey SAND (~210 micron) with iron staining; gleyey
170-180	Soft to firm, brown-grey silty CLAY
180-240	Brown-grey, slightly clayey SAND (~210 micron) with iron staining; gleyey, becoming increasing clayey with depth
240 -	Soft to firm, brown-grey sandy CLAY

Borehole plot 5

Depth from surface (cm)	Description
0 – 20	Topsoil
20 – 80	Brown, firm silty CLAY with occasional iron staining and accretions
80 – 120	Light grey, orange brown smooth firm slightly silty CLAY
120 – 170	Brown firm silty CLAY with stone fragments (weathered, rounded, flat 60mm max diameter)
170 – 285	Light grey and brown mottled (banded?) becoming progressively more firm to stiff with depth CLAY with occasional orange brown to dark brown iron staining and manganese accretions
285 – 295	Brown, uniform fine SAND
295 - 320	Brown, very slightly clayey, fine SAND (wet)
320 – 345	Light brown, grey, stiff CLAY with iron/manganese accretions (20-30mm)
345 – 400 e.o.b.	Light brown and light grey, mottled and

	gleyey, stiff to friable slightly clayey SILT to very fine SAND (dry-ish)
Remarks Wet zone/seeps of free water between 140 and 170. Interpretation: top 120 slide material over Dogger-based slope wash with plastic deformation of clays that become stiff due to base draining over sand. Sand overlying silts of Staithes formation	

Borehole plot 5.2

Depth from surface (cm)	Description
0 – 30	Topsoil
30 – 100	Light brown, firm to stiff, silty CLAY
100 – 160	Light brown, light grey stiff slightly silty CLAY, gleyey, mottled with occasional dark grey, purple staining (manganese?) at 120-130
160 – 200	Light brown, occasionally light grey silty CLAY with occasional orange brown stone fragments (10 – 20mm) rounded and weathered
200 – 240	Light grey, occasionally light brown silty CLAY with frequent orange brown stone fragments (10 – 20mm) rounded and weathered
240 – 245	Thin band of orange brown fine SAND (dry)
245 - 255	Light grey, occasionally light brown silty CLAY with frequent orange brown stone fragments (10 – 20mm) rounded and weathered
255 – 265	Brown fine SAND (wet) with illuviated clay (when tapped, free water appears at surface)
265 – 285	Light brown very stiff silty CLAY to clayey SILT with some friable, more silty structures affected by iron staining, occasional accretions of iron and small iron stones fragments (possible SSF formation)

Appendix III

Measured Electrical conductivities (EC) at each plot.